UCLouvain

FACULTE DES SCIENCES

Faculté des sciences

Chemiresistive gas sensors for methane, based on lead sulphide nanoparticles and reduced graphene oxide

Author : Nathalie HERMANS

Supervisors : Prof. Sophie HERMANS, Prof. Benoît HACKENS

Readers : Prof. A. VLAD, Dr. Y. DANLEE, Prof. A. DELCORTE

Academic Year 2022-2023

Master [120] en sciences chimiques à finalité approfondie

Acknowledgements

First and foremost, I extend my sincere thanks to Professor Sophie Hermans for her unwavering support, enthusiasm, and kindness. I learned so much from her knowledge which really helped to dive deeper in my project and to progress. I am deeply grateful to Professor Benoît Hackens for providing me with invaluable advice and teaching me numerous things. His expertise and mentorship have been truly transformative, and I am incredibly grateful for the chance to explore a field of study that was previously unknown to me. It has opened a world of possibilities and expanded my horizons in exciting ways.

I would also like to extend my appreciation to Professor Fernando Massa Fernandes for giving me the opportunity to work on his multidisciplinary project. Furthermore, I would like to extend a special thank you to Oriane for her invaluable assistance in the electrical engineering aspect of my project. Her contributions and insights have significantly enhanced the quality of my work, and I am truly grateful for her support. I also want to thank Professor Fouad Haj Hassan for his keen interest in my project and his valuable contributions and kindness. His expertise and guidance have been instrumental in shaping my research.

I am grateful to Professor Pierre Eloy for his valuable help with the XPS analysis and his kindness. Furthermore, I would like to thank Dr. Koen Robeyns for his previous help and his devotion in helping me overcome the obstacles I encountered. I also want to thank Miloud Zitout from Winfab platform for his valuable work and his kind support. Also, I would like to thank Sabine Bebelman from the BSMA division for her spontaneous help with the FTIR and Raman equipments.

Furthermore, I would like to extend my thanks to the entire MOST laboratory group. Their helpfulness and kindness have created a collaborative and nurturing environment where I felt myself comfortable. Jean-François, I am grateful for your responsiveness and willingness to assist whenever needed. Louise and Antonin, your support and positive energy have been uplifting and greatly appreciated.

Also, I would like to express my gratitude to Professors Alexandru VLAD, Arnaud DELCORTE and Dr. Yann DANLEE for agreeing to be the readers of my project. I am pleased and thankful for their time, expertise, and valuable feedback.

Lastly, I would like to express my deepest gratitude to my friends for their support throughout this challenging five-year journey, with a special acknowledgment to Raphaël. Our mutual support during

difficult moments has been precious and has played a significant role in overcoming obstacles during these five years.

Abstract

Nowadays, global warming is a pressing issue that is being intensified by greenhouse gases. Among these gases, methane is the second most abundant anthropogenic gas released after carbon dioxide. Methane is widely used as a fuel in chemical industry due to its favourable ignition properties and high heating value, making it also a suitable choice for residential and commercial heating systems. However, methane poses challenges for detection as it is a low polarizable gas. Additionally, it can react with or absorb ambient moisture and is susceptible to interferences with other gases like VOCs, NO_2, and CO. Therefore, there is a growing demand for methane gas sensors that are sensitive, selective, and user-friendly. One potential solution lies in the use of solid-state chemi-resistors made of nanohybrid materials, specifically the promising combination of lead sulphide nanoparticles (NPs) and reduced graphene oxide (rGO). This work focuses on exploring this combination.

The objective of this Master's thesis is to develop a sensor that is sensitive, selective, environmentally friendly, and simple to produce. To achieve this goal, the device is constructed using lead sulphide nanoparticles coated onto reduced graphene flakes, which are then deposited onto interdigitated electrodes. When the PbS NPs encounter methane gas molecules, NPs resistance increases, leading to a charge transfer from the NPs to the graphene flakes that are in contact with the interdigitated electrodes. This process generates an easily interpretable electrical signal, providing a readable output.

The objective of this study was double. Firstly, it aimed at controlling the size and purity of the NPs through the utilization of two different protocols. This was done to achieve well-dispersed nanocrystals on reduced graphene oxide flakes. Secondly, commercial graphene oxide was subjected to solvo-thermal reduction at various temperatures using either water or NMP as the solvent, and ascorbic acid was employed as the reducing agent, to achieve the highest possible reduction rate of rGO. Both materials were manually deposited onto interdigitated electrodes (IDEs), resulting in PbS NPs exhibiting higher resistance compared to rGO. Furthermore, rGO/PbS devices generally displayed higher resistance than pure rGO devices. The study also explored the charge transport mechanisms within the materials by investigating their decreasing resistance with temperature, revealing the occurrence of two distinct regimes. Finally, four devices were tested under a calibration methane gas, containing 2.5% volumetric methane and unfortunately none of the devices showed any sensitivity to methane. The deposition technique as well as the synthesis routes must be further improved to understand the observed ineffectiveness.

List of Abbreviations

CB: Conduction band

DFT : Density-functional Theory

DI water : Deionized water

DOS : Density of states

E_a : Activation Energy

FTIR : Fourier-transform infrared

GO : Graphene Oxide

IDEs : Interdigitated electrodes

IV: Current as a function of voltage

MQ water: Milli-Q water

NC(s) : Nanocrystal(s)

NMP : 1-methyl 2-pyrrolidone

NP(s): Nanoparticle(s)

PCB : Printed circuit board

QD(s) : Quantum dots

rGO : Reduced graphene oxide

RT : Room Temperature

SEM : Scanning electron microscopy

TEM : Transmission electron microscopy

TGA: Thermogravimetric analysis

VB: Valence band

VOCs : Volatile organic compounds

XPS : X-Ray photoelectron spectroscopy

XRD : X-Ray Diffraction

XRF : X-Ray Fluorescence

Table of contents

I. STATE OF ART

1.1 Methane gas industry

Methane is a simple gas composed of one carbon atom bonded covalently with four atoms of hydrogens. It is a greenhouse gas used extensively by the chemical industry. Methane is mainly used as a fuel because it has interesting ignition properties and high heating values that make him a good candidate for heating, such as in residential or commercial heating systems. Combined heat and power engines convert the generated heat to electrical power. The electrical energy is then either recirculated back into the facility or exported to the national grid. Except for those who are overweight, have irritable bowel syndrome, inflammatory bowel illnesses, or anorexia, the exhaled air from typical human breath does not include methane. [1]

However, it is produced in large quantities by farming and in particular cows, still a large part of our alimentation, and sometimes kept inside for most parts of the year. It exhibits explosive properties when its concentration rises to 4.6% in the air. Indeed, it is a main component in dangerous gas in coalmines. Currently, methane explosions continue to occur worldwide during the coal mining process. [2] Unfortunately, it remains a challenge to detect methane gas because it is colourless, odourless. Moreover, methane can cause dizziness, headache, nausea, or even severe suffocation when inhaled. [3]

After carbon monoxide, methane is the second most anthropogenic greenhouse gas [4] and has several anthropogenic causes, the most significant one stems from fossil fuels (29%) as shown in Figure 1.

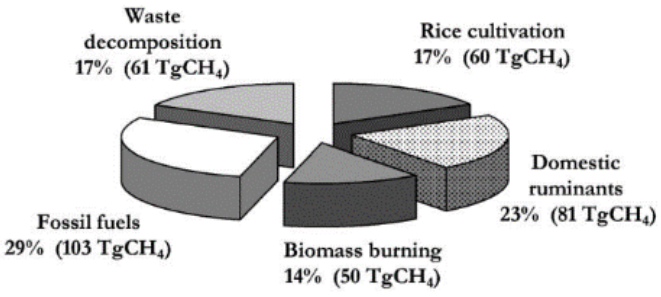

Figure 1. Contribution of individual sources to total anthropogenic methane emissions. [5]

Methane emissions in Belgium fell by 39 % from 1990 levels, mostly because of less routine trash disposal. This is mostly because less rubbish is being routinely landfilled. Modernization in agriculture, a significant source of methane emissions from livestock and fertilizer use, has also contributed to the observed decline. [6] Nevertheless, according to *The International Methane Emissions Observatory* (IMEO) of the United Nations Environment Programme

(UNEP), one estimates the total global methane emissions from industry at 80-140 million tons per year. In the same report, “Oil and Gas Methane Partnership 2.0” (OGMP 2.0) reports that the total emissions of 2022 amount are 1.3 million tons of methane. [7]

Upon release to the atmosphere, methane turns out to be a greenhouse gas thus an environmental concern. Its rising concentrations contribute to different atmospheric perturbations. First, tropospheric O_3 levels will be increased and that will indirectly lead to higher greenhouse effect and potentially to urban high ozone events. Moreover, tropospheric OH could be suppressed if methane concentrations are too high. Consequently, these tropospheric OH will not be able to oxidize and remove harmful hydrocarbons and hydrogenated chlorofluorocarbons (HCFCs) anymore. Methane is also harmful to the stratospheric ozone since it creates stratospheric water vapor, that oxidizes the ozone. [8] [9] Additionally, when methane reacts with chlorine, this explosive reaction participates to ozone destruction. [9]

Methane detection thus becomes more vital than ever for an array of applications, including health and environmental monitoring. Because of the growing worry over methane, many methane detection technologies have been designed and developed.

1.2 Methane gas sensors

Despite its explosive reaction with chlorine, methane is generally considered a chemically inert substance, which makes its detection challenging for sensing strategies that rely on its derivatization.[10] Moreover, in comparison to other commonly studied gas molecules like H_2, CO_2, and CO, CH_4 molecules have a lower level of interaction due to their low polarizability. For example, CO_2 has a permanent quadrupole moment of $4.30 * 10^{26}$ esu-cm^2, and CO has a permanent dipole moment of $0.112 * 10^{18}$ esu-cm^2. [11] These two gases are higher sorption gases since the strength of electric dipole and quadrupole moments affects the enthalpy of adsorption and Henry's constants. [12]

Since 2002, the industry has witnessed a growing number of patents related to methane gas sensors, indicating an increasing utilization of these sensors in various sectors. [13]

When discussing sensors, four parameters must be considered: the sensing materials, the sensing mechanisms, inherent properties, and the sensing platforms as shown in Figure 2. [12]

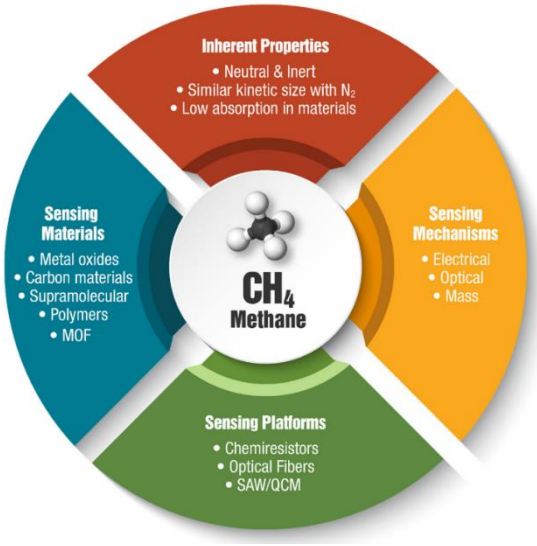

Figure 2. Summary of inherent properties of CH_4, and the demonstration of different sensing materials, mechanisms, and platforms. [12]

Sensing materials can be metal oxides, semi-conductor metals, carbon materials, supramolecular or MOFs. Regarding the sensing mechanisms, it can be electrical, optical or a mass mechanism. Sensing platforms can be chemiresistors, optical fibres or Surface acoustic wave (SAW). Common techniques are piezoelectric sensors, spectroscopic methods, using Raman or infrared, electrochemical detection or gas chromatography. [10] It is noteworthy that the most widely used methane gas sensing techniques are catalytic combustion sensors, non-dispersive infrared sensors, and conductive-type sensors.[2] Here is a brief explanation of these three mentioned main methods with their advantages and drawbacks.

Catalytic combustion sensors are called **pellistors** or calorimetric detection and are used to detect flammable gases. [10] A pellistor sensor is a semiconductor made of a platinum or palladium-based noble metal catalyst and a heating coil. In practice, the target gas is burned by the catalyst pellet and, the metal coil is used to detect any alterations in temperature generated by the combustion of gases. The created heat will change the semiconductor resistance that is proportionate to the gas concentration. These thermal conductivity sensors quantify the heat that is lost by the detecting element when the target gas is present. [4] To minimize heat loss through conduction along the metal wire and to have enough sensitivity, the wire has to be thin, and this consequently leads to a fragile device. To increase the selectivity towards the gas e.g. methane, one can combine two noble metals with differing catalytic activities towards methane oxidation, for instance, platinum and palladium. [14] Palladium can oxidize methane and other hydrocarbons at approximately 400 °C, whereas platinum can only oxidize longer hydrocarbon chains, under the same conditions and will need temperatures as high as 700 °C to oxidize methane. [15] Consequently, the measurement of methane concentration can be achieved by a reference sensor and by simply examining the differences observed at each electrode. Another way to increase the selectivity of the sensor is to use a single pellistor (only one metal as a catalyst) and to combine it with gas chromatography. Overall, the sensors for catalytic

combustion respond well enough to methane but, they must perform at a high temperature, which results in high power consumption and there is high possibility of interferences. [4], [10]

The second most used technique is an optical sensor called **non-dispersive infrared sensor**, meaning no dispersive element such as a prism or diffraction grating is being used like in conventional spectrometers. Optical sensors are advantageous because they can operate in flammable gaseous environments without the need for electrical wires and contacts and therefore provide remote sensing capability, immunity to electromagnetic interference, and non-invasive measurement compared to other sensing platforms. Spectroscopy examines the interaction between the absorbed or emitted light and molecular and/or elemental structures. Spectroscopic methods can detect many gases, including methane in a quantitative manner. [16][4] In general, spectroscopy can be quantitative and qualitative and is largely used in many fields such as biomedicine [17], pharmaceuticals [18], and food [19] analyses, among others. Infrared absorption sensors enable the precise detection of small quantities of molecules and the recognition of molecular structures and conformational states. Methane can absorb in the infrared range [12] and its absorption lines are usually a unique feature under detection. Near infrared (IR) lasers have an advantage over mid IR lasers as they do not necessitate costly cooling equipment and are simpler to operate. However, most of the molecules of interest have only overtones and combinational bands in this range, which have lower absorption strengths compared to the mid IR range, which offer greater sensitivity.[10] In conclusion, nondispersive infrared sensors have good response toward methane, but they are expensive and complex and require great power supply. Moreover, spectroscopic instruments are designed for laboratory use only and are therefore non portable. This increases operating expenses and limits their applicability for point-of-care analysis, which is performing the analysis near the patient or near the area of interest.

The third most used method is **conductive sensors** in solid state. Conductive sensors, also called chemi-resistive sensors, offer several benefits compared to the two other types of sensors mentioned above. Indeed, their advantages include compact size, affordability, ease of integration, and reliability. [4] These sensors remain the most advantageous as long as one ensures that they also have low power consumption. [2] A sensor detects the analyte by a process of transduction which leads to an interpretable signal generation. There exist many types of transductions such as field-effect transistor (FET), solid-state electrochemical sensor (SSES), quartz-crystal microbalance (QCM), gas capacitor, surface acoustic wave (SAW) and chemi-resistors. This latter is the most advantageous and ensures an easy commercialization

since it is easy to fabricate, allows a large combination of sensitive materials – leading to hybrid materials - uses a very small quantity of active materials (a few milligrams only are required) and provide simple sensing data. [20] These types of sensors will be described in more details in the section below.

1.3 Chemi-resistive gas sensors and functional nanomaterials

A perfect gas sensor must provide high responsivity, good selectivity, fast response/recovery, great stability/repeatability, room-working temperature, low cost, and easy-to-fabricate for practical applications. Response time is defined as "the time taken by the sensor to get the response from 10% to 90% of its final value". Similarly, the recovery time is defined as "the time that a sensor output takes to get from 90% to 10% of its initial value when it is exposed to air". [21]

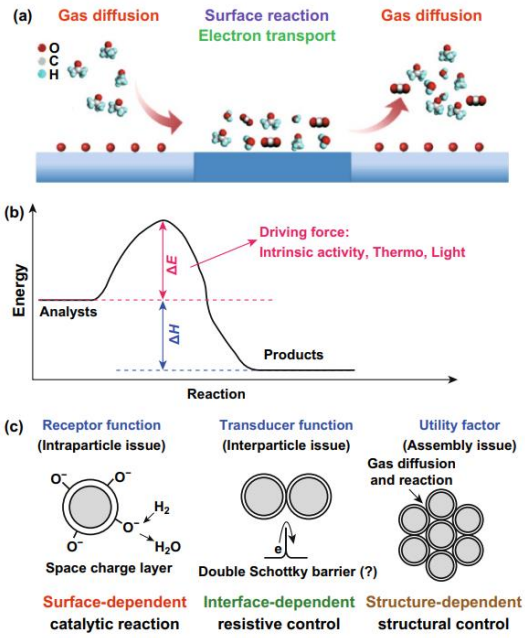

Figure 3. . a) Main processes of gas sensing mechanism b) potential energy diagram c) basic mechanism of nanomaterials-based conductive sensors. [20]

Chemiresistor sensors are conductive-type sensors which are often built on a silicon, ceramic or glass substrate on which there are metallic electrodes such as gold. The gas-sensitive materials are deposited and placed between those electrodes and the sensor's efficiency is really dependant on the placement of the gas-sensitive materials. Chemi-resistive gas sensors are solid-state sensors which "convert the response of the sensing material upon interaction with gas molecules into interpretable electrical signals i.e., electrical conductivity or resistance". [3] Chemi-resistive sensors are comprised of two main components - the sensing material or receptor, and the transducer (see Figure 3-c).

Nanostructured gas-sensitive materials are advantageous for gas sensing due to their larger surface-to-volume ratio – caused by an increased number of surface atoms and own dangling bonds compared with the atoms in bulk – their small size effect and their quantum effect. These characteristics impact the adsorption strength with gases. [2]

There are three main steps within the **sensing mechanism**. First, diffusion/molecule capture step , then a surface reaction step (including charge transfer), and eventually, a charge carrier transport step followed by gas desorption, as shown in Figure 3-a. The sensing mechanisms depend on whether the material is p- or n-type, thus if the majority of carriers are holes or electrons, respectively. Until now, most of these sensors and sensor arrays have used sensing

elements based on a single material or transduction mechanism. Either they rely on the intrinsic sensing activity of the material either they employ external stimuli like temperature or light, to stimulate the sensing effects of target gases (Figure 3b). In p-type metal oxide sensors (MOSs), like in n-type MOSs, an increase in temperature causes a decrease in the sensor resistance. However, when exposed to an oxygen environment, p-type MOS generates holes due to the adsorption of oxygen ions on the surface via the excited electrons from the valence band. This process results in an increase in the number of charge carriers, causing a reduction in sensor resistance (in contrast to n-type MOS). When the p-type MOS sensor is exposed to a reducing gas environment, the electrons inject into the valence band and recombine with the holes, leading to a decrease in the number of holes. As a result, the sensor resistance increases (opposite to n-type MOS). This general sensing mechanism is illustrated in Figure 4. [22] The increasing resistance is also linked to the double Shottky barriers (illustrated in Figure 3-c) which are a type of electrostatic potential barriers that are formed at the grain boundaries in various polycrystalline compound semiconductors [23] such as ZnO, $BaTiO_3$, and $SrTiO_3$. [24], [25] These barriers are caused by acceptor-like grain boundary states that could trap electrons from crystal bulks nearby. [26] One of the factors that might generate these acceptor-states are excess of oxygen coming from chemisorbed oxygen or excess amount of oxygen. [27], [28]

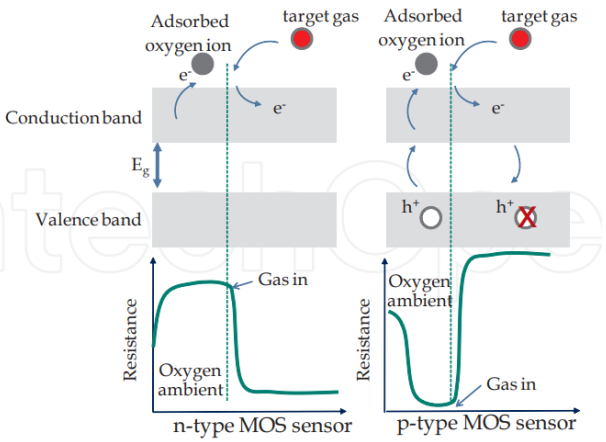

Figure 4. Schematic diagram for modification of the sensor resistance upon exposure to the target gas (reducing gas) in the cases of n-type and p-type MOS sensors.[22]

1.4 Graphene, graphene oxide and reduced graphene oxide

Graphene is a one-atom-thick sheet of carbon atoms that are arranged in a hexagonal lattice. It is a two-dimensional (2D) single layer of cycles of sp^2 hybridized carbon atoms arranged in a honeycomb structure as shown in Figure 5. It has several unique properties, including high electrical conductivity, high strength, and high thermal conductivity, and can be relatively easily oxidized in graphene oxide, which make it an attractive material for a wide range of applications.

1.4.1 Pristine graphene

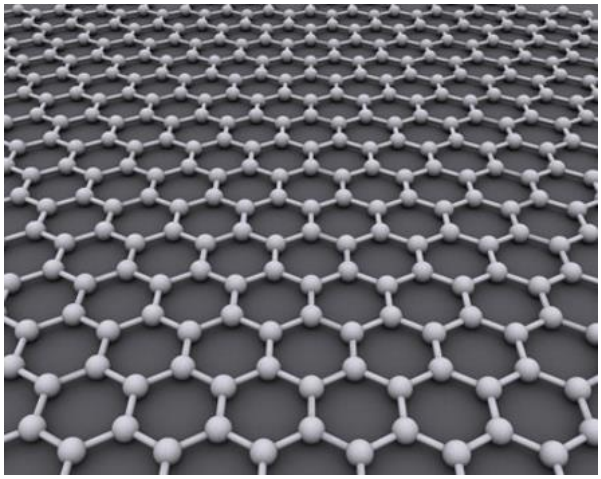

Figure 5. Pristine graphene [128]

The two-dimensional highly crystalline lattice – leading to a high electronic mobility – the low intrinsic noise and the large specific surface area provide a remarkable sensitivity and an extraordinary response towards gases to pristine graphene in sensors. [3][29] The fact that high-quality graphene has a remarkably low defect density, which often acts as a hindrance to charge transport, suggests that graphene has the potential to be the material of choice for future electronic devices. Indeed, due to its planar two-dimensional structure, graphene is highly suitable for integration into devices. [30] Additionally, graphene has been demonstrated to be a versatile material for research in a broad spectrum of applications such as sensors [31], supercapacitors [32], catalysis [33], and thin-film transistors [34].

After its 2D-crystal lattice, **ambipolarity** is the second crucial aspect related to charge transport within graphene. Its unique band structure allows a continuous tuning of the carrier type between holes and electrons by supplying the appropriate gate bias when operating in the field-effect configuration. [35] The band structure is characterized by conduction and valence bands that have nearly linear dispersion. These bands intersect at the corners of the Brillouin zone, resulting in a semiconductor with a zero-band gap. [36] When negative gate bias is applied, the Fermi level falls below the Dirac point, leading to a significant population of holes in the valence band and this is making graphene p doped. Conversely, when positive gate bias is applied, the Fermi level rises above the Dirac point, resulting in a significant population of electrons in the conduction band and making graphene n doped (see Figure 6). In other words, ambipolarity implies that the adsorption of groups that either withdraw or donate electrons to graphene can result in "chemical gating" of the material. This is easily detected in

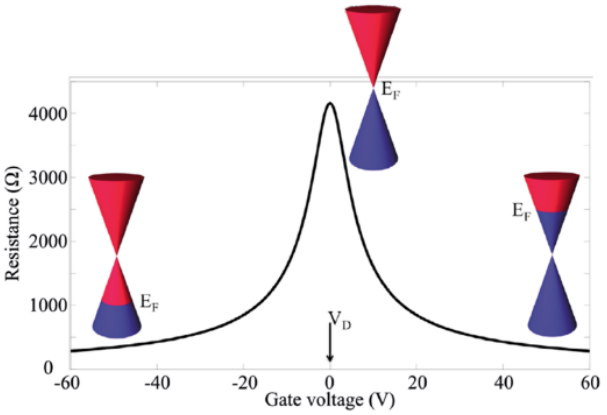

Figure 6. The usual Resistance vs Gate voltage dependence for graphene, showing the Dirac point (VD), where resistance reaches a maximum. In this case the Dirac point is at VD = 0 (neutrality point). [129]

a sensor setup that utilizes resistive-type measurements. This chemical gating, characteristic of the ambipolar semiconductor, means that doping levels can be dynamically controlled solely through gating and this property makes them fundamentally different from silicon-based logic. Indeed, in the case of ambipolar semiconductors, junctions or even more complex logic can be formed by temporarily providing local gate biases to different regions of the same flake. Overall, reconfiguring the biases can entirely redefine the device without physically altering the channel material.

Different **synthetic routes**, bottom-up or top-down, produce graphene materials with distinct characteristics and for graphene-based sensors, both the sensing material and the synthesis approach are important. The first synthetic route, discovered in 2004 by Novoselov et al. in Manchester [37] consists in a mechanical exfoliation, ultimately a much simpler approach than the ones utilized before that date. The first-ever isolation of single layer graphene was achieved through the "peeling" method. This process involves using a polymer sticky tape to gradually eliminate layers from a high-purity graphite flake. Eventually, the tape is pressed onto a substrate to collect a sample. At this stage, flakes captured on the tape are usually thicker than a single layer but the van der Waals forces that exist between the substrate and the tape can detach a lone sheet when the tape is removed. With practice, the technique yields high-quality crystallites that can be over 100 μm^2 in size [38] but demands a lot of patience, making it extremely challenging to locate a single layer and consequently limits its potential as an industrially scalable process. However, scalability is not the only important factor to consider when evaluating the effectiveness of any synthetic route to graphene. Other crucial considerations include producing a high-quality 2D crystal lattice to ensure excellent mobility, achieving precise control over crystallite thickness to ensure consistent device performance, and ensuring compatibility with current CMOS (complementary metal-oxide semiconductor) processing for easy integration.

Two other techniques, epitaxial growth, and chemical vapor deposition which are the most promising bottom-up techniques [36], rely on carefully chosen platforms to enable the growth of good quality graphene. The epitaxial technique pioneered by De Heer et al. involves the high-temperature reduction of silicon carbide to produce graphene.[39] The second substrate-based method is chemical vapor deposition (CVD) of graphene on transition metal films causing multilayers [40] as well as single layers [41], depending on the chosen metal film. This process involves exposing a transition metal to a hydrocarbon gas at high temperatures, causing carbon saturation on the metal surface. Typically, methane gas is used with nickel films.

Upon substrate cooling, the solubility of carbon in the transition metal decreases, causing a thin film of carbon to precipitate from the surface. Both CVD and epitaxial growth are expected to produce a single layer of graphene over an entire wafer which helps greatly the integration the new material into current semiconductor devices. However, it is quite hard in practice to control the layer formation without creating multiple layers and therefore it is difficult to have a controlled thickness.[38]

Despite its multiple exceptional properties, pristine graphene, in its undoped state, does not have dangling bonds, which prevents it from distinguishing between the number of possible gas species adsorbed on its surface.[38] The absence of a specific bandgap in graphene is also problematic if one desires to adjust its sensitivity within sensors.[42] Consequently, modifying graphene properties is necessary to transform it into a selective and effective sensing material for gas detection.

1.4.2 Graphene oxide and reduced graphene oxide

The abundance of diverse oxygen functional groups in chemically derived graphene, specifically graphene oxide (GO) and reduced graphene oxide (rGO), offers significant advantages for the high-sensitivity and selective enhancement of gas sensing responses. Moreover, it is an economical and high-yielding approach with a non-zero bandgap. [3]

Graphene oxide is a modified form of graphene that has undergone alteration by the incorporation of oxygen-containing functional groups like epoxy, hydroxyl, and carbonyl groups. The introduction of these functional groups into the graphene structure is achieved through a chemical oxidation process called graphite oxide synthesis, which involves the oxidation of graphite. These functional groups make GO hydrophilic since they facilitate the bonding of water molecules with GO layers through hydrogen bonding, making them capable of water adsorption and/or intercalation through the layers. [43] The principal method to produce graphite oxide was established by Hummers et al. in 1958 and it is therefore now called the Hummers method. [44] This top-down process is safe and quickly achieved since it can be completed in less than two hours at temperatures below 45°C. The method consists of a process that involves a water-free mixture of concentrated sulfuric acid, sodium nitrate, and potassium permanganate. Then, the resulted graphite oxide is exfoliated via stirring followed by magnetic stirring and heating at 70°C for one of multiple days to eventually produce graphene oxide. [45]

The presence of these functional groups in GO makes it highly reactive, and it can be easily dispersed in water or other solvents. Due to these functional groups acting as defects on

top of the graphene layer, GO is predicted to show even larger enhancement in adsorption energies and charge transfer from gas molecules to the GO surface than pristine graphene. Moreover, GO has a higher interlayer spacing than non-oxidized graphite, because the bonded carbons with oxygens are sp^3 hybridized. This hybridization leads to a non-zero bandgap which allows tuneable electrical properties by varying the oxidation rate and finally impacting the gas adsorption and thus sensitivity when integrated in sensors. [3]

Unfortunately, GO is afflicted by excessive sensor recovery time after detection due to its strong adsorption energy that might restrict its sensing capability, which is why it is usually first transformed into rGO. This modification enhances the performance of the devices, improving both the response and recovery. Additionally, rGO showcases characteristics more similar to traditional semiconductors [46], which is intriguing for its electrical properties while GO lacks sufficient electrical conductivity to be used as a conductance-based sensor.

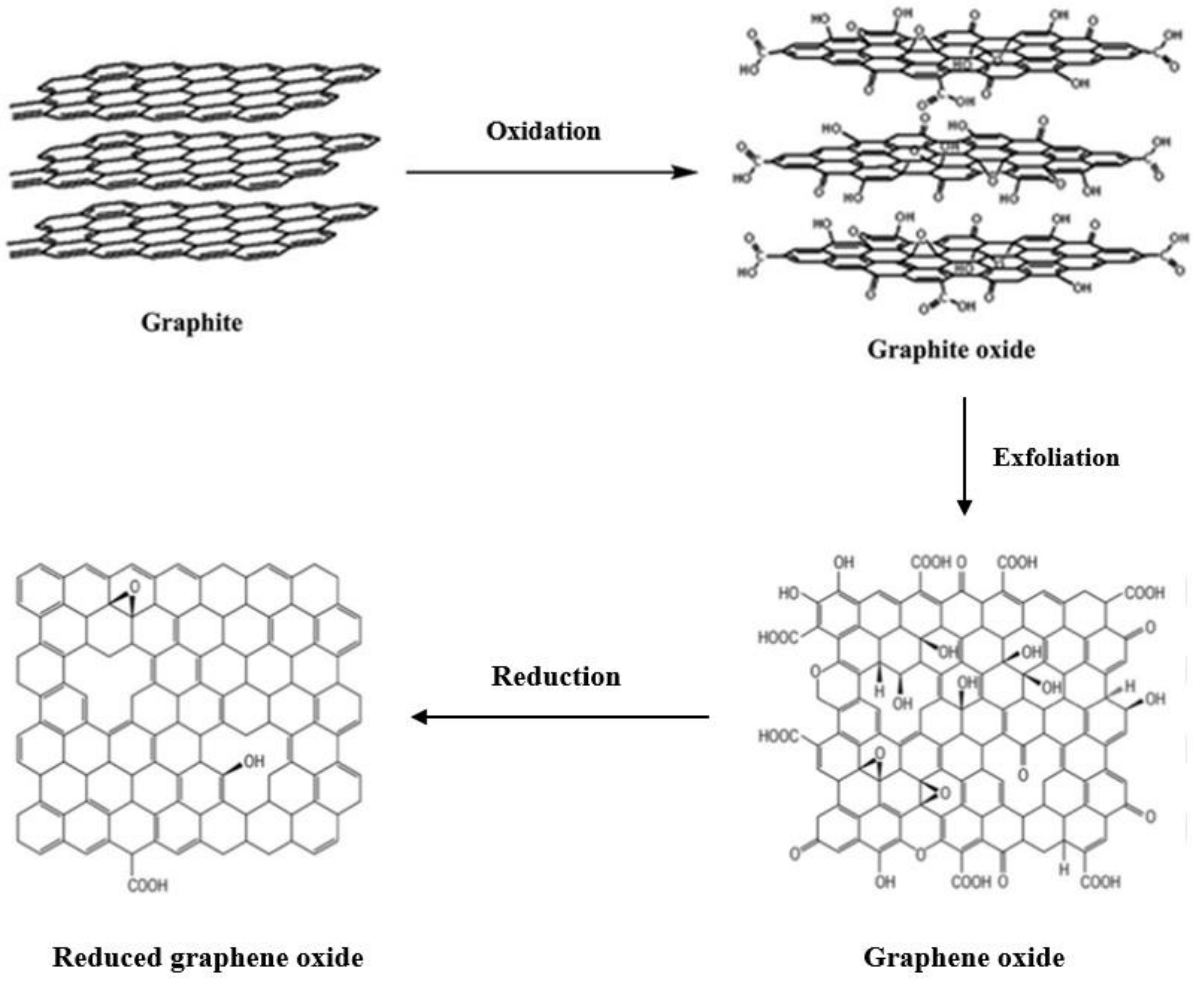

Figure 7. Schematic representation of the steps required for the production of rGO

rGO, or reduced graphene oxide, is a graphene form that has been chemically altered to contain less oxygen than graphene oxide. rGO has excellent electrical conductivity and features extremely reactive defect sites derived from the residual functional groups. [3] rGO as an active material for sensing application was first demonstrated by Robinson et al. in 2008. [47] It is noteworthy that if all the oxygen-based functional groups disappear during the reduction process, the capacity of gas adsorption will decrease. Therefore, a balance between the adsorption capacity provided by the defects and the electronic conductivity of rGO during the GO-reduction process is essential. [48] Synthetic route required to produce rGO from graphite is illustrated in Figure 7.

Reducing GO can be achieved by solvothermal annealing in organic solvents such as N,N-dimethylformamide (DMF) and N-methyl-2- pyrrolidone (NMP) which as boiling point of 204°C. These reductions result in stable rGO dispersions. [49] Many reductants can reduce GO in rGO efficiently but the most used are the reducing agents like hydrazine hydrate [50] and sodium borohydrate [50], which are harmful to the environment and to the health. [51][52] Fortunately, many environmentally friendly alternatives as reducing agents have been discovered. [51] Ascorbic acid, also known as Vitamin C, has been found to be a highly promising eco-friendly reducing agent as reported by Fernandez-Merino et al. in 2008.[53] Indeed, vitamin C is a powerful antioxidant able to donate electrons and protons leading to dehydroascorbic acid (see equilibrium in Figure 8). [54]

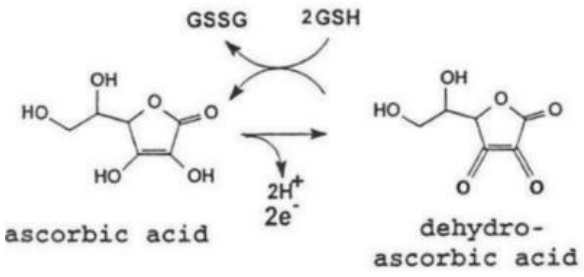

Figure 8. The equilibrium and the species in the ascorbic acid – dehydroascorbic redox system. The oxidized form dehydroascorbic acid can be reduced by glutathione (GSH) [54]

1.5 Semiconductor nanocrystals - synthesis, mechanisms, and properties

Semiconductor are characterized by their band structures and a bandgap (indirect or direct) energy (E_g) between 0 and 4 eV, which is the energy required to excite an electron from the valence band (VB) to the conduction band (CB) (see Figure 9 a-b) for bulk and nanocrystals. When it comes to molecule size, E_g is the energy required to excite an electron from the highest occupied molecular orbital (HOMO) to the lowest unoccupied molecular orbital (LUMO), as shown in Figure 9-c. Nanoparticles have one dimension in the range of 1 to 100 nm in size by definition. Quantum confinement effect and modification of the band structure can occur if one dimension of a semiconductor particle is smaller than the Bohr exciton radius (between 1 and 10 nm) of the material. The confinement causes a blue shift to higher energy of the absorption band corresponding to the bandgap and an increasing half-width at half-maximum (HWHM) of the peak (see Figure 10) due to the nonlinear relationship between band gap and nanocrystal size (Figure 11). When the dispersity is constant, the HWHM of QDs is proportional to their diameter meaning that if quantum dots size decrease, HWHM will do the same because the band gap is more sensitive to changes in QD size for smaller QDs compared to larger QDs. As a result, the HWHM cannot directly measure the dispersity, because it is influenced by the size of the QDs. Additionally, the physical dimensions, composition, structure, shapes, and surface chemistry of semiconductor nanocrystals significantly influence their properties and enable them to be used as active materials in various applications. The fine-tuning of the band structures allows to obtain various electrical and optical properties of the material. Hence it is important to control the synthesis conditions and choose the appropriate precursor to obtain nanoparticles with the desired size and size distribution. The

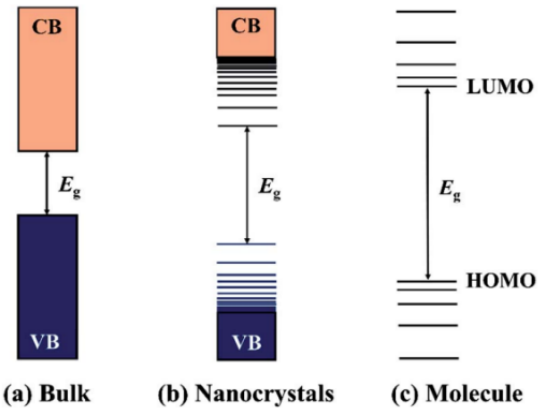

Figure 9. Comparison of electronic energy states of different types of semiconductor materials: (a) bulk inorganic semiconductors, (b) inorganic semiconductor nanocrystals, and (c) molecular semiconductors.[115]

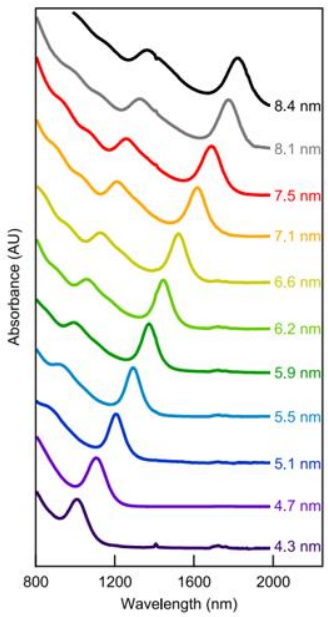

Figure 10. Absorption spectra using a 24:1 Pb:S precursor ratio showing synthetic range of 1000-1800 nm (1.25-0.70 eV). The bottom two spectra (dark violet, purple) were synthesized at 40 and 80 °C, respectively, while all others were synthesized at 120 °C. Labels indicate QDs diamaters.[60]

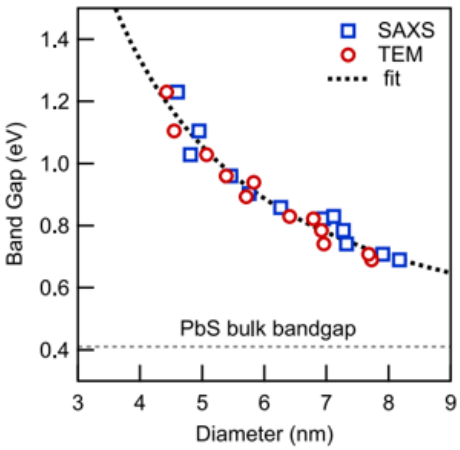

Figure 11. QD band gap versus diameter, as measured by TEM and SAXS. [60]

obtained nanocrystals sizes depend on several factors when carrying out these syntheses by wet-chemistry methods, such as the reaction temperature and time, the injection temperature of the reactant in the case of hot-injection methods, the reactivity and the concentration of precursors, the effect of solvent, surfactant, and pH, etc.[55]

To obtain such high-quality nanocrystals (NCs) with controllable physical or chemical properties, both top-down (e.g. ball milling [56]) and bottom up (e.g. chemical vapour deposition (CVD) [57] and metal–organic vapour chemical deposition (MOCVD) [58]) can be used. Top-down techniques reduce the size of the structure toward the nanoscale and are simple to use. [55][56] However, they are ineffective for manufacturing irregularly shaped and extremely small particles and therefore, it remains hard to obtain proper particle size and shape using this approach. While bottom-up is the formation of large nanostructure from smaller atoms and molecule and this approach allows for the formation well-defined shape, size, and chemical composition of nanoparticles. [59]

Moreover, the physical state of the reacting media of the bottom-up approach impacts strongly the obtained NCs. Synthesis can involve a vapour-phase approach, a solid-phase approach, liquid-phase approach, and a two-phase approach. [55] Unfortunately, vapor and solid phase approaches are the least convenient options for the fine control of the nanocrystals since they suffer from instrument and precursor limitations. On the other hand, the liquid-phase approach has been demonstrated to be an effective method for achieving well-defined semiconductor NCs which, in this case, are also called colloidal semiconductor nanocrystals (CS-NCs) and are often dispersed in suitable solvents with the aid of capping ligands or surfactants. The resulting stable dispersions allow direct applications such as spin-coating, roll-to-roll casting, and inkjet printing. These techniques are quite interesting because they are low-cost and offer high throughput and therefore, they can lead to large-scale device manufacturing. [55]

The liquid-phase approaches can be divided into three categories: firstly, the aqueous-based approaches such as the hydrothermal methods that are the most environment-friendly but do not provide an efficient morphology control of nanocrystals due to the low reaction

temperatures. [60] Secondly, organic-based approaches are non-aqueous methods employing high boiling temperature organic solvents, thus enabling the fine-controlled synthesis of CS-NCs. Non-aqueous approaches comprise the hot-injection method, [61] non-injection method [62] and the solvothermal method using autoclaves. [63] Thirdly, the two-phase approach is an aqueous– organic approach, where reactants that are often dissolved in separate phases and solid nanocrystals are formed at the interface of aqueous and organic media.

When it comes to the **reaction mechanisms** leading to the NCs, the formation process of NCs basically consists of two stages, based on the particle's formation model of Lamer [64] and shown in Figure 12. Reaction precursors are dispersed or dissolved in appropriate solvents, and chemical reaction between each other will provide the monomers. As their concentrations increase to the super-saturation level, nuclei are formed through the aggregation and self-nucleation of monomers. Then the growth process occurs as monomers continuously aggregate on these pre-existing nuclei until the concentration of monomers drops below the critical level. It is important to note that new nuclei are also formed during the growth of nanocrystals, which often leads to a broadening of the size distribution of the nanocrystals. Narrowing the size distribution is important when controlling the size of CS-NCs, this can be done by controlling nucleation and growth. This size-control can also be assisted by utilizing organic ligands. [65] The role of these capping agents will be further discussed in Section 1.6.2.

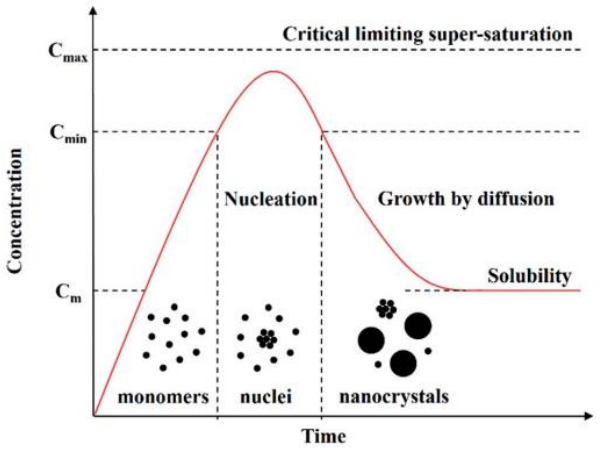

Figure 12. Schematic illustration of the nucleation and growth of nanocrystals in solution: precursors are initially dissolved in solvents to form monomers, followed by the generation of nuclei and the growth of nanocrystals via the aggregation of nuclei [60]

The growth stage of NCs can follow two types of processes: "diffusion-controlled growth" and "reaction-controlled growth". [55] The growth mechanism that is controlled by diffusion exhibits rapid reaction rates and the diffusion rate of monomers is the limiting factor. In this process, larger particles tend to grow at a faster rate, and smaller particles at a slower rate. In the case of reaction-controlled growth, the kinetic limiting factor is the reaction at the monomer surface. Unlike diffusion-controlled growth, the reaction rate is not dependent on the particle's size and moreover, as the growth progresses, the size distribution decreases, leading to a narrower distribution.

Two injection methods exist. The hot injection method can be utilized to separate the nucleation and growth processes and obtain a narrow size-distribution. This involves introducing the precursors at a high temperature in the reaction medium (where they react instantaneously) and this method has been successfully adopted to synthesize many semiconductor nanocrystals such as PbS [66] or PbSe. [67] However, the use of this method necessitates highly reactive reactants and air-free handling. Additionally, the injection step limits this method to a small scale. The non-injection/direct heating method, on the other hand, involves gradually increasing the temperature of the reactants. This method enables the use of lower temperatures and more environmentally friendly solvents. The precursors used in non-injection methods need to exhibit a low reactivity at low temperatures and a high reactivity at higher temperatures where nucleation of the precursors occurs rapidly, followed by the growth of nanocrystals, which is similar to the hot-injection method. Non-injection methods are significantly simpler to implement successfully than the hot-injection method. [55]

In the case of **diffusion-controlled reactions and the hot injection approach**, nucleation occurs immediately after injection, leading to a rapid increase in the average size of the particles, therefore resulting in a focused size distribution. At this stage, the monomer concentration is high, causing the particle size to be larger than the critical size, leading to size focusing. [55] However, as the monomer concentration decreases, particle growth slows down, causing the critical size to become larger than the average particle size. As a result, smaller particles shrink, and the size distribution becomes broader, a phenomenon known as "defocusing" of particle sizes or “Ostwald ripening”. [60], [68] The focusing and defocusing processes of size distribution are illustrated in Figure 13.

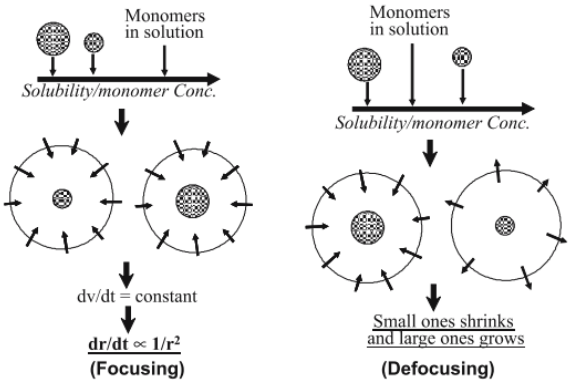

Figure 13. Schematic focusing and defocusing processes during the nanoparticle formation. [60]

1.6 Lead sulphide nanoparticles

Nanocrystals of PbS are air-stable and possess a near-infrared band gap that can be adjusted based on their size [69] which makes them an attractive material for applications such as photovoltaics[70], photodetectors[71], and infrared light emission. Due to their exceptional properties and multiple applications, they have been extensively studied. [72] Additionally, PbS can serve as a gas sensor with gases like NH_3, NO_2, SO_2, NO and H_2S. [73] However, there

have been limited investigations into the sensing capabilities of PbS regarding methane gas, with the first report on this topic being relatively recent, in 2016, by Mosahebfard et al. [74]

1.6.1 PbS nucleation and growth

Let us first look at mechanisms of nucleation and growth that might occur when synthetizing PbS nanocrystals. Weidman et al. reported that monodisperse phase of nanocrystal growth proceeds by diffusion-limited monomer addition from solution. [75] Moreover, it is known that the Pb:S ratio during nucleation is a critical parameter affecting subsequent growth and monodispersity of PbS nanocrystal ensembles.[72] Indeed, one can observe a delay in the "Ostwald ripening" or "defocusing" under the condition of constant limiting reagent (sulphur) suggesting that as the Pb:S ratio increases, the nucleation rate decreases, and thus a lower number of nanocrystal nuclei are formed during the initial burst of nucleation. [72] The contrary happens in the case of the nucleation of CdS and CdSe, for which a larger stoichiometric excess (and larger overall precursor concentration) increases the nucleation rate, forming consequently more nanocrystal nuclei and shortening the time during which nanocrystals grow via monomer addition. [75] The significant contrast demonstrates that the rate of precursor reaction is not the underlying mechanism by which the precursor stoichiometry influences the growth of nanocrystals in PbS system. There is a suspicion that a higher viscosity of the solution (caused by a higher amount of lead precursor) results in reduced mass transfer in the system, leading to an overall decrease in the number of nucleation events. As a result, with fewer nuclei formed during the nucleation burst, there is more sulphur monomer available to attach to existing nuclei, which prolongs the period during which nanocrystals grow through monomer addition. In summary, the primary function of the excess lead precursor is to regulate the equilibrium between precursors utilized during nucleation and those that remain available for further growth of nuclei.

1.6.2 PbS nanoparticles used in gas sensors

As mentioned earlier, PbS nanoparticles for gas sensing have been widely studied for several gases like NH_3 or NO_2. However, using PbS materials for methane gas sensing is quite recent. [74]

Simple **preparation methods** are achievable and lead to good sensing results. These preparations include lead precursor (e.g., lead nitrate dissolved in deionized (DI) water), on which a capping agent, such as 2-mercaptoethanol (see Figure 14 for proposed interaction with the NPs), is slowly added. A sulphur precursor (e.g., sulphur sulphide dissolved in DI water) is eventually slowly added.

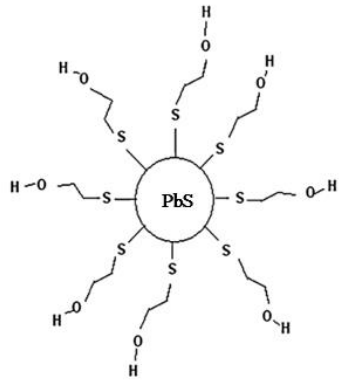

Figure 14. Proposed capping interactions with 2-mercaptoethanol. Inspired by [76]

Capping agents play an important role in the control of the nanoparticles size since they prevent agglomeration and settling down of nanoparticles caused by Ostwald ripening and Van Der Waals (VdW) interactions between particles. [76] During the precipitation reaction, it is possible to achieve size selective synthesis by either using electrostatic stabilization to prevent agglomeration or introducing steric hindrance via the capping agents. Electrostatic stabilization works by generating an electrical double layer that results from ions adsorbed on the particle's surface and their associated counter ions in the dispersing media. When the electric potential linked to the double layer is significant enough, it creates a columbic repulsion force that stops the particles from aggregating. [76] Steric hindrance, on the other hand, can be achieved by the adsorption, on the surface of the particles, of large molecules such as polymers or by organic capping ligands, such as pyridine, ethanedithiol (EDT), ethylenediamine (EDA), and mercapto-carboxylic acid (MPA) to reduce interparticle spacing compared to the spacing obtained with polymers [55] A perfect capping molecule should establish a strong bond with the surface of the nanoparticles, ensuring that it remains attached almost permanently without interfering with any of the internal processes occurring within the nanoparticles to avoid interfering with its intrinsic properties. Additionally, it should obviously prevent the coalescence of nanoparticles.

PbS QDs show p-type semiconductor behaviour in ambient air due to oxygen doping effect [77] that leads to oxygen adsorption. Therefore, Mosahebfard et al. suggested the adoption of the above-mentioned general mechanism (see Figure 4) for PbS and suggest the following particular mechanism in case of methane sensing. When PbS nanoparticles are exposed to methane, which is a reducing gas, it reacts with surface-absorbed oxygen molecules through the following reaction:

$$CH_4 + 2\,O_2^- \rightarrow CO_2 + 2\,H_2O + 2e^-$$

As a result of the reaction between oxygen anions and the semiconductor surface, the excess negative charges of the consumed oxygen anions are released and returned to the semiconductor's conduction band, increasing the number of negative charges that are the minority carriers. Consequently, the concentration of holes (majority carriers) decreases, causing a degradation in the semiconductor's conductivity. [74]

As described in Section 1.3, the chemi-resistive gas sensors consist of a **receptor, a transducer and an utility factor** (Figure 3-c). The **receptor's** function is an intraparticle concern that involves the adsorption and reaction of methane with surface-adsorbed oxygen ions, leading to a modification of the width of the space-charge layer, also called the electron-depleted region (Figure 15). [2] Oxygen ions can exist in the forms of O^{2-}, O^{-}, or O_2^{-}, depending on the temperature. [78]

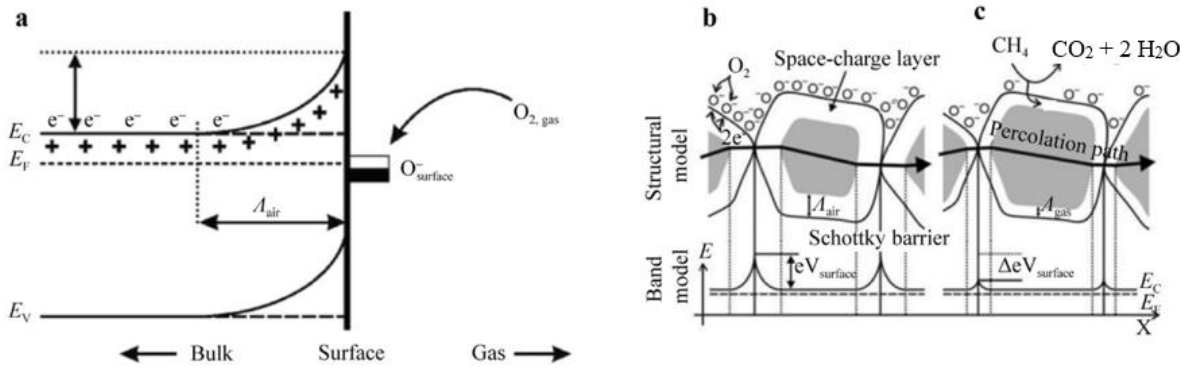

Figure 15. a) Schematic diagram of band bending after chemisorption of oxygen ions, where EC, EV and EF mean energy of conduction band, valence band and Fermi level , Λ_{air} means thickness of space-charge layer, $eV_{surface}$ means potential barrier, e^- denotes conducting electrons, and + represents donor sites; structural and band models of conductive mechanism upon exposure to reference gas, b) without or c) with CH_4.[2]

Mosahebfard et al. reported, from density functional theory calculations, that the adsorption of methane to the O^{2-} adsorbed PbS cluster is much more probable than its adsorption onto the pristine PbS cluster. Thus, PbS methane gas sensing abilities are higher under ambient air conditions than oxygen-free atmospheres and vacuum circumstances. [79] Even worse, without oxygen molecules on PbS, the adsorption of methane molecules would not be significant, as confirmed by the E_g values (see Table 1).

Table 1 - Electronic structure parameters of PbS cluster in four situations (all values are in eV)

Structure	LUMO	HOMO	E_g	Binding energy
PbS cluster	−1.856	−7.397	5.540	–
PbS/CH_4	−1.803	−7.338	5.535	0.176
PbS/O_2	−2.728	−7.289	4.560	0.971
$PbS/O_2/CH_4$	−2.559	−7.175	4.616	5.77

The **transducer** function is an interparticle issue, related to the change in height of the double Schottky barrier, resulting in changes in resistance of the sensors. It is accomplished by an intrinsic electronic property of the nanocrystal /or nanocrystal assembly, or through the application of an additional material (like graphene in a hybrid material, see Section 1.7). While the **utility factor** is an assembly issue, where physical aspects such as pore structures and film thickness influence the sensing performance, which determine the diffusion length of methane.

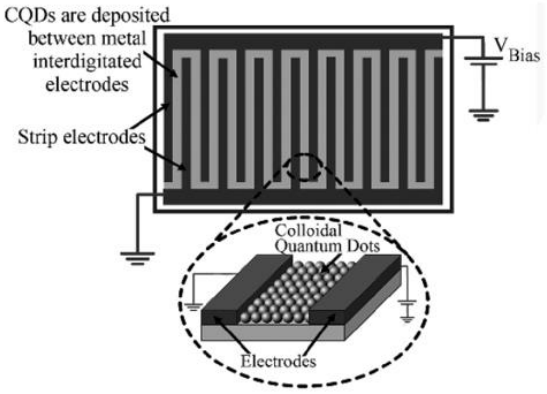

Figure 16. Photograph of implemented PCB Interdigitated Electrodes. [74]

In [59], the sensor is fabricated on a printed circuit board (PCB) and the sensing material is deposited on the Interdigitated electrodes (IDEs) as shown in Figure 16. IDEs are used to enhance system responsivity and sensitivity. The sensing properties will depend on the morphology of the deposited gas sensing material as mentioned in Section 1.3. The use of PCBs aims to integrate sensors with the corresponding electronic circuits, either for driving or readout purposes. The application of a bias voltage allows efficient charge separation between electrons and holes. In addition, this type of substrate provides excellent electrical isolation to prevent current leakage, making the sensor more reliable and sensitive.

1.7 Hybrid gas sensitive materials

Currently, most gas sensors and sensor arrays utilize sensing elements based on a single material or transduction mechanism. These rely on intrinsic sensing activity or additional thermal/photonic energy to drive the sensing effects of target gases. However, this approach, for both organic and inorganic-based materials, is not the best suited. Organic materials chemi-resisors suffer from short-term stability and sensitivity due to the affinity of conductive polymers towards volatile organic compounds (VOCs) and atmospheric humidity. [20] On the other hand, inorganic materials - based (especially metal oxide materials, e.g., ZnO, SnO, TiO_2, SnO_2) chemi-resistors require high operating temperatures, usually > 200 °C, and suffer from limited selectivity, baseline drift and oxidation/decomposition of VOCs. **A solution to these drawbacks involves the utilization of new gas sensitive materials based on hybrid inorganic-inorganic** [80],**organic-organic** [81], **and inorganic-organic materials**. [20] Thus, to optimize the chemi-resistive gas sensor's sensitivity, selectivity, and efficiency, it is often necessary to use **hybrid gas-sensitive materials** to achieve new and/or enhanced sensing properties. Using hybrid materials, which comprises complex constituents and novel

nanostructures, provides numerous advantages. Firstly, the abundance of hybrid materials is inexhaustible, and this allows for the optimization of many factors, such as surface-dependent, interface-dependent, and structure-dependent factors. This results in the creation of novel sensing behaviours [82]. Secondly, hybrid materials can implement more chemical and physical processes, which can lead to many improvements in gas detection. This is mainly achieved through catalytic reaction with analyte [83], charge transfer [84] manipulation of charge carrier transport [85], heterojunctions, molecular binding/sieving [86], and combinations of these mechanisms. These combinations can go up to five typical hybridizing forms which are categorized into three sensing-dependent factors: interface-, surface- and structure-dependent factor. [20]

The first combination, categorized as surface-dependent factor, involves catalysis reactions between analyte gas and decorating metal catalysts such as Pt [87] or Pd [88] on host semi-conductive materials. The second combination is a quick charge transfer process between guest additives and the host material through carrier withdrawal or donation, electron acceptor or donor.

The third is based on controlling charge carrier movement in a conductive/semi-conductive material (e.g., gold nanoparticles (GNPs)-thiols [89]) when exposed to gas analytes (classified as an interface- and structure-dependent factor). The fourth is based on the manipulation/construction of heterogeneous semi-conductive materials such as n-n, p-n, p-p, and p-n-p heterogeneous semi-conductive materials (categorized as interface-dependent factor). [90] The last one is based on semiconductors covered with gas molecular sieving/binding layers or ligands/complexes for selective gas detection (a surface- and structure-dependent factor). [86]

It is also possible to combine those five mechanisms between each other's. Indeed, Patricia A. Russo et al. for example reported that combining the catalytic effect of Pt nanoparticles with SnO_2/rGO is still highly sensitive to hydrogen concentrations of 3% and lower (compared to SnO_2/RGO devices) but exhibited shorter response and recovery times than those found for previously reported resistive hydrogen sensors based on graphene-based materials functionalized with Pt or Pd only. [91]

Reduced graphene oxide is commonly used in chemi-resistive-type sensors using fast charge transfer process since rGO is a highly conductive and promising material. There are different groups of graphene-based sensors.[48] The first one operates at room temperature and

graphene usually acts as the main sensing material. [92] Another category is the cases where metal oxides still act as the main sensing material, using hybrid materials. Indeed, they may increase the surface area, and as a result, analyte adsorption on the surface of graphene causes a difference in the conductivity of the metal-oxide/graphene hybrid. It is also possible for metal oxides to act as the sensing material but *at room temperature*. This metal-oxide-dominated hybrid is the 3rd group and has been observed with hybrids of copper-oxide/graphene.[93]

1.7.1 Reduced graphene oxide and PbS nanoparticles for methane gas sensing

A gas sensor that relies on a charge transfer process can be created by incorporating semiconductor nanoparticles, such as lead sulphide, onto rGO. [21] Previous studies [94] have reported on the gas sensing capabilities of lead sulphide, including research on the methane gas sensing properties of PbS NCs at room temperature. [74]

Roshan et al. proposed a PbS/rGO based chemi-resistor sensors for the detection of CH_4 as reported in [21]. Reduced graphene oxide flakes are expected to act as conductive flakes to enhance the sensing performance of sensors since graphene nanosheets, carbon nanotubes, and carbon combinations have been used in different studies to reduce working temperature and increase the sensing performance of sensors.[95] Moreover, graphene nanosheets provide interesting properties for the final gas sensor such as long-term stability and high conductivity. The goal is to enhance carrier transportation between neighbouring PbS NCs, which act as the receptor, by introducing rGO nanosheets, which act as the transducer, to the PbS nanocrystals since charge transfer is challenging. [21]

As explained earlier, the sensing mechanism occurring when PbS QDs meet methane gas is based on electron-holes combination which eventually leads to conductivity decreasing. Then, the charge transfer from these quantum dots to the rGO nanosheets relies on the heterojunction occurring within a rGO/PbS gas sensor and has been suggested by Hossein Roshan et al. [21] The conduction and valence bands in PbS nanocrystals (NCs) exhibit a 4.4 eV and 4.9 eV, energy levels, respectively and Fermi energy of PbS is close to its valence band. However, the work function of graphene falls within the range of 4.9 eV. Consequently, there will a transfer of the holes present in the rGO nanosheets to the lead sulphide NCs, leading to the equalization of Fermi levels, band bending of energy levels, and the expansion of a hole accumulation layer within the PbS NCs. Consequently, in a clean air environment, ionized oxygen is adsorbed on the surface of the NCs leading to the formation of the first accumulation layer, while the second accumulation layer is caused by the PbS/rGO heterojunction.[21] When exposed to a methane

environment, the desorption of ionized oxygen atoms results in the return of electrons to the conduction band of PbS. Consequently, the concentration of holes decreases. Mechanism is illustrated in Figure 17.

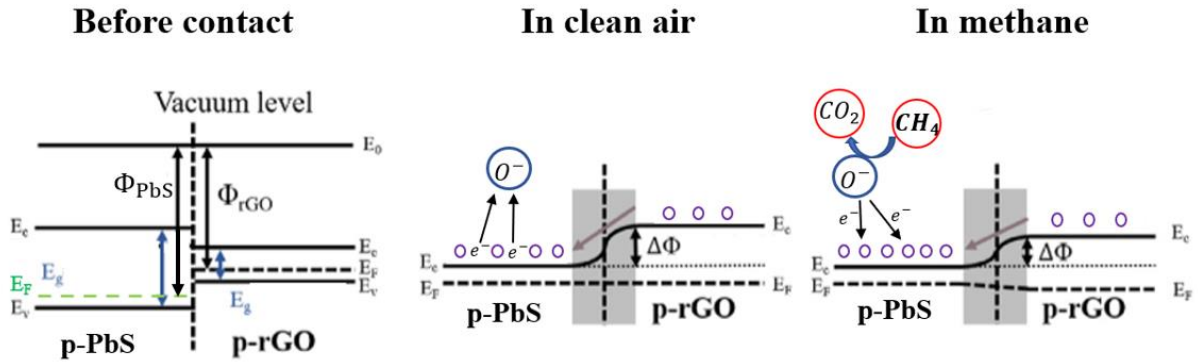

Figure 17. Band diagram of p-type PbS and p-type rGO before contact (left), rGO/PbS heterojunction in clean air (centre) and in CH_4 (right). E_F is the fermi level, E_c is the conduction band, E_v is the valence band, purple circles are holes and Φ is the working function.

The preparation method consists of one batch containing lead precursors (lead (II) nitrate) and graphite oxide. Then, 2-mercaptoethanol, acting as the capping agent, is slowly added to the mix solution. Eventually, the sulphur precursor (sodium sulphide) is added to the mixture dropwise for several hours under vigorous stirring and the solution is eventually washed, dried, and recovered. Afterwards, GO is hydrothermally reduced. In other words, PbS NCs/ GO is first synthetized followed by the reduction of GO, in situ. The resulting PbS/rGO nanocomposite methane sensor exhibited favourable sensing properties, including reproducibility, room temperature operation and the device composed of 3.5 % rGO exhibited the best results with high sensitivity to methane (up to 45% resistance change in 6% methane concentration), rapid response (90s), and a wide detection range (from 1000 to 60 000ppm).

Roshan et al. demonstrate that the more rGO added to nanocomposite, the smaller the electrical conductivity in the fabricated sensor. The electrical resistance reduced from 10 MΩ (in pure PbS sensor) to about 500 kΩ (in 3.5 wt% rGO sensor) as shown in table 2. [21]

Table 2 – PbS and rGO/PbS sensors properties

Sensor	Components	Average size of PbS NPs	Electrical resistance at RT	Best sensitivity	Response/recovery time	Detection range (ppm)	Reference
Pure PbS	0.1M 2-mercaptoethnaol 0.1M $Pb(NO_3)_2$ 0.1M Na_2S	40 nm	10 MOhms	47.6 %	180s/85s	10000-50000	[74]
PbS/rGO (3.5%wt rGO)	Identical + 1.05 mg GO	40 nm	500 kOhms	45%	92s/65s	10000-60000	[21]

1.8 Aim and challenges of the Master Thesis

The aim of the Master Thesis is to provide a solid-state methane gas sensor based on lead sulphide nanocrystals on top of reduced graphene oxide flakes and eventually combine these two materials by using an ink-jet printer to print them on interdigitated electrodes (IDEs). The whole device is expected to provide an effective sensitivity to methane gas while involving simple, easy synthesis protocols and processes of the sensing materials. Moreover, despite the inherent toxicity of lead components [96] and organic solvents like NMP [97], deliberate efforts are being made to prioritize the environmentally friendly aspect of the process employed in this work.

As mentioned earlier, graphene-based materials are a promising material for sensing and adsorbing molecules due to their good adsorbing properties and reactive functional groups on their area. Reduced graphene oxide recovers the electronic properties by recovering sp^2 carbons and thus can act as a conductive layer. On the other hand, PbS is a cheap component and its PbS nanocrystals, with their large surface-to-area ratio, are sensitive and selective to methane. [74] The most interesting aspect of the synthesis technique used in this Master Thesis is that it allows to tune and characterize each material separately before the printing and therefore, allowing an infinity of combinations.

The main focus of the Master Thesis is on the synthesis of PbS nanoparticles which must display a pure surface, a well-controlled size and a good dispersion. The synthesis protocol for the reduction of graphene oxide is meant to be easy to reproduce, simple, the least polluting as possible and fast. The concrete goal is to have as much PbS nanocrystals as possible to cover the rGO flakes and hence to get a good dispersion on flakes. This part of the work is done in

the MOST research unit at UCLouvain where the role of the Prof. Sophie Hermans laboratory is first the size and purity-controlled preparation of the nanoparticles and their characterization via multiple analysis techniques such as XRD or Raman spectroscopy for example. Both materials are expected to be integrated on the IDEs, deposited on an oxidized silicon substrate via a manual deposition technique of adequate dispersions of both materials. These deposited materials on IDEs are investigated through resistance measurements. This part of the work is done in the NAPS (Nanoscopic Physics) research unit at UCLouvain where the role of the Prof. Benoît Hackens laboratory is the analysis of the resistance and gas sensing properties of the integrated devices.

Eventually, the focus of this project is to unravel the methane sensing mechanism, which poses a significant challenge due to the multitude of factors that affect the resistance variations. One of the key difficulties that has been explored in the literature is the ability of methane to react with or absorb ambient moisture [98] and its cross-sensitive sensitivity to other analyte gas such as VOCs, NO_2, and CO which are typical interfering gases. [99] Moreover, several factors such as the morphology, dispersion, purity, and crystallinity of lead sulphide nanoparticles can impact the conductivity. Additionally, rGO must act as a conductive layer and is not expected to be the sensing material. [8]

Overall, this study looks at the capacity of PbS nanoparticles, combined with rGO, to detect methane gas molecules efficiently and selectively. In practice, it investigates the morphology, dispersity, size, and purity of PbS nanoparticles and how its combination with the most reduced graphene oxide is playing on the resistance behaviour and on the methane sensing. Ultimately, the perfect combination could be used with an ink-jet printer to deposit sensitive materials on IDEs.

1.9 Methodology

To accomplish the research goals and address these scientific inquiries, the experimental work has been partitioned into three primary stages.

The **first stage** was the synthesis of reduced graphene oxide and lead sulphide nanoparticles as well as their respective characterization.

First, the reduction of the commercial graphene oxide coming from Graphenea was performed either with deionized water at 80°C and at 90°C, either with the organic solvent N-Méthyl-2-pyrrolidone at 80°C and at 200°C to evaluate the efficiency of the reduction process. In addition,

vitamin C is utilized as the reducing agent, and two distinct concentrations are tested to assess the reduction rate. To compare the reduction rate of the different rGO, each sample undergoes analysis with both FTIR and Raman spectroscopy. Since these two characterization methods are qualitative, we utilize a combination of them to ensure the precision of our findings and XPS analysis is performed to calculate the O/C ratio as well as the sp^2/sp^3 carbons ratios. Additionally, TGA analysis was conducted on various rGO samples to study their thermal behaviour and DFT calculations were performed to study the DOS and bandgap of pristine graphene, graphene with hydroxyl, graphene with epoxy and graphene with epoxy and hydroxyl groups.

The second step of this first stage is the synthesis and the characterization of PbS nanoparticles. The method was an injection method and consisted of the injection of a sulphur precursor solution (sodium sulphide in DI water) into a lead precursor solution, (lead (II) nitrate in DI water) at different dripping speeds using an automatic syringe. Synthesis of the nanoparticles was carried out with and without the use of 2-mercaptoethanol as a capping agent, and a comparison was conducted between the two methods. All synthesis were performed under inert atmosphere and all samples were washed and dried. A second synthesis method was performed, consisting of one batch of lead and sulphur precursors in the presence of sodium borohydride as the reducing agent. This second method is expected to synthesize nanoparticles with a different shape than the 1st protocol described above. X-ray diffraction (XRD) and X-ray fluorescence (XRF) were utilized to characterize the PbS nanoparticles and ensure their crystallinity and molar ratio, respectively. Inductively coupled plasma (ICP) has been used as a second method to measure the molar ratios. Subsequently, Scanning Electron Microscopy (SEM) and Transmission Electron Microscopy (TEM) were conducted to verify the dispersion, size, and shape of the nanoparticles.

The **second stage** consisted in the selection of rGO samples and PbS samples to be deposited on the interdigitated electrodes for the sensor. Four PbS samples were chosen based on the molar ratios determined by XRF and ICP analysis. Additionally, these four PbS samples were examined with DR-spectroscopy to determine the bandgap energy. On the other hand, the most highly reduced graphene oxide sample is selected according to its FTIR, Raman spectroscopy and XPS analysis to ensure the highest reduction rate compared to the other samples.

The **third and last stage** was the deposition on the sensing layer followed by resistance tests and gas sensing measurements. One of the chosen PbS samples was initially deposited onto four IDEs on a die by using drop-casting. Before that, the electrical resistance of this chosen PbS was measured while dropcasting and data was gathered at that moment. This preliminary dropcasting session aimed to determine the number of droplets of PbS dispersion required per electrode. While the number of droplets of rGO that will be deposited on IDEs, is chosen arbitrarily because no preliminary dropcasting session was performed.

Next, resistance, and corresponding IV curves, of one of the four selected PbS samples and one rGO sample were collected with a four-point probe technique, the PM8PS probe station, to verify that the values did not exceed hundreds of Mega Ohms. Subsequently, the remaining PbS and rGO samples were individually drop-casted and their resistance were measured by using PM8PS. Ultimately, the two PbS samples with the lowest resistance, since the highest conductivity within the sensor is required, were selected and their dispersions were deposited onto dies where rGO was already deposited. Furthermore, one PbS sample, one rGO sample, and a rGO/ PbS mixed sample were analysed to study the variation of resistance with temperature and to investigate the conductivity regime through the materials.

The two rGO/PbS die as well as a PbS die and a rGO die are bonded on a DIL-16 package (as shown in Figure 23) and are analysed under a methane calibration gas containing 2.5 volumetric % of methane, 20.9% O_2 in N_2 for a preliminary gas sensing.

The last step is the gas sensing measurements with different concentrations of methane to determine the degree of sensitivity of the sensor's devices.

II. EXPERIMENTAL METHODS

This section provides an overview of the chemicals employed in the study, along with the characterization methods utilized. Additionally, detailed descriptions of the synthesis protocols for reduced graphene oxide (rGO) and PbS nanoparticles are provided. This section also covers the preparation of sample dispersions, cleaning and preparation of the dies, deposition technique, and explanation of resistance and gas sensing measurements.

2.1 Chemicals

Multiple chemicals were used in this work and are shown in Table 3. Milli-Q water, deionized water and N-Methyl-2-pyrrolidone were used as solvents. Lead(II) nitrate, sodium sulphide and 2-Mercaptoethanol were utilized as lead source, sulphur source and capping agent, respectively. For the 2nd protocol, lead chloride, sulphur, and borohydride were also used as reagents. Chemical reduction was performed with L(+)-Ascorbic acid dissolved in NMP or in milli-Q water. The graphene oxide source comes from Graphenea and was then reduced in this work to obtain rGO.

Table 3 - Chemicals employed in this work

Chemical	Chemical formula	Supplier	Additional information
Sodium sulphide	Na_2S	Sigma-Aldrich	98% pure Water soluble
Lead(II) chloride	$PbCl_2$	Sigma-Aldrich	≥ 98.0 % Powder
Lead(II) nitrate	$Pb(NO_3)_2$	Sigma-Aldrich	99.999% trace metals bases, Water soluble
2-Mercaptoethanol	C_2H_6OS	Sigma-Aldrich 14.3 M (pure liquid),	14.3 M (pure liquid) Reagent grade
Graphene oxide	-	Graphenea	Powder
L(+)-Ascorbic acid (Vitamin C)	$C_6H_8O_6$	VWR Chemicals	99.0-100.5% USP
Sulphur	S	Sigma-Aldrich	99.998% trace metals basis, Powder
N-Methyl-2-pyrrolidone	C_5H_9NO	Acros Organics	HPLC Solvent
Methanol	CH_3OH	VWR Chemicals	Technical

Sodium borohydride	$NaBH_4$	Sigma-Aldrich	Reagent Plus 99%
Absolute ethanol	CH_3CH_2OH	VWR Chemicals	AnalaR NORMAPUR® Reag. Ph. Eur
Ink solution			
Cyrene (Dihydrolevoglucosenone)	$C_6H_8O_3$	Sigma-Aldrich	Biorenewable
Isopropanol	$(CH_3)_2CHOH$	VWR Chemicals	≥97%
Milli-Q Water	H_2O	VWR Chemicals	Milli-Q® IQ 7000
Milli-Q water	H_2O	VWR Chemicals	Milli-Q® IQ 7000
Acetone	C_3H_6O	Fisher Chemical	Extra dry, for synthesis

2.2 Reduction of graphene oxide

2.2.1 Water-based solvothermal reduction of GO

40mL of deionized water is degassed with Argon. Then, 7.0505g of L-ascorbic acid is added to the degassed water for stirring under gentle heating for solubilisation.

GO powders provided by Graphenea were dispersed in Milli-Q water with a concentration of 20.4 mg/mL. Then, to break the clustered GO, to improve the dispersion of GO sheets and to reduce the dimensions of the biggest GO flakes, ultrasonic treatment (USC1200D, VWR International) at 45 kHz and 60 W was performed for about 15-30 minutes. After, the GO dispersion was added into the Vitamin C solution and left under stirring for 1h. To remove the byproducts and residuals, the mixture was centrifugated (6000 rpm for 15 minutes) and washed with milli-Q water, acetone, methanol, and milli-Q water once again. One centrifugation cycle was carried out between each washing to recover the solid product by decanting the supernatant. The product is eventually dried in a vacuum oven at 50°C overnight.

2.2.2 NMP-based Solvothermal Reduction of GO

7.0505g or 3.525g of L-ascorbic acid (vitamin C) is added to 40 mL of N-methyl-2-pyrrolidone (NMP) and the solution is stirred under gentle heating (around 30-35°C) for solubilisation. GO powders provided by Graphenea were dispersed in Milli-Q water with a concentration of 20.4 mg/mL. Then, to break the clustered GO and therefore to improve the dispersion of GO sheets, an ultrasonic treatment (USC1200D, VWR International) at 45 kHz and 60 W was performed for between 15 and 30 minutes. Afterwards, the GO dispersion was added into the mixture NMP-Vitamin C (0.8M or 0.4M) and left under stirring for 1h. To remove the byproducts and

residuals, the mixture was centrifugated (6000 rpm, 15 minutes) and washed with milli-Q water, acetone, methanol, and milli-Q water once again. One centrifugation cycle was carried out between each washing to recover the solid product by decanting the supernatant. The product is eventually dried in a vacuum oven at 50°C overnight. All conditions tested are summarized in Table 4 below.

Table 4 - Details about the tested GO reductions

Sample	Solvent	Temperature (°C)	Vitamin C
NMP 80 (full)	N-methyl-2-pyrrolidone	80	Yes (0.8M)
NMP 200 (full)	N-methyl-2-pyrrolidone	200	Yes (0.8M)
NMP 200	N-methyl-2-pyrrolidone	200	No
Waterbased 80	Water	80	Yes (0.8M)
Waterbased 90 full	Water	90	Yes (0.8M)
Waterbased 90 half	Water	90	Yes (0.4M)

2.3 Synthesis of the PbS nanoparticles

Lead sulphide nanoparticles were synthetized following two different synthetic routes to investigate the impact of the precursors, the injection method, the temperature and the solvent on the morphology and the chemical and physical properties of synthesized nanoparticles.

2.3.1 Protocol n°1

PbS nanoparticles were prepared as following: 250mL of deionized (DI) water is degassed for about 30 minutes. In the meantime, a triple-neck glass flask is purged with argon to be put into inert atmosphere. 1.57g of $Pb(NO_3)_2$ is dissolved in 50mL DI water, giving a concentration of 0.1M, and poured into the triple-neck flask under stirring (350 rpm) at room temperature. Then, 0.7mL of 2-Mercaptoethanol is dissolved in 99mL of deionized water, forming a 0.1M solution, and is dripped slowly into the lead nitrate solution during one hour with an automatic syringe. 360 mg of sodium sulphide is dissolved in 50 mL of DI water, giving a concentration of 0.1M, and stirred for about 5 minutes. Afterwards, the sodium sulphide solution is slowly dropped into the mix 2-mercaptoethanol/lead nitrate solution for a certain time with an automatic syringe. Dripping times tested are shown in Table 11, Section 3.2. When the sulphide was totally added, the mixture is put under stirring for approximately one hour for ripening. To remove the by-products and residuals of the organic capping agent, as the presence of organic residues on the surface of NPs may be detrimental to the gas sensing properties, the mixture

was centrifugated (6000 rpm for 15 minutes) and washed with milli-Q water, acetone, methanol, and milli-Q water once again. One centrifugation cycle was achieved between each washing to recover the product. The product is eventually dried in a vacuum oven at 50°C overnight. The theoretical yield of the reaction is 1.11 g of lead sulphide. PbS NPs are synthesized following this equation:

$$Pb(NO_3)_2 + Na_2S \rightarrow PbS\ (s) + 2\ NaNO_3$$

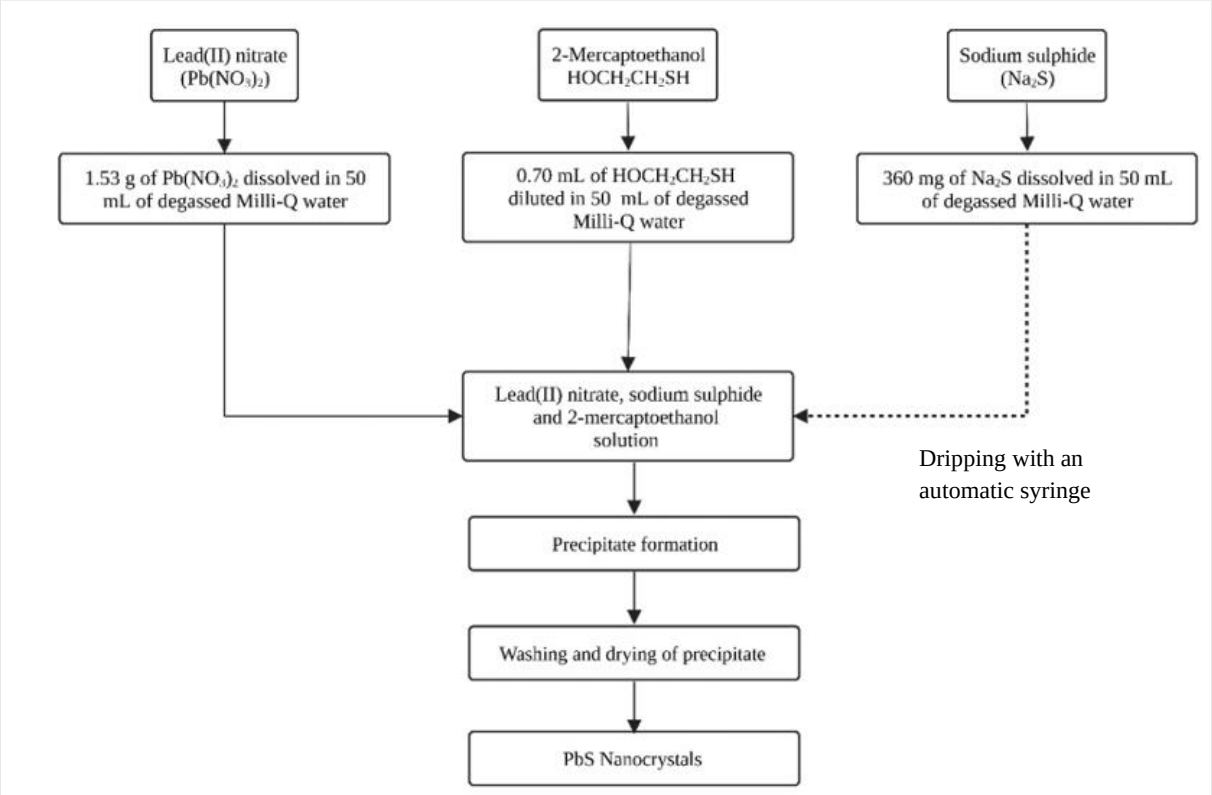

Figure 18. Flow chart of the PbS nanocrystals synthesis using the 1st protocol [100]

2.3.2 Protocol n°2

PbS nanoparticles were also prepared from lead chloride, sulphur powder and varying the chemical reagent sodium borohydride in two different molar ratios, namely 1:1:1 and 1:1:3.

In case of 1:1:1 ratio, 60 ml ethylenediamine was poured in a beaker together with 2.78 g PbCl2 , 0.32 g S and 0.37 g NaBH4 and kept under stirring at 40°C for 4 hrs. Then the solution was centrifuged, washed with milli-Q water PbS, acetone then with milli-Q water once again and the solid was then dried in a vacuum oven at 50°C. The nano powder was collected after drying. This same procedure was followed for the ratio 1:1:3, adapting the amounts of reactants as shown in Figure 19 below. PbS NPs are synthesized following this equation:

$$PbCl_2 + S + 2\ NaBH_4 \rightarrow PbS\ (s) + 2\ NaCl + B_2H_6 + 2H^+ + 2e^-$$

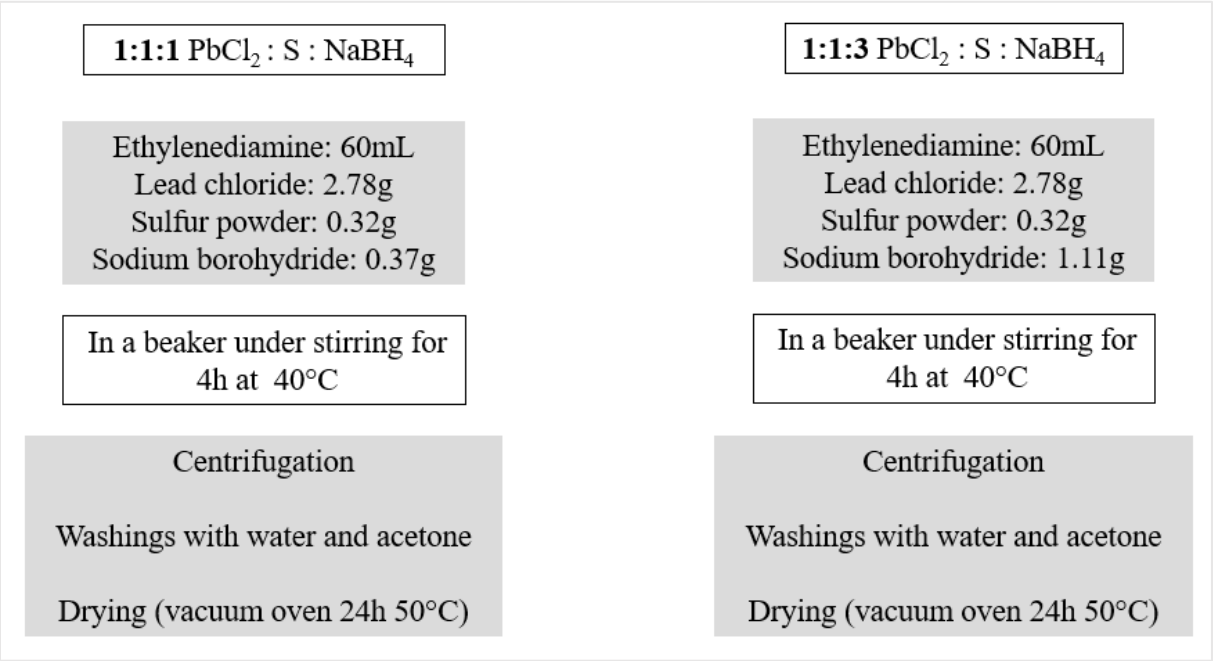

Figure 19. Flow chart of the PbS nanocrystals synthesis using 2nd protocol

2.4 Sample dispersions

The best PbS samples (the selection method is explained in Section 1.9) and the most reduced rGO sample were dispersed in an appropriate solvent as described below.

2.4.1 PbS sample dispersions

PbS samples were dispersed in milli-Q water at a concentration of 5 to 15 mg/mL and were sonicated with an ultrasound tip (Fisherbrand™ Model 120 Sonic Dismembrator) for 10 min at 120W, 20 Hz, pulsed mode, full power. Just before the dropcasting, each PbS sample was stirred 30s with a Vortex (VWR international, Bio-Chim tuber shaker VWR, 2014 EQ142 at the maximal speed) and then was left to rest for one or two minutes.

2.4.2 rGO dispersions

2.5 mg of rGO sample was dispersed 25mL of an ink solution to form a 0.1mg/mL dispersion. The ink solution is composed of 50mL of Cyrene, 40mL of IPA and 75mL of MQ water and is a well-suited solution for ink-jet printer as its viscosity perfectly matches the printer requirements. Therefore, it allows an optimal printing. The rGO suspension was sonicated with an ultrasound tip (Fisherbrand™ Model 120 Sonic Dismembrator) for 10 min at 120W, 20 Hz, pulsed mode, half power. Just before drop-casting, the rGO sample was stirred 30s with a

Vortex (VWR international, Bio-Chim tuber shaker VWR, 2014 EQ142 at the maximal speed) at the maximal speed and then was left to rest for one or two minutes.

2.5 Preparation and cleaning of the dies

The CMOSEnvi™ dies were created by VOCsens, by using an oriented silicon layer that is 380 µm thick and N-doped with phosphorus to have a resistivity of 2-3 Ω·cm. A layer of silicon oxide, 300 nm thick, was grown on top of the silicon layer. The dies were coated with a protective blue layer then Ti:Au (200:2000 Å) metallic lines were patterned on top of the insulating layer with a 2 µm width and a 5 ± 1 µm gap between them. Afterwards, the protective blue layer was removed by soaking them in an 80°C acetone bath. The dies were then washed with methanol and then deionized water to ensure a clean surface. These CMOSEnvi™ dies (patented VOCSens) were, in this work, mainly utilized as substrates to produce the final devices. A schematic drawing of the dies is shown in Figure 20 and their dimensions are detailed in Table 5. The two electrodes situated in front of the VOCsens logo are referred to as the big and small electrodes "S", while those located in front of the other logo are named big and small electrodes "M". All electrodes are designed for deposition of sensing layers, but these eight "M" and "S" electrodes (and the skinny electrode, but not used in this work) are designated for the dropcasting as well as for the ink printing, while the other electrodes are used for electro polymerization.

2.6 Deposition technique

Both reduced graphene oxide and lead sulphide nanocrystals dispersion were deposited on dies by drop casting are described below.

Table 5 – Details about the interdigitated electrodes (IDEs) [100]

Electrodes	Number of fingers	Length (L) [µm]	Height (H) [µm]
(a)	150	500	1050
(b)	50	250	350
(c)	50	50	350
(d)	50	200	250
(e)	15	50	60

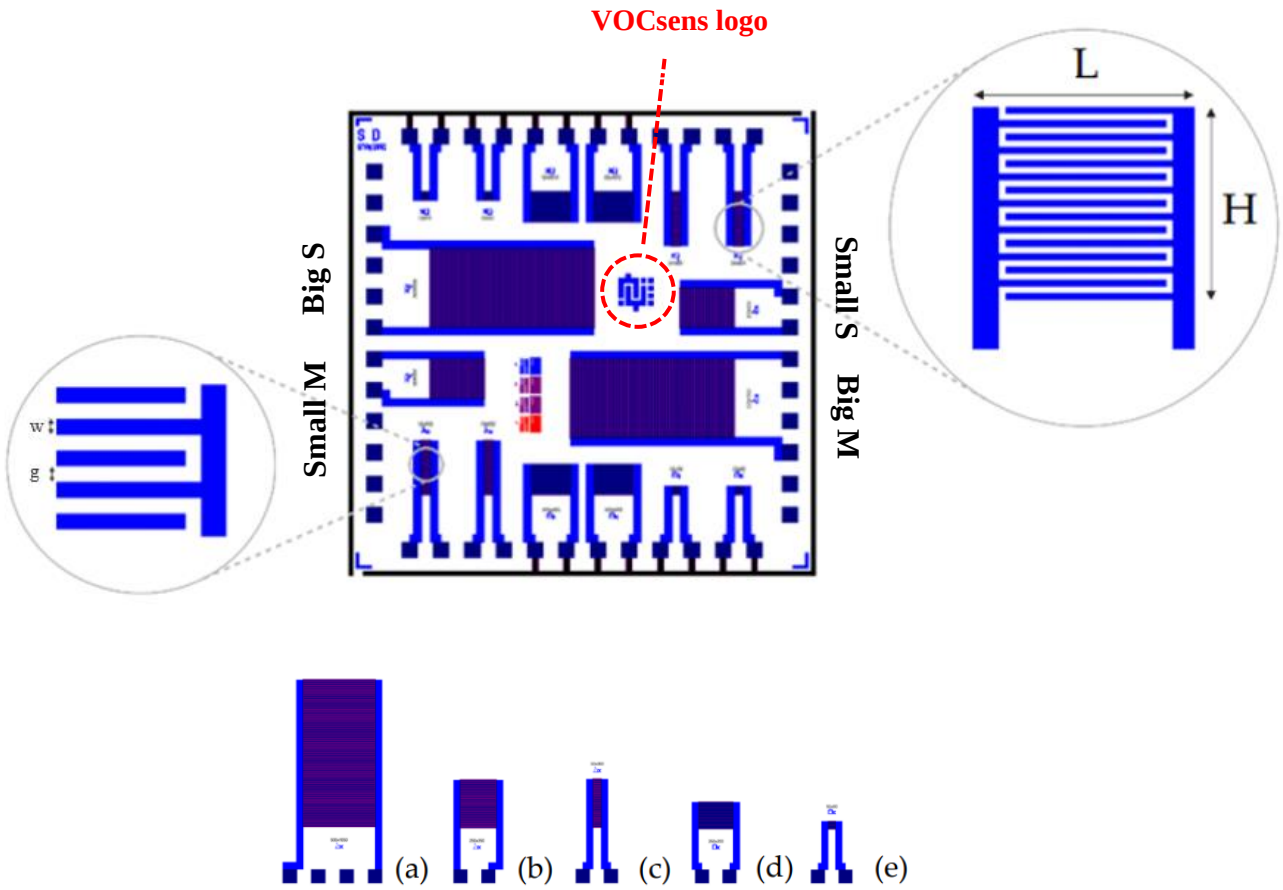

Figure 20. Schematic view of the IDEs used in this work. Big (a), Small (b) Skinny (c) Electro-polymerization Electrodes (d)(e) [100]

The dropcasting station is shown in Figure 21 and is provided with a bench stereomicroscope, a sample platform and two lamps, along with a ceramic heating element. On top of the latter, the die was sticked or not, with a small amount of conductive silver paste, if necessary. A power supply unit (RSPD 3303C) and a digital multimeter (DMM) (RSPD 3303C), were connected to the heating element together with a thermocouple. The syringe used to drop cast the solution is a 0.3 mL insulin syringe with sterile interior, with a straight cut needle of 0.25 mm in diameter. The produced droplets can have a volume between few µL to hundreds of nL.

For each PbS sample, 180 drops were deposited on big electrodes (electrode a) and 160 drops on small electrodes (electrode b). For each rGO sample, 25 drops were deposited on big electrodes (electrode a) and 16 drops on small electrodes (electrode b). For the dies made of both PbS and rGO, the rGO flakes were first deposited, 25 drops on big electrodes (electrode a) and 16 drops on small electrodes (electrode b), then PbS nanoparticles were added on top of the rGO flakes, 180 drops on big electrodes (electrode a) and 160 drops on small electrodes (electrode b). Each die was eventually dried at 110°C for one hour, to remove any trace of solvent.

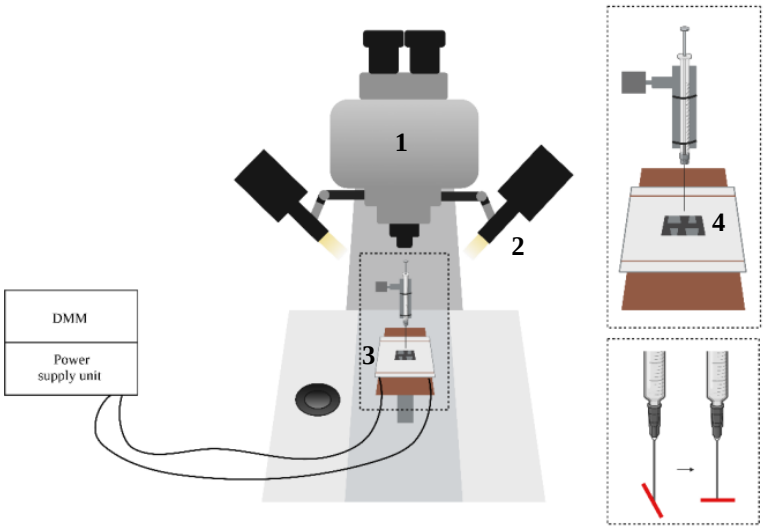

Figure 21. Schematic view of the dropcasting station. Stereomicroscope (1), lamps (2), ceramic heating element (3) die (4). [100]

2.7 Characterization methods

In this section, the characterization techniques will be discussed. First, FTIR and Raman Spectroscopy were used to investigate the structural properties and the defectivity the reduced graphene oxide flakes. Carbon/oxygen ratio and degree of graphitization were studied through X-ray photoelectron spectroscopy. Thermal behaviour of reduced graphene oxide and PbS nanoparticles was studied through Thermogravimetric Analysis (TGA). Also, density of states and band structures of reduced graphene oxide were calculated with density functional theory (DFT). Then, X-ray fluorescence spectroscopy (XRF), Inductive coupled plasma (ICP) and powder X-ray diffraction (XRPD) were utilized to check the composition and verify the crystallinity of the lead sulphide nanoparticles, respectively. Finally, resistance and gas sensing measurements were achieved with point probe measurement and a gas sensing station, respectively.

2.7.1 Fourier-Transform Infrared Spectroscopy (FTIR)

Samples were analysed with a Nicolet™ iN10 MX Infrared Imaging Microscope expanded with the Thermo Scientific Nicolet iZ10 FTIR Module to work with standard sample-compartment accessories and full spectrometer capabilities. The equipment allows for the analysis of samples down to 10 microns with the onboard spectrometer. Samples (in pellet form with KBr) were analysed with high-resolution, in a cooling mode (provided by liquid nitrogen) in transmission mode with a detected signal by an MCT-A detector, an ultra-fast mapping that can collect 10 spectra per second.

2.7.2 Raman Spectroscopy

Equipment n°1 (Boltzmann Building)

Raman analyses were carried out with a DXR3xi Raman Imaging Microscope (Thermo Scientific™), in the dark. The sample in powder form is spread on a glass plate and placed under the microscope. The incident light, having a wavelength of 532 nm, is sent on the sample with a 5mW power and an exposure time of 1s, automatically exposed 15 times to enhance the signal to noise ratio.

Equipment n°2 (Welcome Area in Maxwell Building)

Raman analyses were also done with Horiba Jobin Yvon Technology, Raman Division, LabRam HR 2013 EQ 103 instrument, in the dark or in the light. The sample in powder form is spread on a glass plate and placed under the microscope. The incident light, having a wavelength of 514 nm, was used at 10% of power and an acquisition time of 20s.

2.7.3 Scanning electron microscopy (SEM)

SEM images were obtained with a Zeiss Auriga FIB-SEM providing a high-resolution. The SEM features Schottky field emission Gemini electron column operating between 100V and 30kV, capable of resolutions of 1.0nm at 15kV and 1.9nm at 1kV. The system is fitted with a standard in chamber ET detector, and two in column detectors, in the form of an in-lens SE detector and an energy selective backscattered electron detector. In practice, the solid-state dies are introduced in the SEM equipment and analysed as such.

2.7.4 X-Ray Fluorescence (XRF)

Dried lead sulphide powders have been analysed on a SPECTRO XEPOS energy dispersive X-ray fluorescence (ED-XRF) spectrometer by Dr. Koen Robeyns, provided with a palladium and cobalt anode in the X-ray tube, to evaluate the ratio between lead and sulphur (1 was the target ratio, corresponding to the molar ratio between lead and sulphur in the asymmetric PbS unit). The XRF spectrometer detector was kept at -30°C. Data were acquired between 0 keV and 70 keV. It is worth noting that organic traces are difficult to be identified through X-ray fluorescence spectroscopy. The spectrometer was calibrated using a commercial pure PbS sample, following instructions from the supplier of the instrument.

2.7.5 X-Ray Photoelectron Spectroscopy (XPS)

XPS analyses were carried out by Pierre Eloy at room temperature with a SSI-X-probe (SSX 100/206) photoelectron spectrometer from Surface Science Instruments (USA), equipped with a monochromatized microfocus Al X-ray source. A few milligrams of each sample were stuck

onto small sample holders with double-face adhesive tape and then placed on an insulating ceramic carousel (Macor®, Switzerland). Charge effects were avoided by placing a nickel grid above the samples and using a flood gun set at 8 eV. The binding energies were calculated with respect to the aliphatic C-(C,H) component of the C1s peak fixed at 284.8 eV. Data treatment was performed using the CasaXPS program (Casa Software Ltd., UK). The peaks were decomposed, after subtraction of a Shirley-type baseline, into a sum of GL(15) Gaussian/Lorentzian components with the A(0.35,0.35,20)GL(50) specific asymmetric shape in the case of the aromatic C-(C,H) component.

2.7.6 Transmission Electron Microscopy (TEM)

TEM images were recorded by Dr. Fabien Drault on a LEO 922 OMEGA Energy Filter Transmission Electron Microscope operating at 120 kV. Samples are dispersed in absolute ethanol and sonicated with an ultrasound bath for 10 minutes, then they are dried overnight. Afterwards, samples are deposited on C-flatTM thick grids (Standard 20 nm Carbon, 1.2 µm hole diameter and 1.3 µm hole spacing with a 200-mesh copper grid, Protochips).

2.7.7 Optical Microscopy

Optical Images of the sensing materials deposited on IDEs were obtained with the Zeiss Axio Imager Vario A2, a research microscope with a wide range of incident light techniques and equipped with a CCD camera. 10X, 20X and 50X objective magnifications were applied and their specifications are listed in Table 6.

Table 6 – Specifications of different objective magnifications of optical microscope [101]

Objective magnification	Max. capture range in µm (reflective, bright surface)	Maximum precision of focus position (accuracy) (~0.3 times the objective's depth of field), in µm	Minimum size of the object to be brought into focus, in µm
1.25×	>12,000	~170.00	~2,000
2.5×	>10,000	~42.00	~1,000
5×	>10,000	~8.90	~500
10×	>8,000	~2.50	~250
20×	>4,000	~0.60	~125
50×	>700	~0.25	~50
100×	>150	~0.20	~25

2.7.8 X-Ray Powder Diffraction (XRPD)

By Koen Robeyns (analyses done for all PbS samples of this work, except Section 6.3)

X-ray diffraction patterns of powders were recorded by Koen Robeyns on a D8 Advance (Bruker, USA) diffractometer with a Bragg Brentano geometry using a power of 1200 W (40 kV, 30mA), equipped with a copper source ($\lambda_{K\alpha}$ = 1.5409 Å) and a LynxEye XE-T detector. About ten milligrams of each sample were deposited on a PMMA sample holder. Data were collected in the 2θ range from 5° to 80°, with a step of 0.015° and a time/step of 0.15 s at room temperature. The obtained 2D diffractograms were analysed using DIFFRAC.EVA software (Bruker, USA). The PbS particles sizes (d_{XRD}) were extracted from XRPD measurements by using the Scherrer equation [102]

$$d_{XRD} = k\,\lambda/(B\cos\theta) \quad \text{(Equation 1)}$$

where k is a constant taken as 0.9 here, λ is the wavelength of X-ray radiation ($\lambda_{K\alpha}$ = 1.5409 Å), θ is the diffraction angle and B is the line width at half maximum height. The (111) diffraction line of lead sulphide crystallites was used to determine the B and θ values.

By Timothy Steenhaut (analysis done for the PbS sample shown in Section 6.3)

Lab PXRD analyses were performed using a MAR345 diffractometer with X-rays generated by an Incoatec Microfocus Source HIGHBRILLIANCE (IμS HIGHBRILLIANCE) Mo ELM47 operating at 50 kV and 1000 μA (λ= 0.71073 Å). Powdered samples were loaded in glass capillaries (0.7 mm, Hilgenberg GmbH) and diffraction data were integrated using the Fit2D software (a 0.1 mm diameter capillary filled with LaB6 was used as a calibrant).

2.7.9 Thermogravimetric Analysis (TGA)

Thermograms were recorded using a TGA/SDTA 851e instrument from Mettler Toledo. Samples (2-10 mg) in alumina containers were heated at 10 °C/min under an air flux (100 mL/min) from 25 to 850 °C.

2.7.10 Density Functional Theory Calculations (DFT)

Density of states and band structures of rGO were calculated by Prof. Fouad El Haj Hassan Director of PRASE from the Lebanese University – Doctorate School for Science and Technology. DFT was carried out by using Quantum espresso program. Quantum espresso is a suite of computational codes, for electronic structures and materials modelling, based on density functional theory, plane wave basis and ultrasoft conserved norm pseudopotentials.

2.7.11 Inductive Coupled Plasma Optical Emission Spectroscopy (ICP-OES)

ICP analyses were done one PbS samples with a Varian Vista MPX ICP-OES system by MEDAC LtD analytical, a chemical consultancy services company in the UK. MPX megapixel

detector, provides over 1.1 million pixels in a CCD array detector design and the technique has full wavelength coverage.

2.7.12 Diffuse Reflectance UV visible Spectroscopy (DR-UV-vis)

PbS samples were analyzed, in a powder form, by the spectrophotometer UV-3600i Plus UV-Vis-NIR by Shimadzu, in absorbance mode with wavelengths ranging from 200nm to 800nm and detected by a photomultiplier tube as the detector in collaboration with Dr Fabien Drault.

2.7.13 Resistance measurements

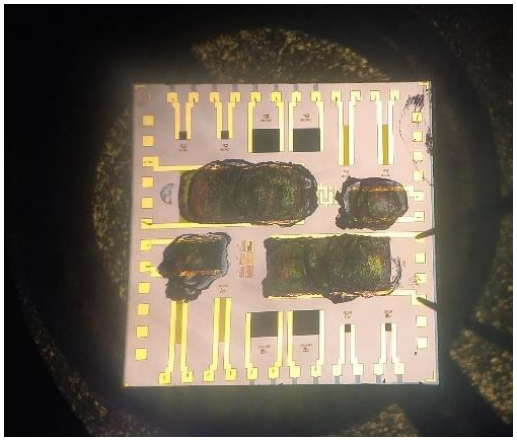

Figure 22. Die with deposited materials and probers placed on gold contacts (on the right)

After the deposition of the dispersions on the IDEs, resistance measurements were performed, on each of the four interdigitated electrodes. The measurements were carried out with the B1500 semiconductor analyser and the four-point prober PM8PS, (Low Signal probe station with Probeshield) provided with thermal chuck (300°C) for IV and CV measurements. The probes are shown in Figure 22. All IV measurements were done with a voltage from -1V to 1V and a current compliance of 10mA. Resistance measurements as a function of temperature were carried out with the thermal chuck.

The dispersions of the least resistive PbS dies (PbS 4 and PbS 14) were deposited on new dies and measured again, to check the reproducibility of their resistance values (PbS 4b and PbS 14b). All mixed dies (with both PbS and rGO on it) were first measured with the rGO flakes only (rGO 3 and rGO 4) then measured again when PbS nanoparticles were deposited on top (becoming rGO 3b and rGO 4b).

Also, measurements of resistance as a function of temperature (25°C up to 200°C, with steps of 25°C) were performed for some of the samples. To avoid any undesirable oxidation effects (as explained in section 3.2.4) of the materials, these samples were not chosen for the final sensor's devices. The achieved resistance measurements are listed in Table 7 and selected samples for subsequent gas sensing are highlighted in grey.

Table 7 - Resistance measurements

Sample	Composition	Resistance test in temperature
PbS 4	PbS 4	Yes
PbS 4b	PbS 4	No
PbS 6	PbS 6	No
PbS 10	PbS 10	No
PbS 14	PbS 14	No
PbS 14b	PbS 14	No
rGO f	rGO NMP 200	Yes
rGO 1	rGO NMP 200	No
rGO 2	rGO NMP 200	No
rGO 3	rGO NMP 200	No
rGO 4	rGO NMP 200	No
rGO 3b	rGO 3 + PbS 4	No
rGO 4b	rGO 4 + PbS 14	No
rGO 1b	rGO 1 + PbS 4	Yes

2.7.14 Gas sensing measurements

Gas sensing measurements were done with the setup gas KEYSIGHT, DAQ970A for data acquisition and were performed on the four selected samples (rGO 3b, rGO4b, rGO 2, PbS 14b). The dies were bonded on DIL-16 package (see Figure 23) and connected to the board for gas sensing (see Figure 24).

i. Preliminary gas sensing

After the bonding (Figure 23), the dies were placed on the board (Figure 24) and then were measured with the gas sensing station under a flow of oxygen calibration gas composed of 20.9% O_2 in N_2 in a 110L canister (69 bars), produced by © 2023 Air Products and Chemicals, Inc. Then, a methane calibration gas composed of 2.5% Methane and 20. 9% O_2 in N_2 in a 110L canister (69 bars) produced by Air Products, is applied on the sensor. Protocol is a flow-through technique [103] and is described in Figure 25.

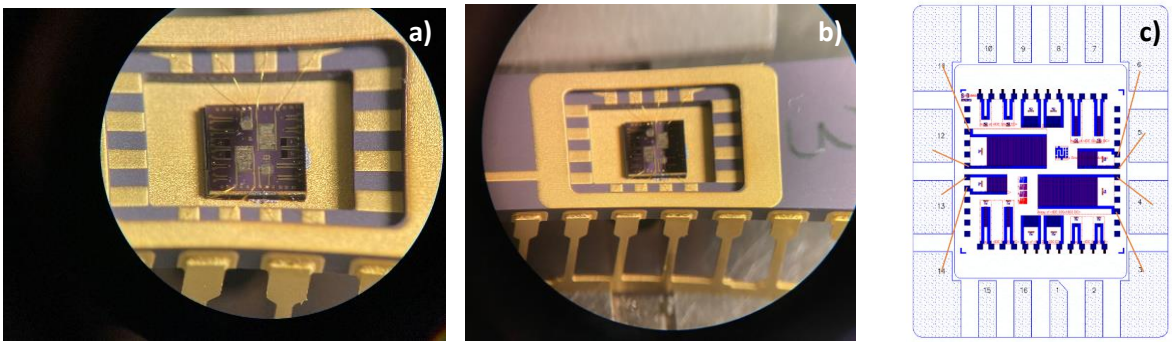

Figure 23. Wire bonding of sensors on the DIL-16 packaging a-b) Schematic of the wire bonding c)

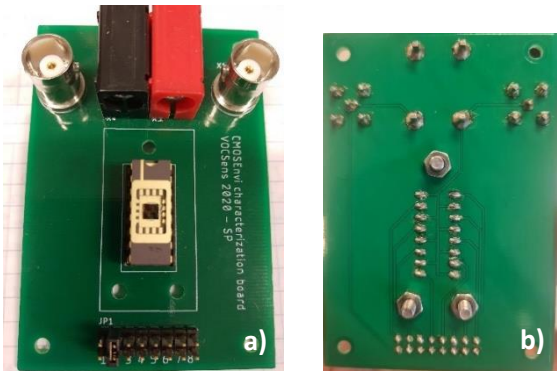

Figure 24. Board for gas sensing measurements a) bottom view b) top view with the die bonded to DIL-16 package in the centre

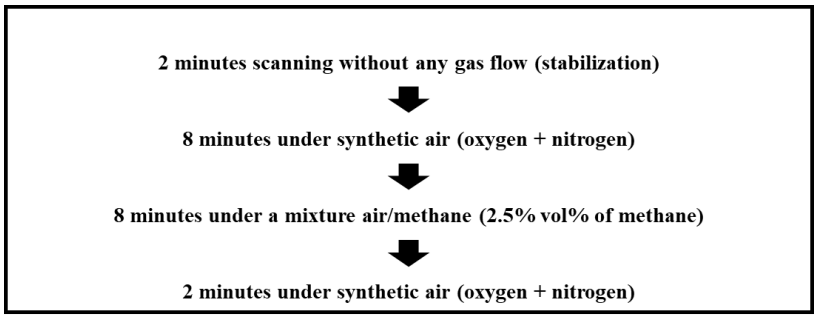

Figure 25. Protocol for preliminary gas sensing measurements

ii. Gas sensing

Gas sensing aims to test the four sensors sensitivity with different volumetric percentages concentration of methane. The set-up includes three standard gas cylinders – O_2, N_2/CH_4 (2%) and N_2 – mass flow controllers (MFC), a humidifier (Cellkraft, P-10), a sealed chamber and a data acquisition system. The output electrical resistance of the sensor is monitored by a DMM7510 7 ½ Digit Graphical Sampling Multimeter (Keithley). The set-up is illustrated in Figure 26.

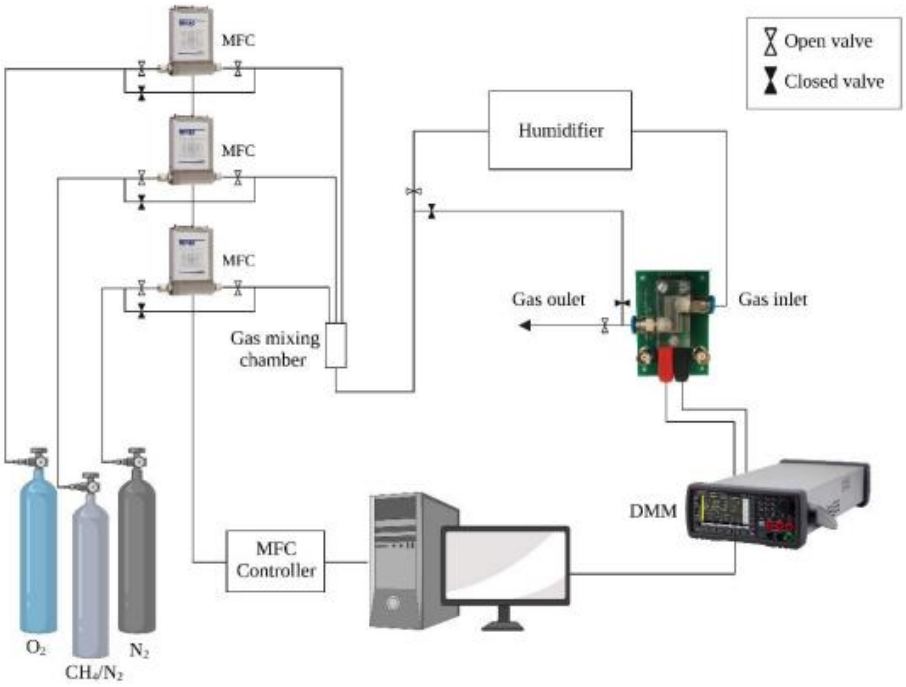

Figure 26. Schematic representation of laboratory gas sensor measurements set-up [100]

III. EXPERIMENTAL RESULTS AND DISCUSSION

In this chapter, results of the experiments conducted on reduced graphene and lead sulphide nanocrystals will be analysed and discussed. The first section will treat the graphene oxide reduction results. Through FTIR, Raman, TGA and deconvoluted XPS spectra reported in this section, the reduction rate is investigated. DFT calculations are evaluated to investigate the electronic properties of rGO. The second section is dedicated to the analysis of the lead sulphide nanocrystals synthesis results. XRD & XRF results are analysed to determine the crystallinity, size, and the purity of the nanocrystals, respectively which is then confirmed by ICP. SEM, TEM, and Optical Microscopy imaging investigates the morphology and dispersion of the nanoparticles. Data obtained from resistance measurements and gas sensing performances carried out on reduced graphene oxide and lead sulphide nanocrystals samples are finally described after description of the deposition techniques on IDEs.

3.1 Reduced graphene oxide production from GO

3.1.1 Reduction rate

Reduced graphene oxide samples were analysed through FTIR, Raman scattering and eventually by XPS. The thermal behaviour of rGO was investigated by thermogravimetric analysis. Details about the different synthesis conditions tested are summarized in Table 4.

3.1.1.1 Raman analyses

Raman spectra were acquired for each of the reduced graphene oxide samples considered in this work. Curve fitting for the Raman data was carried out in OriginPro 8.5 software with an appropriate Gaussian fit for each peak. The fits are in relatively good agreement with the experimental data, providing an adjusted R^2 greater than 0.9 for each peak. The spectra of each reduced graphene oxide sample showed two main peaks, defects peak (D) at 1360 cm^{-1} and graphitic peak (G) at 1580 cm^{-1} . The D peak, corresponds to the first allowed Raman mode A_{1g}, indicating the degree of defects present in graphene oxide flake by analysing the sp^3 hybridized carbon. On the other hand, the G peak stems from sp^2 graphitic carbons that form the crystal lattice and corresponds to the first order allowed Raman mode E_{2g}. Raman analysis is qualitative by nature, but by comparing the intensity ratio of the two primary peaks (I_D/I_G) from various samples, the reduction level can be investigated. Some samples I_D/I_G ratios are listed in Table 8 and their corresponding Raman spectra are shown in Figures 27-30. The rest of the Raman spectra are shown in Section Appendix. In general, the reduction of graphene oxide increases the corresponding I_D/I_G ratio as reported many times in the literature. [104]

[105] [106] This behaviour is shown in Table 8 where all samples display a higher ratio than commercial GO except for NMP 200. This one sample exhibits a lower ratio, and this trend is typically associated with a healing process that may have taken place after the reduction process due to the higher treatment temperature in this case. [107] The ratio for water-based reactions at 90°C with a full concentration of Vitamin C appears lower compared to those with half concentration. However, this difference could potentially be attributed to a margin of error in the analysis.

Table 8 - I_D/I_G ratios of multiple GO reductions tests

Sample (solvent, T°)	**I_D/I_G ratio**
Commercial GO	0.96
rGO NMP 200 without Vitamin C	1.34
rGO Water 80 (full Vitamin C)	1.28
rGO NMP 200 (full Vitamin C)	0.66
rGO Water 90 full Vitamin C	1.2
rGO Water 90 half Vitamin C	1.7

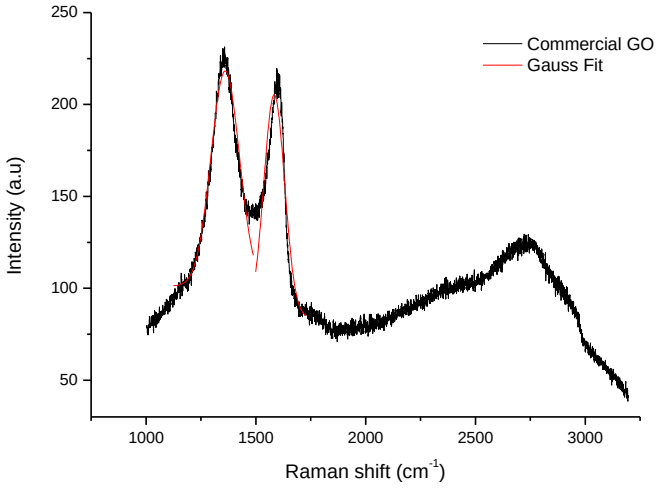

Figure 27. Raman spectrum of Commercial GO

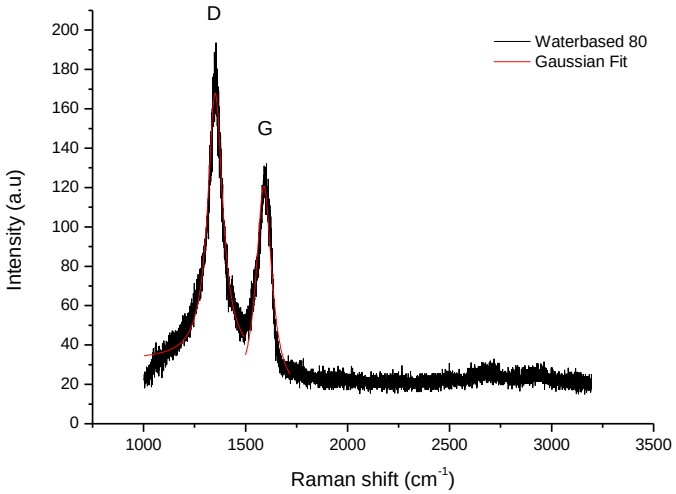

Figure 28. . Raman spectrum of water-based GO reduction at 80°C

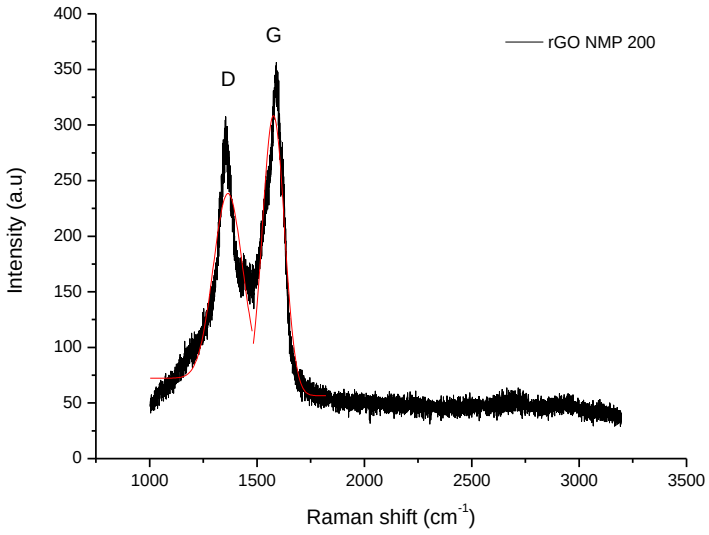

Figure 29. Raman spectrum of NMP based GO reduction at 200°C

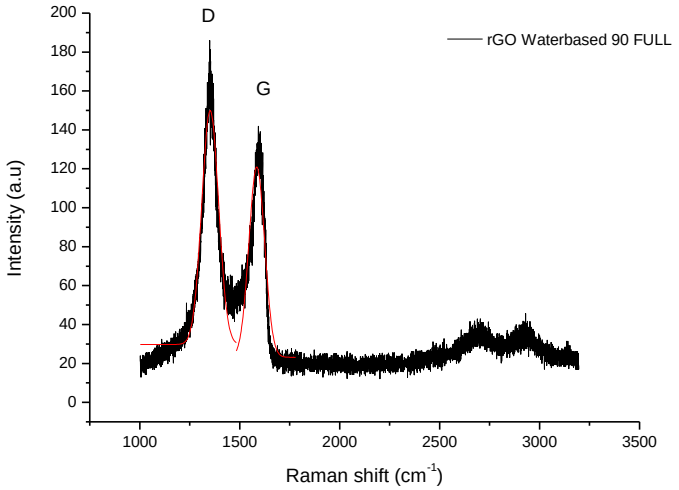

Figure 30. Raman spectrum of water-based GO reduction at 90°C with full Vitamin C (0.8M)

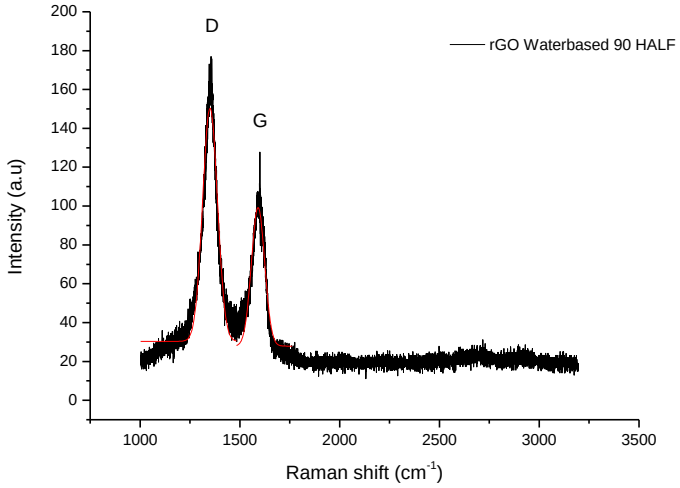

Figure 31. Raman spectrum of water-based GO reduction at 90°C with half Vitamin C (0.4M)

3.1.1.2 FTIR analysis

FTIR, another qualitative analysis method, was achieved for each rGO sample as well as for the commercial GO and showed multiple peaks. The graphene oxide (GO) of this work exhibits an intense absorption band at 3408 cm^{-1}, which is attributed to the stretching vibration of the –OH group from carboxyl and hydroxyl groups. The absorption peak around 1603 cm^{-1} corresponds to the bending vibration of the OH group. Additionally, a broad range of absorption peaks from 3000-3700 cm^{-1} appears due to the presence of oxygen-containing functional groups introduced during the oxidation process of graphene oxide. The C=O stretching vibration of the carbonyl group is observed at 1728 cm^{-1}, while the C-O stretching vibration of the carboxyl group is seen at 1380 cm^{-1}. Finally, the absorption peak at around 1045 cm^{-1} is attributed to the stretching vibration of C–O of the hydroxyl group. These peaks wavelengths can be compared with those reported by Yang et al. [108] The aromatic C=C is at 1600 cm^{-1} and the CO_2 is the tiny peak around 2300 cm^{-1}. The intensity of the stretching vibration of the –OH group varies significantly depending on the reduction rate of the rGO samples. It is important to note that since all baselines are created "manually" on the original data by using the Origin Pro program, a margin of error needs to be considered and a combination with the other analysis techniques present in this work, is essential. One can observe that GO commercial has the broadest -OH peak and this peak decreases in the wb 80 reduction sample, followed by wb 90 and finally NMP 200 which has the smallest peak (Figure 32). Overall, according to FTIR analysis, rGO NMP 200 is then the most reduced graphene oxide.

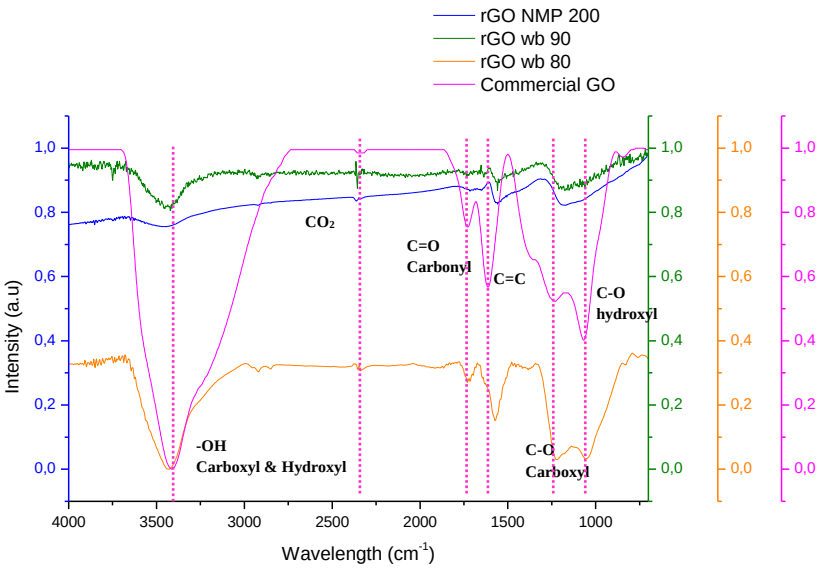

Figure 32. FTIR spectra of GO and different rGOs produced in this work

The impact of temperature on NMP-based reductions can also be observed, as indicated by the significantly lower peak compared to rGO NMP at 80°C in Figure 33. Additionally, the influence of Vitamin C is well pronounced in the case of NMP 200 compared to NMP 200 without Vitamin C, as seen in Figure 34. However, when comparing the half and full concentrations of Vitamin C, in the case of wb 90, the observed effect is relatively smaller, as depicted in Figure 35.

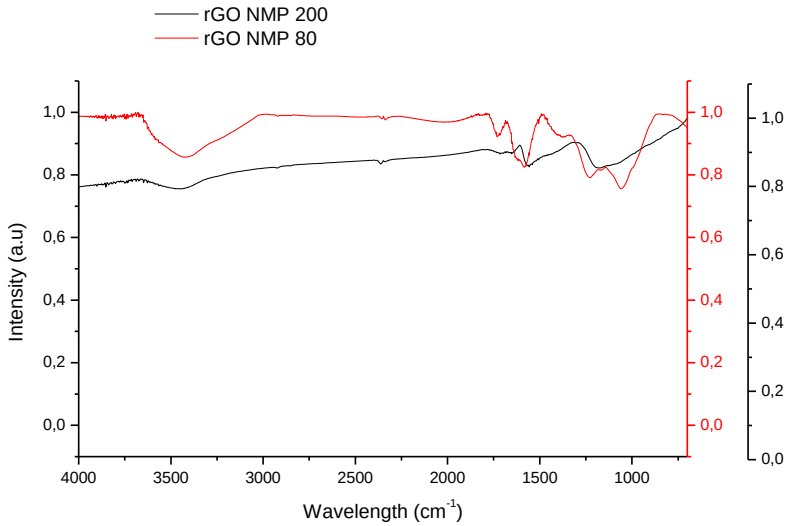

Figure 33. FTIR spectra NMP-based reductions of GO at 200°C and at 80°C

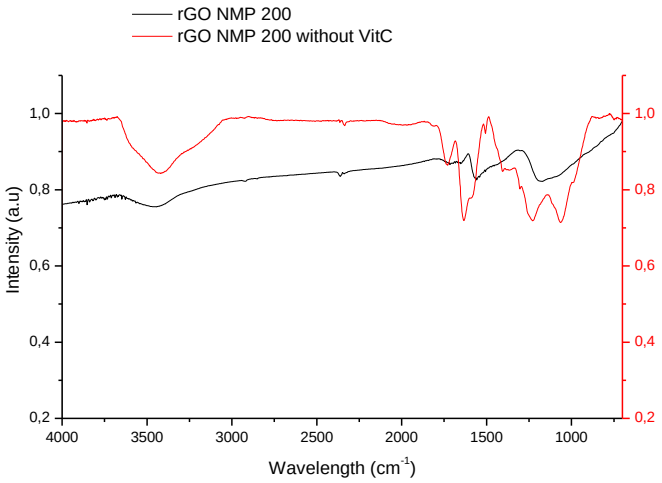

Figure 34. FTIR spectra of NMP-based reductions of GO with 0.8M Vit. C (black) and without Vit. C (red)

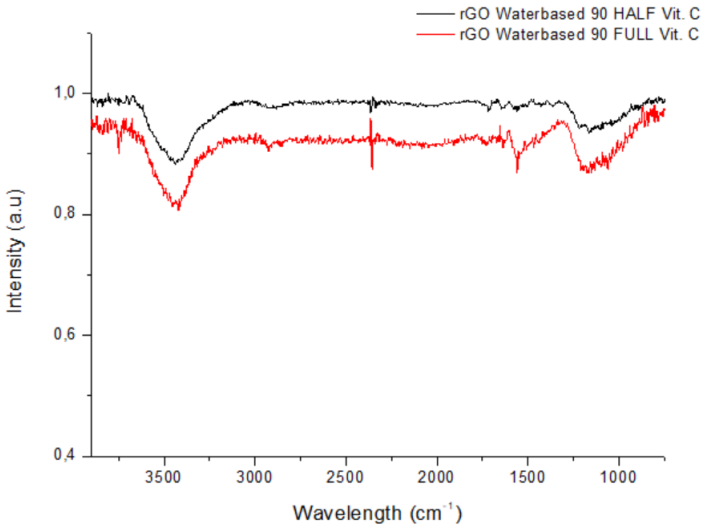

Figure 35. FTIR spectra of Waterbased rGO reductions at 90°C with full (red) and half (black) Vitamin C amounts

3.1.1.3 XPS analysis

XPS was employed to assess the reduction rate of some rGO samples. XPS is a semi-quantitative analysis technique that allows for the deconvolution of spectra (Figures 35-38), showing C 1s peaks with sub-components corresponding to C-O, O=CO, O-C-O, CCH sp^2, CCH sp^3 (Figure 36) as well as the O 1s peak, enabling the precise calculation of the O/C ratio as well as the sp^2/sp^3 ratios as shown in table 9. The O/C ratio should decrease as the reduction rate increases. However, the corresponding sp^2/sp^3 ratios are not directly proportional to O/C ratios since carbons from the basal plane can be damaged as explained in Section 3.1.1.1.

Table 9 - O/C ratios obtained by XPS for various rGO samples.

Sample	**O/C ratio**	**sp^2/sp^3 ratio**
Commercial GO	0.65	0.49
Water based 90°C full concentration of Vitamin C	0.20	0.5
Water based 90°C half concentration of Vitamin C	0.22	0.53
Water based 80°C	0.45	0.50
NMP 200 °C	0.28	0.54
NMP 80°C	0.40	0.50

GO has two main peaks in its C 1s spectrum (Figure 36) while rGO should exhibit a single peak which is also characteristic of graphite. Therefore, it would be confirming the good restoration of C=C bonds. [109] rGO NMP 200 exhibits indeed a C = C bonds dominating peak, as shown by one single peak with small tails at the higher-binding energy region (Figure 38) while rGO wb 80 (Figure 39) shows two peaks, which is a sign of its much lower reduction rate. The other XPS spectra are shown in Section 6.2.

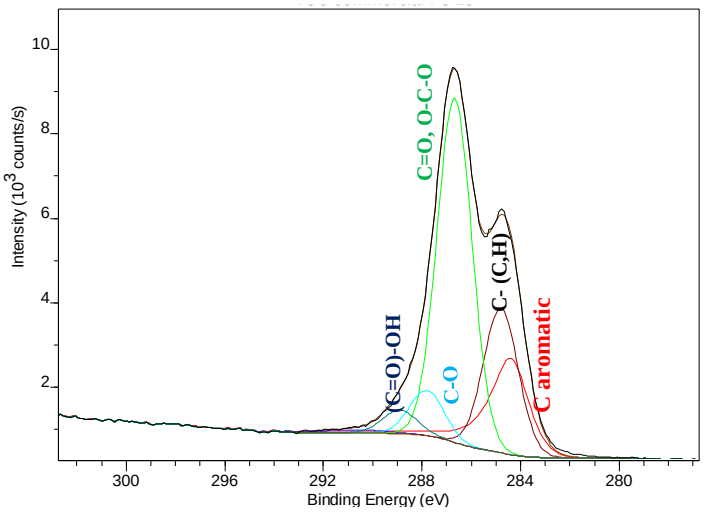

Figure 36. C 1s XPS deconvoluted spectrum of commercial GO.

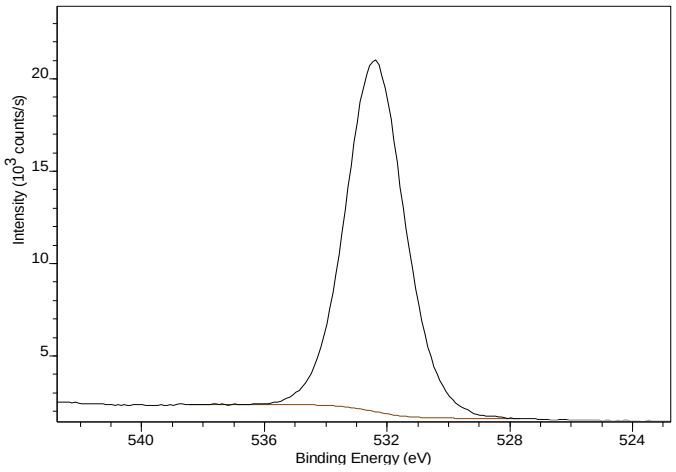

Figure 37. O 1s XPS spectrum of commercial GO.

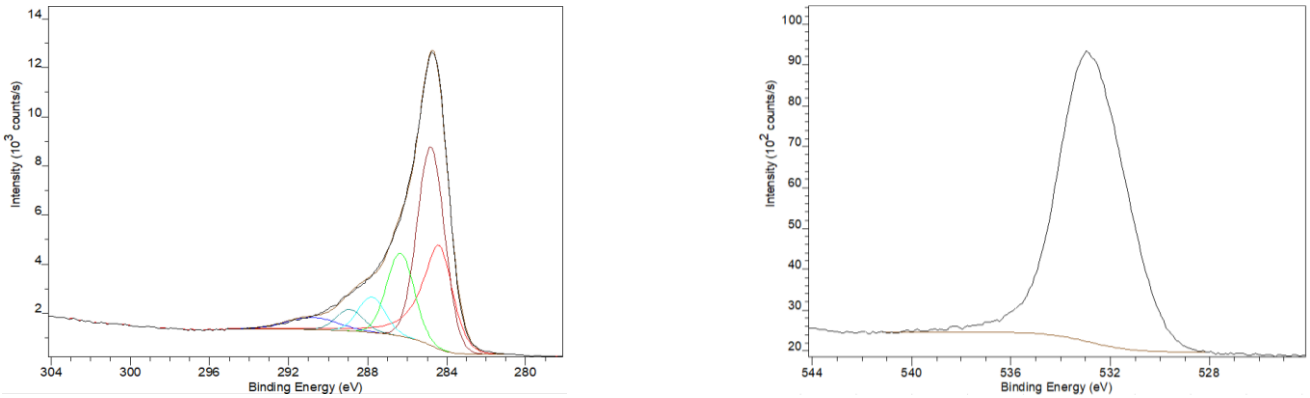

Figure 38. XPS deconvoluted spectra of rGO reduced with NMP at 200°C. C 1s (left) and O 1s (right).

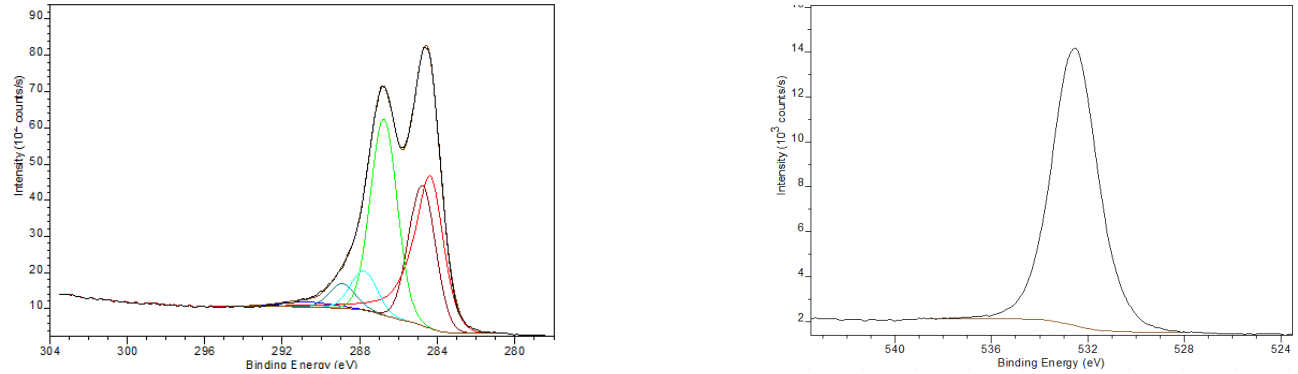

Figure 39.XPS deconvoluted spectra of rGO water-based reduced at 80°C. C 1s (left) and O 1s (right).

3.1.1.4 TGA analysis

TGA analysis was conducted under an air flux at 10°C/min, to examine the behaviour of moisture, oxygen groups, and carbon contents present in the graphene flakes. The analysis revealed various decomposition steps, including (1) the removal of moisture from interlayer adsorption of graphene oxide, followed by (2) the removal of oxygen-containing functional groups before concluding with (3) the decomposition of the carbon component itself as the analysis is conducted in air (Figure 40). As the oxygen-containing groups are removed, the second weight percentage step of the (r)GO samples decreases progressively.[107] Figure 40-a illustrates a reduction of 40% in weight for commercial GO and a reduction of 35% for NMP 80 as shown in Figure 40-b. Water-based reductions at 90°C and NMP 200°C exhibit a relatively comparable decrease, resulting in a loss of approximately 5% in weight as shown in Figure 40-c and 40-d respectively. These decreasing weight losses may be attributed to

hydroxyl and epoxy groups [110] and align with the decreasing O/C ratios analysed by XPS observed for the same samples, as shown in Table 9 above. After the first removal of oxygen containing groups, Figure 40 shows a slow and steady mass loss is observed and may be ascribed to desorption of more stable oxygen functional groups such as carbonyls. [53]

Afterwards, the decomposition of the carbon component occurs, and one can observe an increasing of the decomposition temperature for Commercial GO (~460°C) < NMP 80°C (~625°C) < wb 90°C half (~660°C) < wb 90°C full (~670°C). The increase observed is proportional to the O/C ratios analysed by XPS in these samples, indicating that the removal of oxygen-containing groups involves also some stabilization of the carbon content. Surprisingly, rGO NMP 200°C, which has similar O/C ratio than wb 90°C, and that exhibits the highest sp^2/sp^3 ratio (Table 9), has the lowest carbon decomposition temperature (~550°C) compared to the other rGOs. This could be due to a higher removal of oxygens, and bonded carbons, meaning that oxygen as well as carbon atoms are expelled during the heating. This carbon plane alteration could be caused by high temperature. [110] Therefore, there is a need for compromise when selecting the temperature of the reaction. Low temperature causes a partial removal of oxygen function groups with lower damages to the carbon basal plane and requires longer annealing times (not achieved in this work) to obtain sufficient reduction rate while high temperature allows the full deoxygenation of GO but altering the carbon plane. [110]

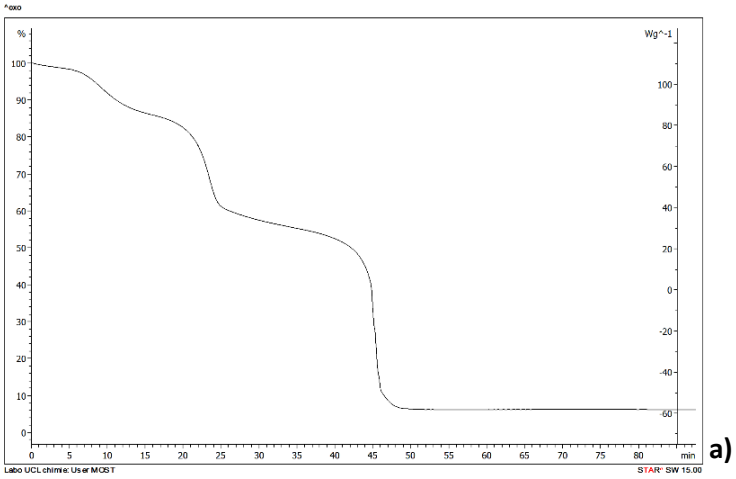

a)

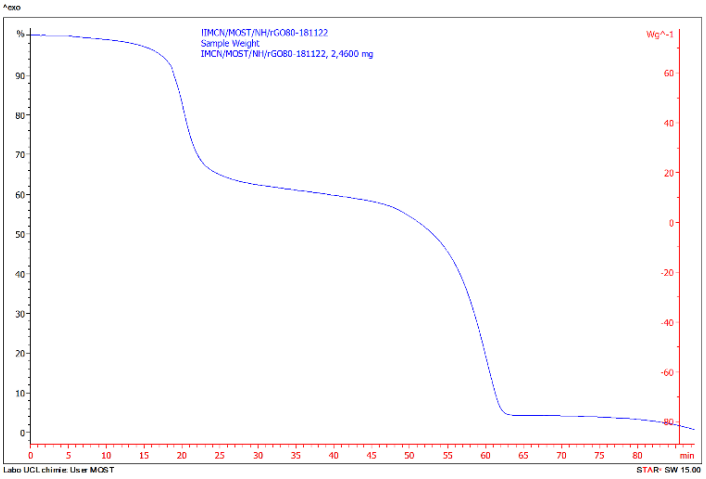

b)

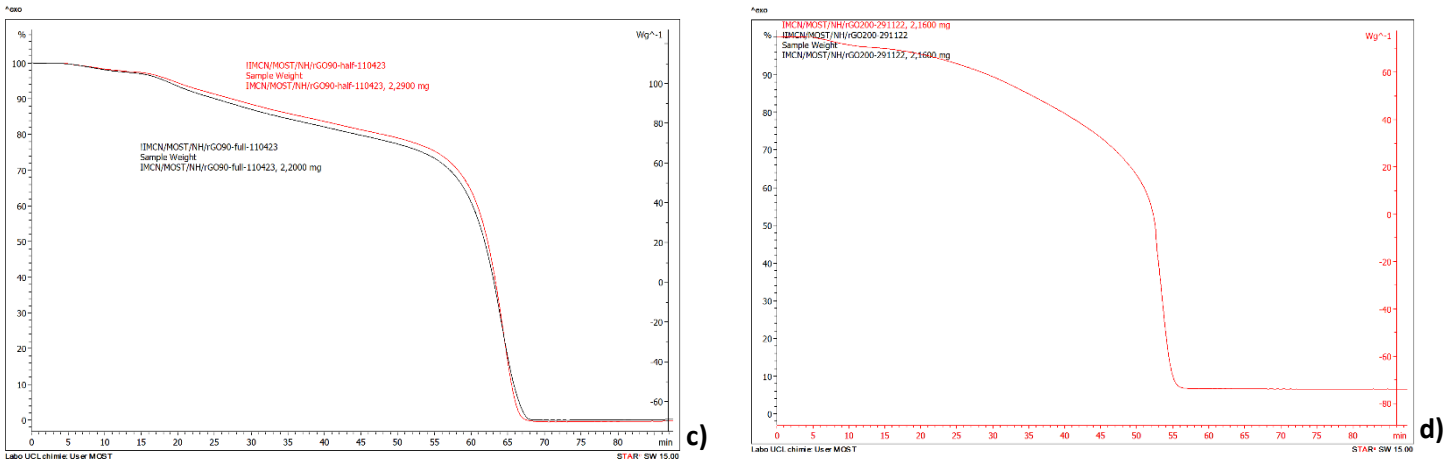

Figure 40. TGA profiles under oxygen flow at 10K/min, of commercial GO (a) NMP based GO reduction carried out at 80°C(b) Water-based GO reductions at 90°C half (red) and full (black) Vit. C (c) and NMP based GO reduction at 200°C (d)

Eventually, all these mentioned reduction syntheses give more reduced materials than commercial GO, meaning that both water and NMP have succeeded to reduce graphene oxide someway. The reduction synthesis tested with three different concentrations: 0.8M Vitamin C (full concentration), 0.4 M Vitamin C (half concentration), and without any Vitamin C revealed that the full concentration in Vitamin C improved the reduction rate and therefore was the best option. This difference is much more significative for reductions in NMP, when comparing with (full) Vitamin C and rGO NMP without any Vitamin C, than for Waterbased 90 with full and half concentration of Vit. C, as shown in Figure 35, where the full concentration yielded in a slightly smaller OH FTIR peak. Based on these results, it can be inferred that Vitamin C acts as a reducing agent in the reaction where its efficiency is just slightly better going from 0.4M to 0.8M.

When putting all data from different techniques together, NMP seems to be the best synthesis medium for rGO. The initial indication of the effect can be observed through the smallest OH peak in the FTIR analysis, followed by the prominent peak of C = C bonds in the XPS spectra. This leads to the highest ratio of sp^2/sp^3 carbons, which aligns with the decreasing I_D/I_G ratio compared to commercial GO, suggesting a sign of healing. However, the lower carbon decomposition temperature (T°) observed in the TGA analysis for NMP 200 indicates that this particular sample experienced potentially carbon loss, resulting in a higher concentration of C sp^2 and the disappearance of C sp^3.

3.1.2 Electronic properties

Electronic properties of reduced graphene oxide have been investigated to predict its behaviour in contact with methane gas. As reported many times in the literature [36], [104], rGO shows a p-type semiconducting behaviour and this characteristic appears to be beneficial for better tunability of the sensor. It is important to note that while the sensing of methane gas is reported to be carried out by lead sulphide nanoparticles, rGO is expected to function solely as a conductive layer and not as the sensing material, as reported in [21]. DFT calculations were performed on GO and the resulting band structures indicated a zero-bandgap for pristine graphene (Fig. 41), which is consistent with previous findings. [36] The bandgap remained zero even when the graphene crystal lattice was modified with epoxy groups (Fig. 41), although there was an increase in the Fermi level (see Table 10). In contrast, when pristine graphene was functionalized with hydroxyl groups, the bandgap became nonzero, and the Fermi level decreased significantly. Finally, when graphene was modified with both hydroxyl and epoxy groups, a non-zero bandgap was observed, and the Fermi level increased slightly compared to graphene with only hydroxyl groups. These findings indicate that GO functionalized with epoxy and hydroxyl groups, is a semiconductor material. The resulting non-zero bandgap is expected [3] and can range from > 0eV to values exceeding 2.5 eV. [111] Further analyses must be conducted to assess the semiconductor-type when GO is reduced in rGO.

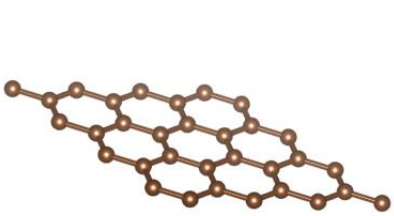

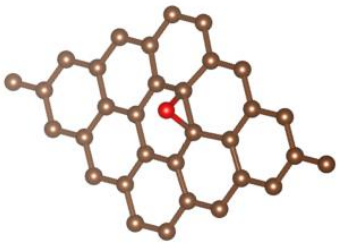

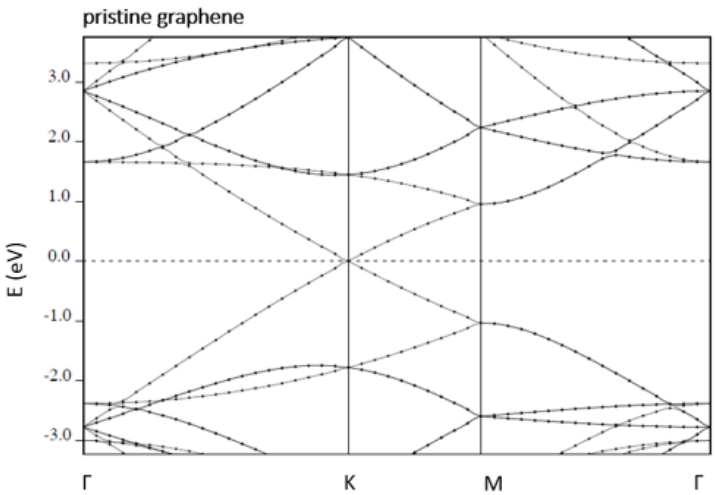

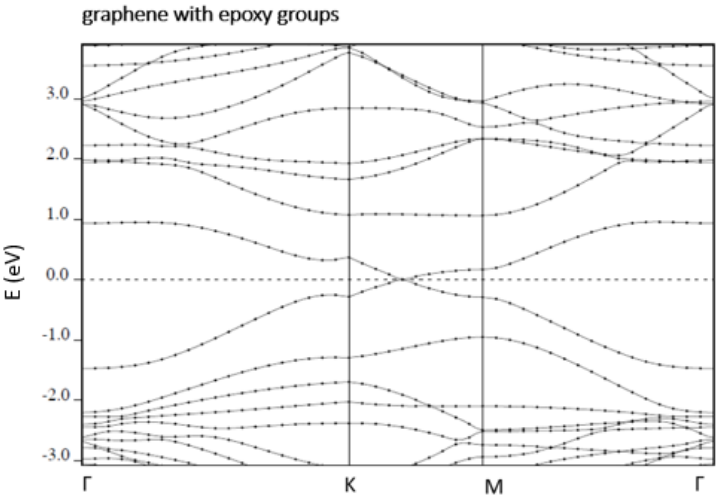

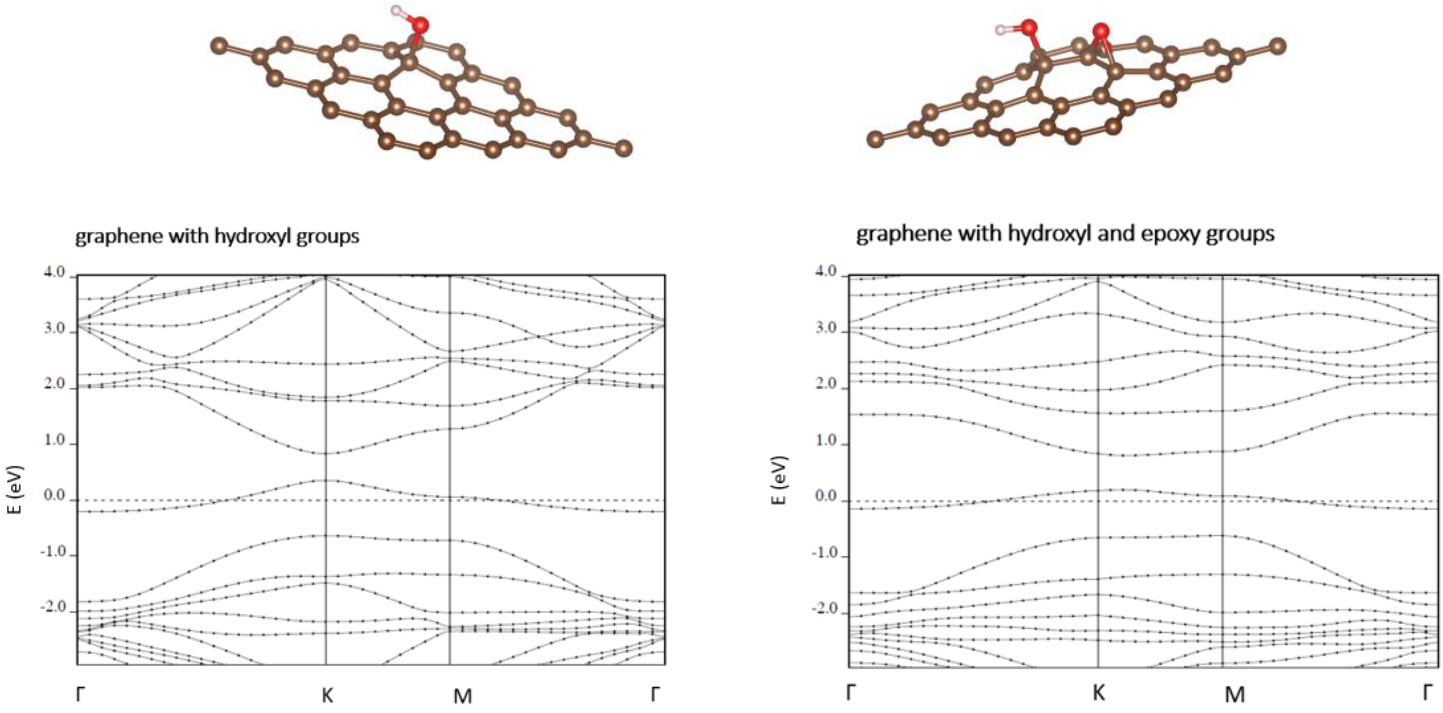

Figure 41. Chemical (up) and band structures (down) of various graphenes

Table 10 - Details about the band structures of pristine and functionalized graphenes calculated by DFT

	Fermi Level (eV)	**Bandgap (eV)**	**Total energy (Rydberg, where 1 Ry = 13.6 eV)**
Pristine graphene	-1.7578	0	-579.72
Graphene with epoxy groups	-1.9113	0	-620.68
Graphene with hydroxyl groups	-2.0417	0.5	-621.91
Graphene with hydroxyl and epoxy groups	-2.0244	0.5	-662.9

3.1.3 Deposition and morphology characterization

As mentioned in Section 3.1.1, the most reduced graphene oxide – corresponding to the synthesis with NMP as solvent at 200°C with Vitamin C - has been first dispersed in an ink solution and then deposited on the IDEs by manual drop casting method (methodology is explained in Section 2.6). The deposited rGO was observed by Optical Microscopy and by SEM imaging.

SEM images of the deposited material reveal a variety of shapes and sizes of dispersed rGO f flakes, including flat, folded, and sandstone-like slabs (refer to Figure 42). These flakes range in size from a few micrometres to tens of nanometres which is similar to the commercial GO (see Figure 43).

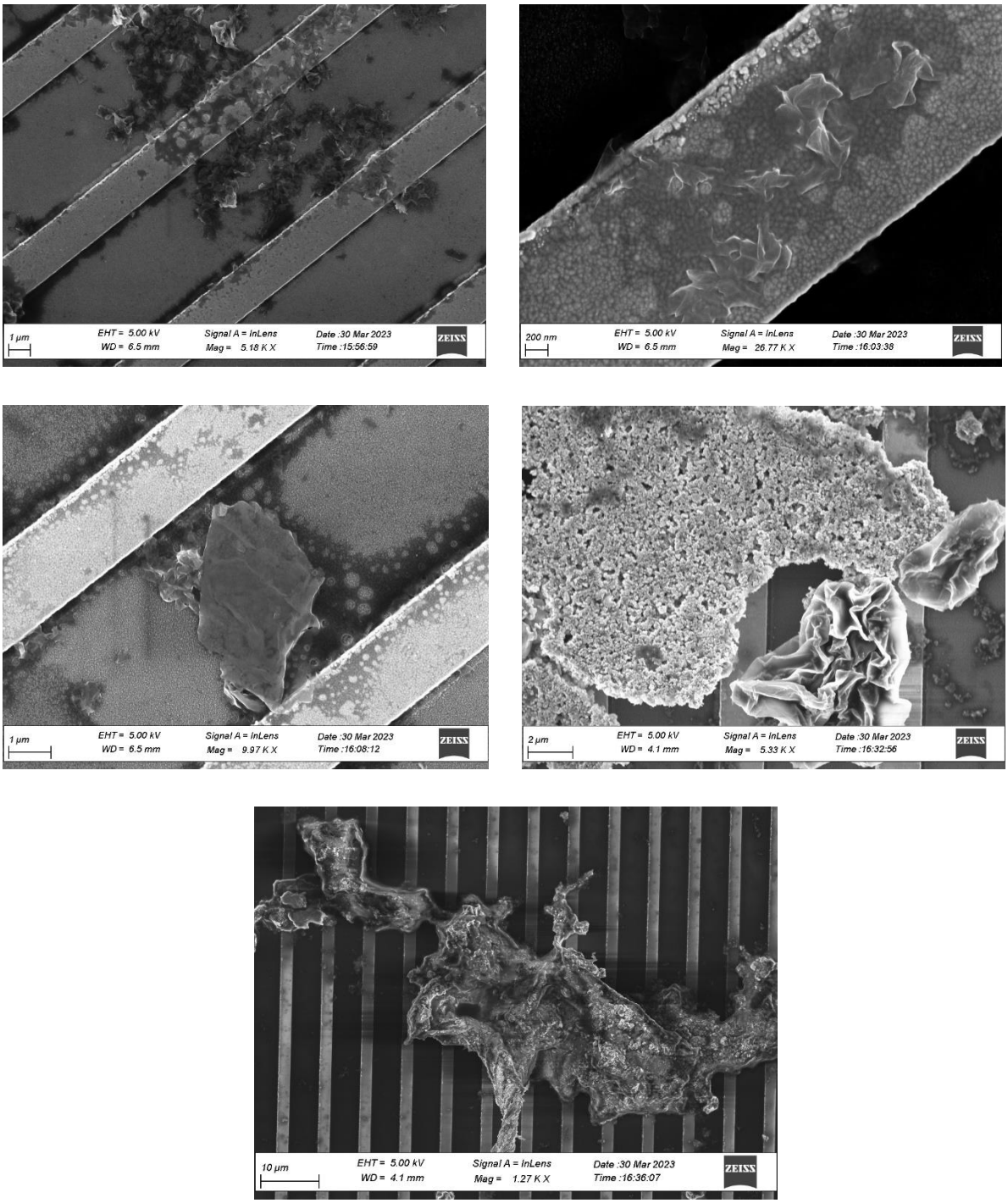

Figure 42. SEM images of rGO f flakes deposited on interdigitated electrodes

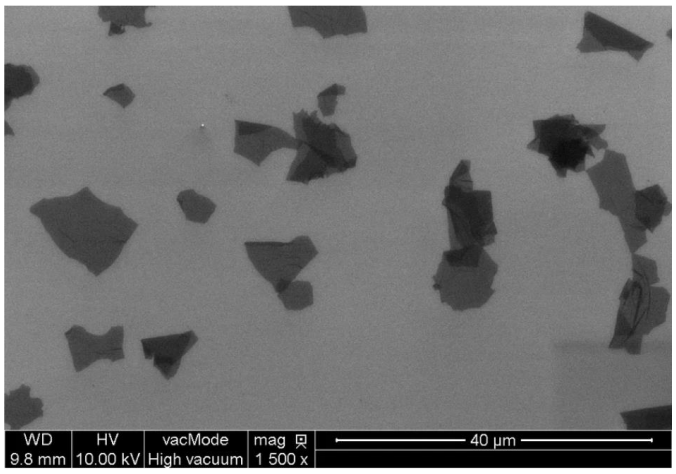

Figure 43. SEM image of 0.5 mg/mL water dispersion of Graphenea GO [112]

Optical images show dispersed black spots on the IDEs. Interestingly, the small electrodes exhibit a phenomenon known as the "coffee ring effect" where flakes naturally concentrate more towards the periphery of the electrode rather than the centre (Figure 44). This effect could be attributed to three factors: the small size of the electrodes (Table 5), the viscosity of the ink solution, and the manual nature of the drop casting process. Indeed, in this case, all the drops were deposited at the same central location, while for larger electrodes, several drops were added at different positions. Therefore, it can be concluded that rGO flakes can be deposited by this technique, but further work would be necessary to obtain optimal layers.

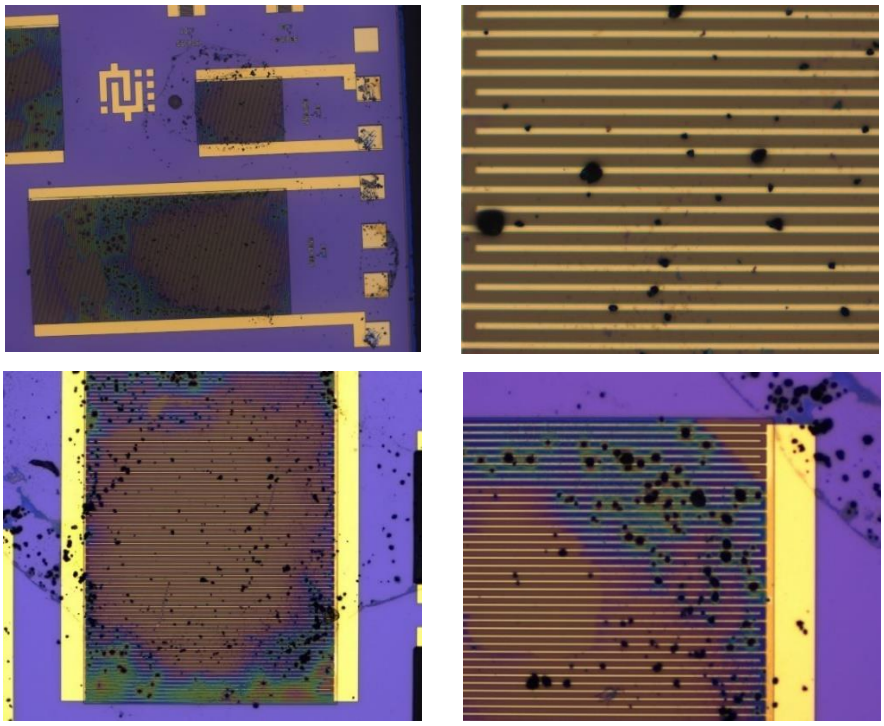

Figure 44. Optical microscopy images of rGO f deposited interdigitated electrodes

3.2 Synthesis of Nanoparticles of PbS and Characterisation

3.2.1 PbS synthesis

Lead sulphide nanoparticles were synthesized using various protocols as explained and illustrated in Section 2.3. The various PbS samples are listed in Table 5 and the four selected ones are highlighted in grey. Their crystallinity and S:Pb molar ratios were initially evaluated using XRD and, XRF and ICP analyses, respectively. In some instances, ICP analysis was conducted on the samples. SEM and TEM were employed for visual morphological analysis of the particles that were roughly deposited on dies.

Table 11 - Details about the PbS nanoparticles syntheses – Protocol 1

Sample	**Na_2S dripping time**	**Capping agent (2-mercaptoethanol)**
PbS 2	8h	Yes
PbS 3	4h	Yes
PbS 4	1h	Yes
PbS 5	2h	Yes
PbS 6	2h	No
PbS 9	3h20	Yes
PbS 10	1h	No
PbS 11	50 min	Yes
PbS 12	1h	Yes
PbS 13	40 min	Yes
PbS 14	30 min	Yes

All PbS samples showed fortunately peaks in agreement with peaks corresponding to PbS crystalline phases (Figure 46). Lead sulphide's XRD pattern displays nine characteristic diffraction peaks corresponding to crystal planes (111), (200), (220), (311), (222), (400), (331), (420) and (422) that are located at 26.03 degrees, 30.15 degrees, 43.16 degrees, 51.10 degrees, 53.55 degrees, 62.68 degrees, 69.06 degrees, 71.12 degrees and 79.14 degrees, respectively. Standard XRD pattern is shown in Figure 45 as reported in [113].

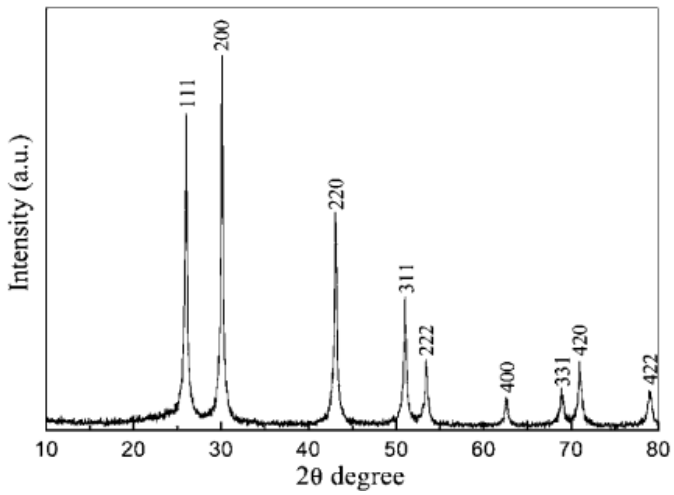

Figure 45. Standard XRD pattern of PbS nanocrystals [113]

Their dispersity, morphology, and shapes of the obtained PbS nanoparticles were collected imaged with SEM and TEM microscopy.

First, one can notice the similarity of the peak's broadness for the samples prepared by the 1st protocol, for PbS 3, 4 and 6. For example, XRD pattern PbS 10 (1h dripping time), PbS 14 (30 min) then PbS 2 (8h) which appears to correspond to a more crystalline sample than the others. Other XRD patterns are shown in Section 6.4.

The XRD patterns obtained in the 1st protocol case reveal a higher background intensity, which arises due to the presence of an amorphous phase. The asymmetry in the background shape may be attributed to stacking faults, which are planar defects occurring in crystalline materials. Specifically, errors can occur in the arrangement of these layers. [102] In the case of PbS 4 and PbS 6, the observed increase in background intensity is particularly notable at low angles. This can be attributed to two main factors. Firstly, it suggests that the sample surface is not adequately flat, resulting in the laser beam encountering the amorphous sample holders. Secondly, the presence of an amorphous phase within the powder indicates the probable presence of uncrystallized lead and sulphide compounds.

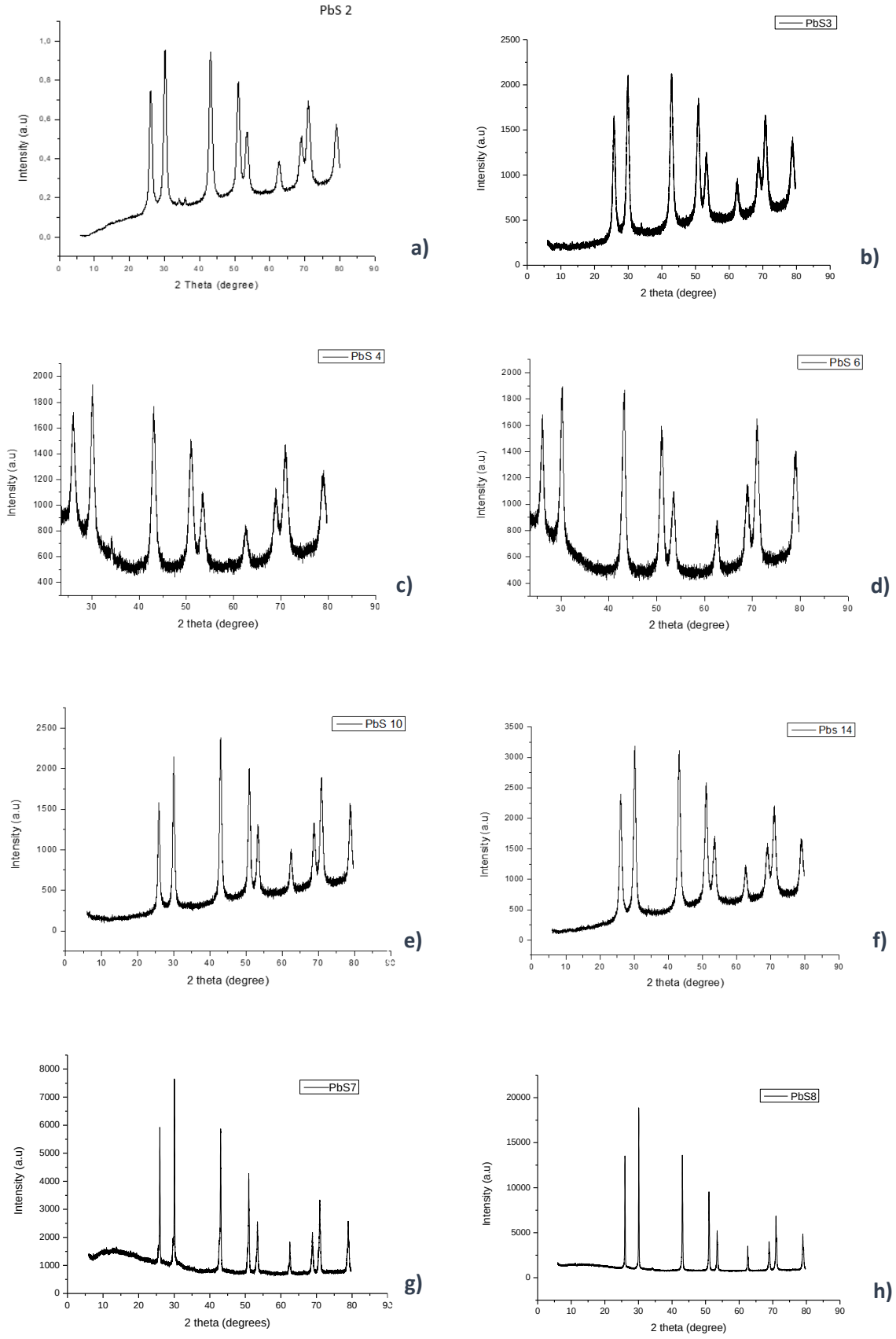

Figure 46. XRD patterns of different PbS synthetized nanoparticles. a-f) 1st protocol, g- h) 2nd protocol

The Debye-Scherrer formula, as mentioned in Section 4.7, was used to calculate the crystallite sizes and the results are shown in Tables 12 & 13. One can observe a narrow distribution of sizes for the synthesis of the nanoparticles using the first protocol. It appears that the dripping time didn't have that much impact on the size of the obtained particles. It should be noted that the value obtained by the Debye-Scherrer equation is typically considered to be a lower bound estimate for the size of nanoparticles. Indeed, XRD pattern can suffer from broader peaks due to various other factors that particle sizes, such as defects, stress, dislocations, twins or stacking and inhomogeneous strain in the crystal lattice[102]. Moreover, the Scherrer approach assumes a homogeneous size distribution of monocrystalline domains. This can result in inaccurate results for crystallite sizes if a broad distribution of crystallites ranging from small to large sizes is present within a sample.[102] These facts could explain the sizes observed in SEM images that show larger spherical particles, even though it is quite hard to have a sufficient resolution to distinguish single particles. When the size is systematically observed as larger by microscopy compared to XRD, it definitely means that the particles are poly crystalline. Also, particles tend to aggregate, as confirmed by TEM images (Figure 49). In agreement with the microscopy images also, the second protocol gives much larger nanoparticles (Table 13).

Table 12 – PbS crystallite sizes using Scherrer equation – 1st protocol

	Crystallite size (nm)	
Sodium sulphide dripping time	**With capping agent**	**Without capping agent**
30 min	8.61	/
40 min	7.56	/
50 min	8.46	/
1h	8.31	10.83
2h	7.3	9.85
3h20	7.9	/
4h	9.81	/
8h	8.25	/

Table 13 – PbS crystallite sizes calculated Scherrer equation – 2nd protocol

$PbCl_2$:S:$NaBH_4$	**Crystallite size (nm)**
1:1:1	35.98
1:1:3	41.78

When characterizing the morphology by electron microscopy, particles synthetized with the protocol n°1 appear to be spherical and with different sizes - the most distinguishable ones

range from 10nm to 20nm in diameter (see Figure 47). By contrast, particles from the second protocol show big cubes - the most distinguishable one measures 40nm - as shown in Figure 48. Other cubes fall within the micrometre range. The disparity in size between the samples obtained using the first and second protocols is evident in the XRD analysis, as depicted in Figure 46. XRD patterns of the 2nd protocol (Fig. 46 g-h) displays extremely sharp peaks and a high degree of crystallinity, indicating a well-defined crystal structure. Conversely, XRD patterns from the 1st protocol (Fig. 46-a-f) demonstrates much broader peaks and lower crystallinity, signifying a smaller particle size or a less organized crystal lattice.

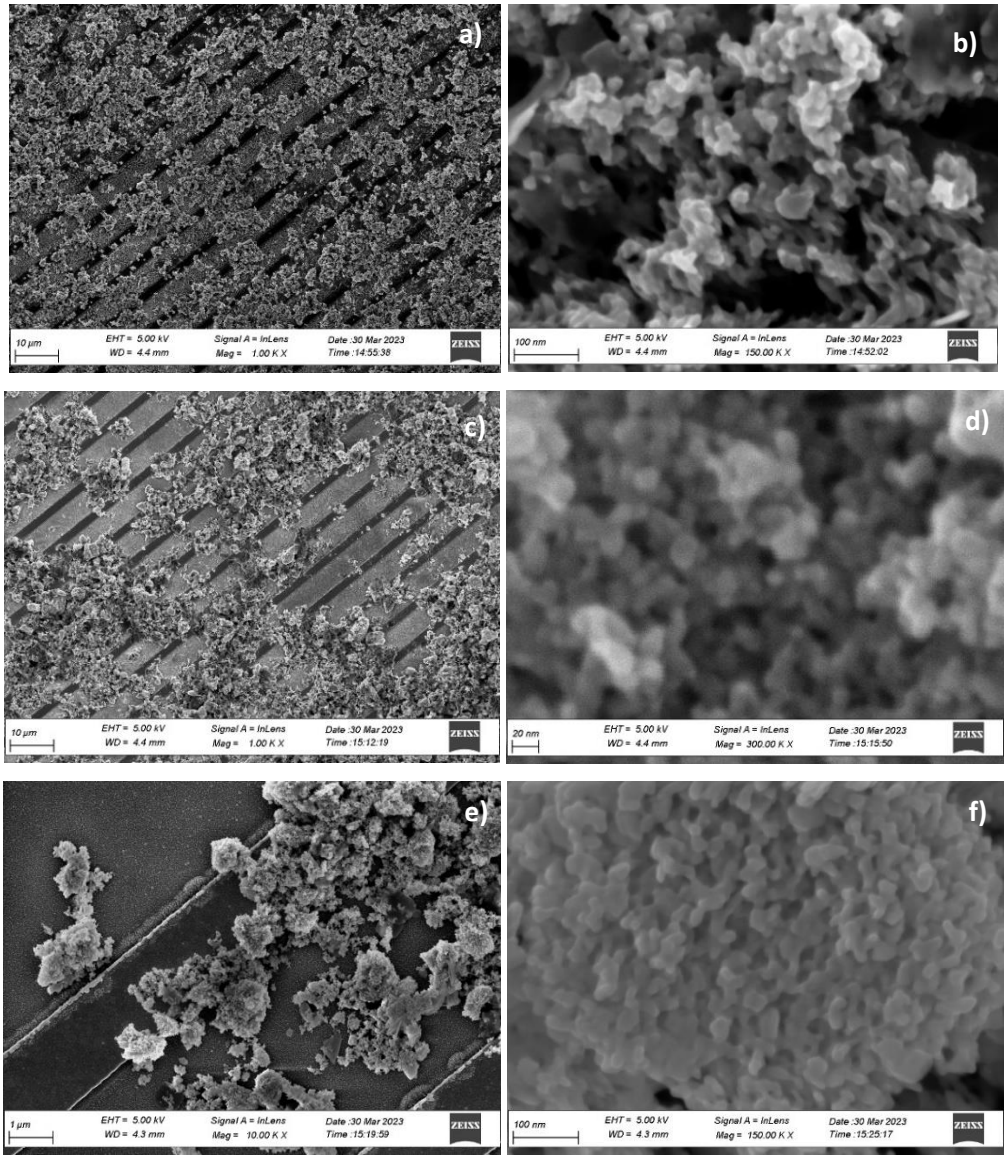

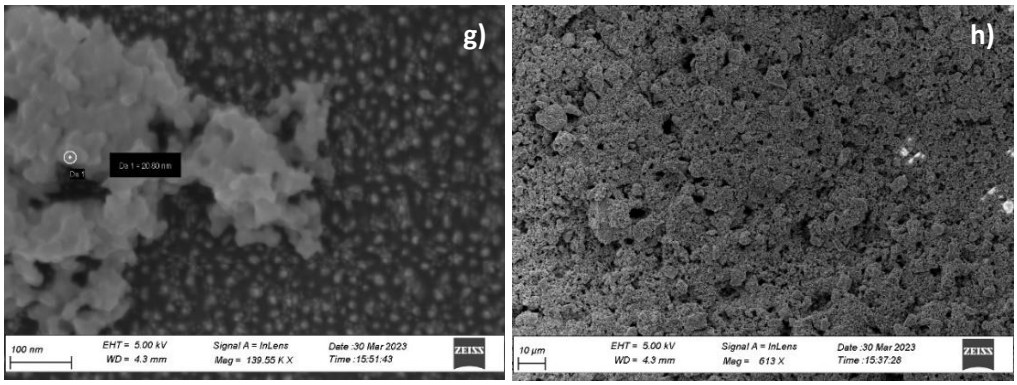

Figure 47. SEM images of dispersed PbS NPs PbS 4 a-b) PbS 6 c-d) PbS 10 e-f) and PbS 14 g-h)

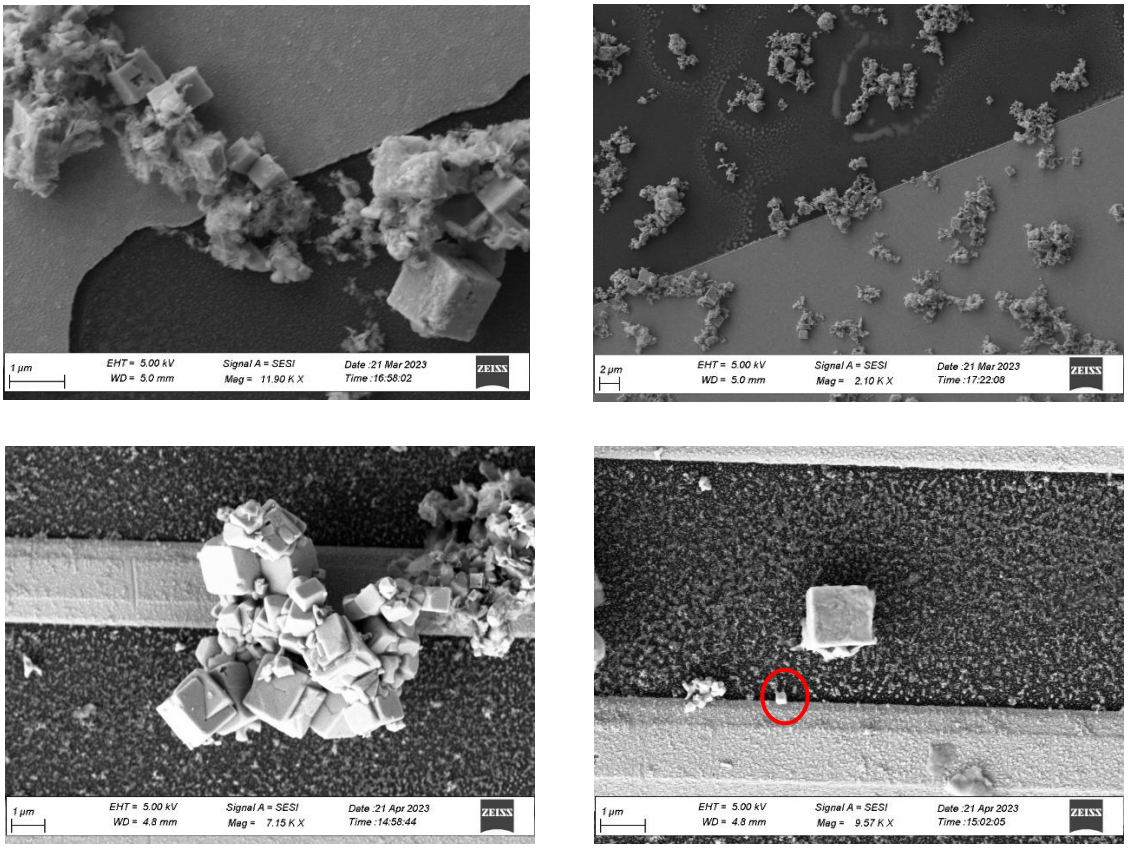

Figure 48. SEM images of PbS 7 (top) and PbS 8 (bottom), prepared using the second protocol. The smallest cube is encircled in red.

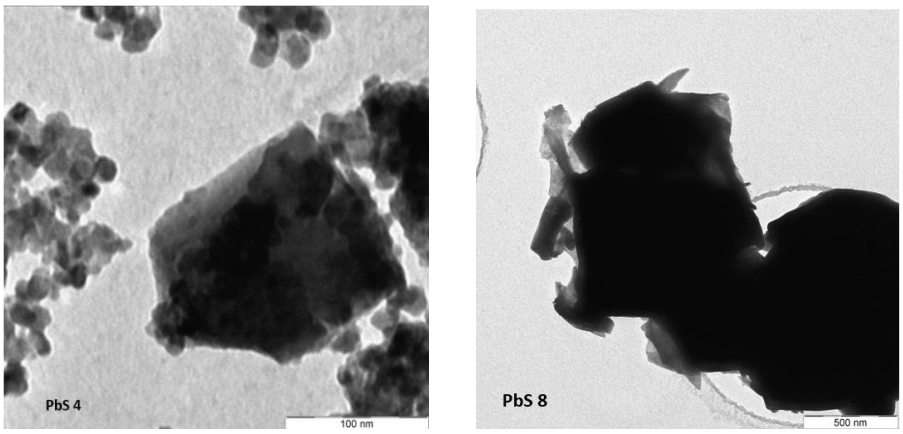

Figure 49. TEM images of PbS 4 and PbS 8 samples prepared by the second protocol

The temperature involved in the 1st (RT) and 2nd syntheses (40°C) syntheses might have had a role on the obtained PbS NCs shapes. The intrinsic surface energy of {111} facet of PbS is higher than that of its {200} facet. [114] It is reported that at higher reaction temperatures the growth of atoms on the {111} facets are favoured. [115] This kinetically controlled formation of cubic nanocrystals [116] and nanostructures [117] makes the nanocrystals expose {100} facets more likely [115]. Additionally, the 2nd protocol may be considered as following a hot injection approach, in the case of diffusion-controlled reactions, as explained in Section 1.3. The immediate nucleation that occurs after injection leads to a rapid increase in the average size of the particles.

The theoretical weight percentages of Pb:S is 86.6% of lead and 13.4 % of sulphur in a perfectly pure PbS material. The synthesized samples were analysed by XRF and ICP to determine their Pb and S weight percentages and the different S:Pb molar ratios that can be calculated from these experimental values. The goal obviously is to have a S:Pb molar ratio as close to 1 as possible. The obtained weight percentages of lead and sulphur are close to their theoretical values, meaning that the nanoparticles have a quite high purity. However, all PbS samples, according to XRF analysis, exhibited an excess of sulphur, because they display S:Pb molar ratios ranging from 1.1 to 1.3. It should be noted that XRF suffer from matrix and interelement interference issues. With XRF, the standard and sample must be matrix matched with respect to both the matrix and the particle size. We have tried to use a reference sample that matches closely our synthesized samples, but the particle size was not identical. On the other hand, ICP-OES can give very accurate and precise results. In addition, ICP is carried out after sample dissolution so it can be considered as a bulk analysis, while XRF has a certain penetration depth but will be influenced more by surface effects. The excess of sulphur seen by XRF might be

located at the surface of the particles. Therefore, ICP results will be considered more decisively for the following discussion and conclusion of this work.

It can be noticed that the absence of capping agent during the synthesis did not change the molar ratios obtained that much, as can be seen for the molar ratio obtained for sample PbS 6 (see Table 14) which was obtained with 2h dripping time of sodium sulphide PbS without 2-mercaptoethanol, as compared to the others.

In the case of the second protocol (Table 15), one sample showed a much lower S:Pb ratio, 0.52. In that case, the lower S:Pb ratio in that sample, 0.83, was also visible by ICP. This could be explained by a lower amount (1:1:1 $PbCl_2$:S:$NaBH_4$) of the reducing agent, sodium borohydride, compared to PbS 8 (1:1:3 $PbCl_2$:S:$NaBH_4$). Sulphur compound reacts with protons released by the borohydride and the produced hydrogen sulphide then reacts with lead to produce the lead sulphide, as shown in the following equation [118] :

$$PbCl_2 = Pb^{2+} + 2Cl^-$$

$$2NaBH_4 + 2Cl^- = 2NaCl + B_2H_6 + 2H^+ + 2e^-$$

$$2H^+ + S^{2-} = H_2S$$

$$H_2S + Pb^{2+} + 2e^- = PbS + H_2$$

Table 14 - S:Pb weight percentages and molar ratios in PbS samples synthetized by the 1st protocol.

Sample	Sodium sulphide Dripping time	XRF wt.%Pb wt.%S	XRF S:Pb molar ratio	ICP wt.%Pb wt.%S	ICP S:Pb molar ratio
PbS 2	8h	84.96 14.76	1.12		
PbS 3	4h	84.38 15.41	1.18		
PbS 4	1	86.23 13.58	1.02	81.22 12.45	0.99
PbS 5	2	82.78 16.97	1.32	82.03 12.70	1
PbS 6	2	82.44 17.34	1.36	81.96 12.36	0.98
PbS 9	3h20	83.27 16.55	1.28		
PbS 10	1	83.85 15.99	1.23	81.21 12.10	0.96
PbS 11	50 min	83.88	1.23		

		15.93			
PbS 12	1h	83.76 16.09	1.24		
PbS 13	40 min	83.41 16.33	1.26		
PbS 14	30 min	82.77 16.98	1.32	80.91 12.56	1

Table 15 – weight percentages and molar ratios in PbS samples synthetized by the 2nd protocol.

Sample	**Duration**	**XRF Wt.% Pb Wt.% S**	**XRF S:Pb molar ratio**	**ICP Wt.%Pb Wt.%S**	**ICP S:Pb molar ratio**
PbS 7	4h	92.06 7.35	0.52	82.77 10.60	0.83
PbS 8	4h	84.71 15.07	1.15	84.12 12.53	0.96

3.2.2 Electronic properties

DR UV visible analyses were carried out on PbS samples to calculate the bandgap but unfortunately, it appears that all PbS samples absorb too strongly, and absorption saturation appears around 240 nm, which is the wavelength at which the first peak should appear(See Section 6.5). This method proved unsuccessful to determine the bandgap of our synthesized samples, unfortunately.

3.2.3 Thermal behaviour

Thermogravimetric analysis was performed on a PbS sample, and it appears that the material is losing mass until 200°C, probably due to solvents and/or organic impurities losses. After reaching that temperature, one can notice a 14% weight gain between 200°C and 450°C and eventually, a steady behaviour until 800°C. This weight increase is probably linked to lead sulphide oxidation since TGA is performed under ambient air. The very small amount of powder that was remaining in the crucible at the end of TGA analysis was hardly recoverable but still taken to be tested with XRD analysis. Unfortunately, XRD results (see appendix) give un-processable data, probably due to the too small amount. However, an oxidation of PbS

leading to the oxidized forms $PbSO_3$ and $PbSO_4$ is suspected according to the XPS analysis reported in [119].

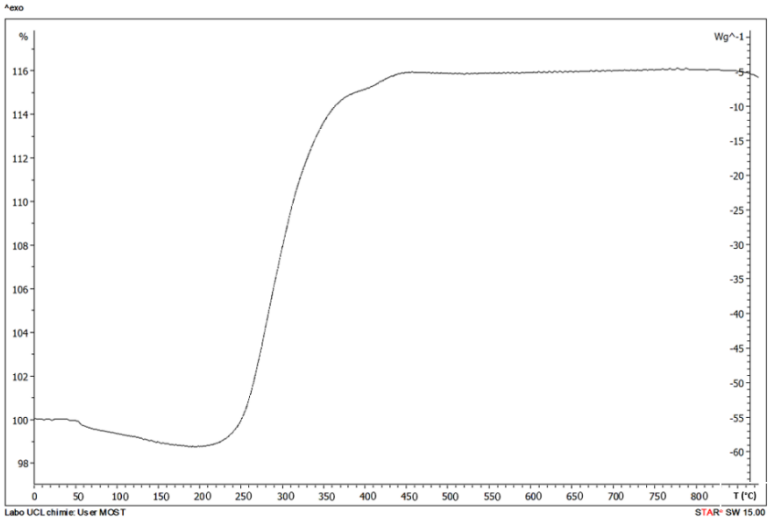

Figure 50. TGA thermogram of PbS 4

3.2.4 Deposition and morphology of PbS dies

This section discusses the deposition of PbS following the deposition procedure and the dropcasting station illustrated in Section 2.6.

Due to the relatively similar characteristics in terms of crystallinity, crystallite size, and particle shapes observed in all the samples, distinguishing between them becomes challenging. Moreover, the analysis conducted using ICP and XRF techniques revealed distinct S:Pb ratios for each sample. To showcase various possible scenarios, the samples PbS 4 (1h) , 6 (2h *without* capping agent), 10 (1h *without* capping agent), and 14 (30 min, the shortest time dripping) were specifically selected for further investigation. The four samples are first dispersed in Milli-Q water and then deposited (as described in Section 2.4 & 2.6, respectively) on the IDEs by manual dropcasting method.

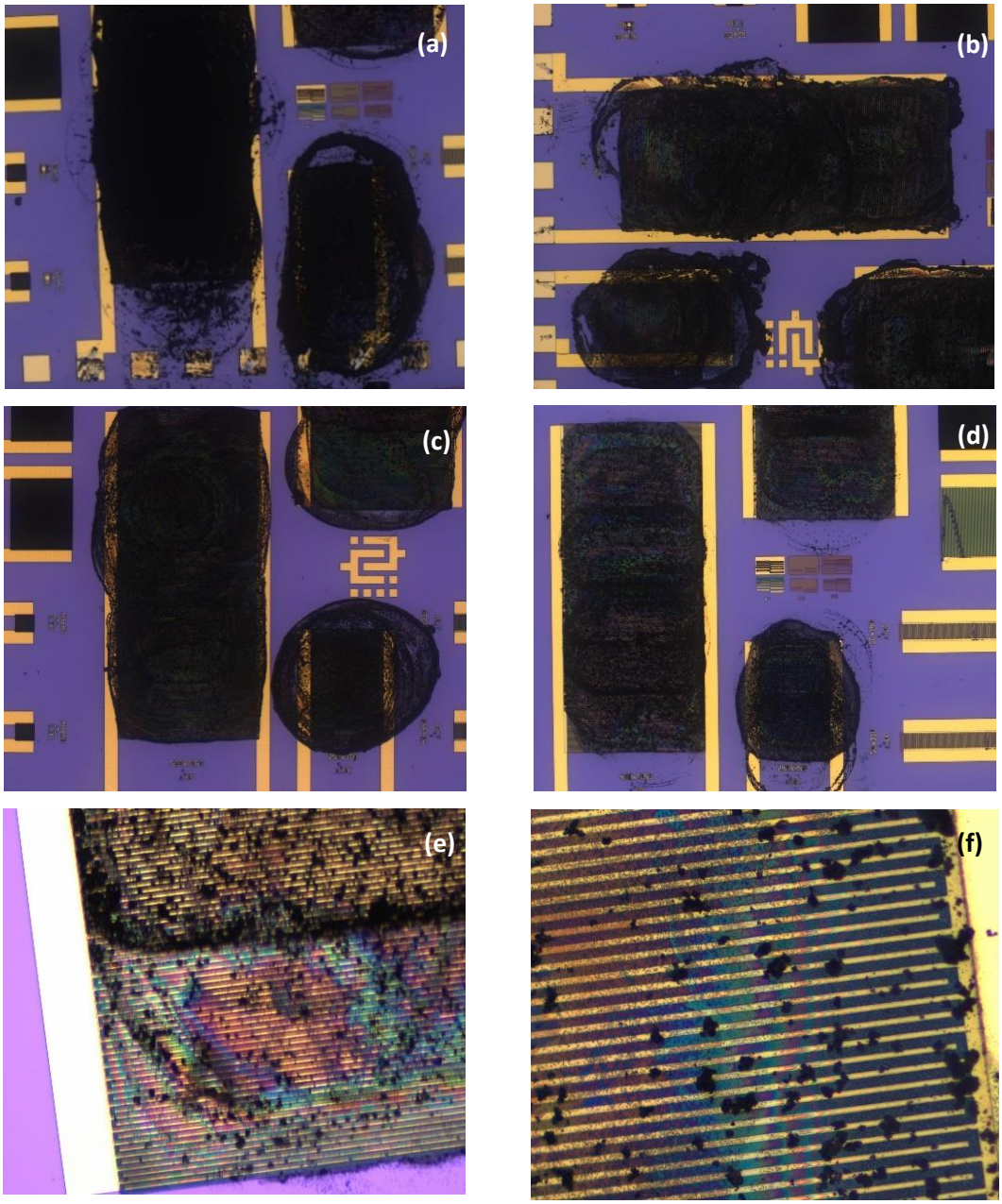

Figure 51. Optical Microscopy images of PbS NPs deposited on IDEs: PbS 4 (a) PbS 6 (b) PbS 10 (c) PbS 14(d) with 10X magnification. PbS 14b with 20X (e), PbS 14b with 50X (f)

The deposition of 180 drops on large electrodes and 160 drops on small electrodes resulted in a black, dark coating. Compared to the three other samples deposited, PbS4 exhibited the darkest appearance, possibly because it was the first die to be prepared and the drop size might

have been larger due to better control over the manual drop casting method over time. One can clearly see the particles being well dispersed on the IDEs in Figure 51 e-f.

3.2.5 Deposition and morphology in the case of mix: PbS on top of rGO

When PbS nanoparticles are deposited on top of rGO flakes, Optical Microscopy images show coatings (Figure 52) that appear darker compared to rGO flakes alone (Figure 44). SEM images show dispersed PbS nanoparticles on top and beside rGO flakes (see Figure 53).

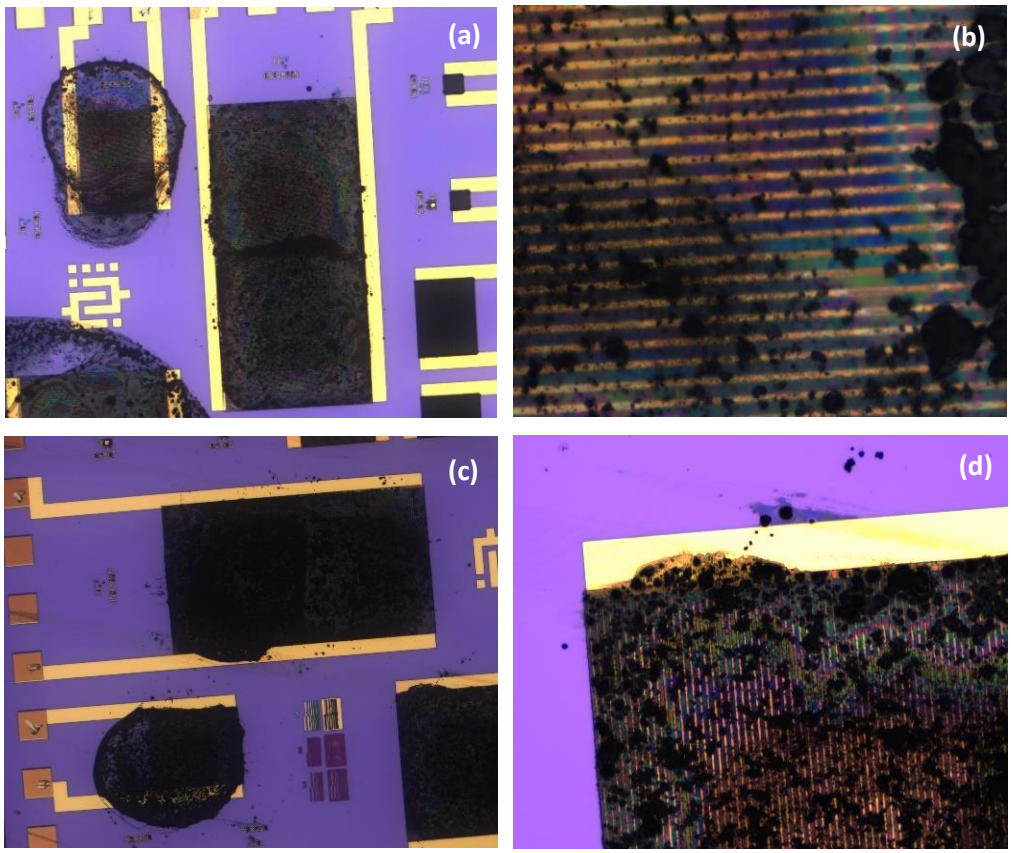

Figure 52. Optical Microscopy images of deposited rGO + PbS on IDEs. rGO 3/ PbS 4 a- b) rGO 4/ PbS 14 c-d)

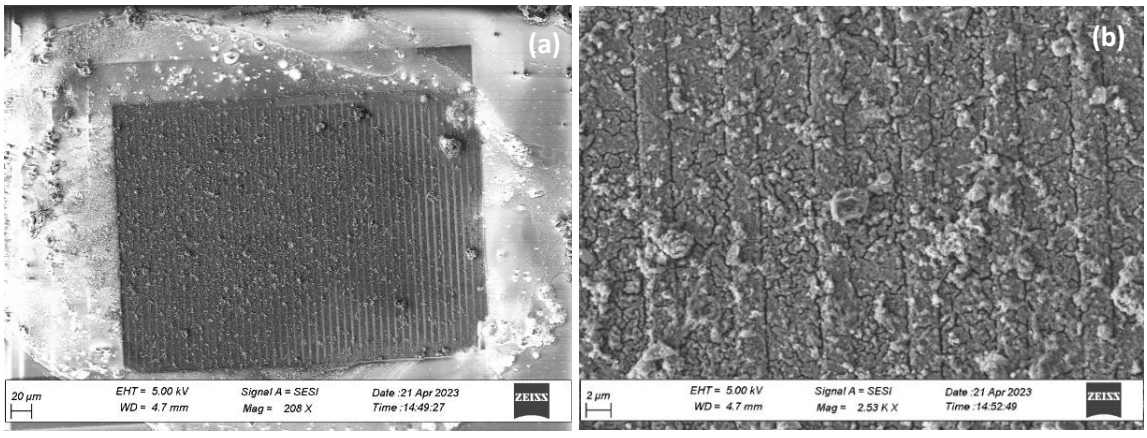

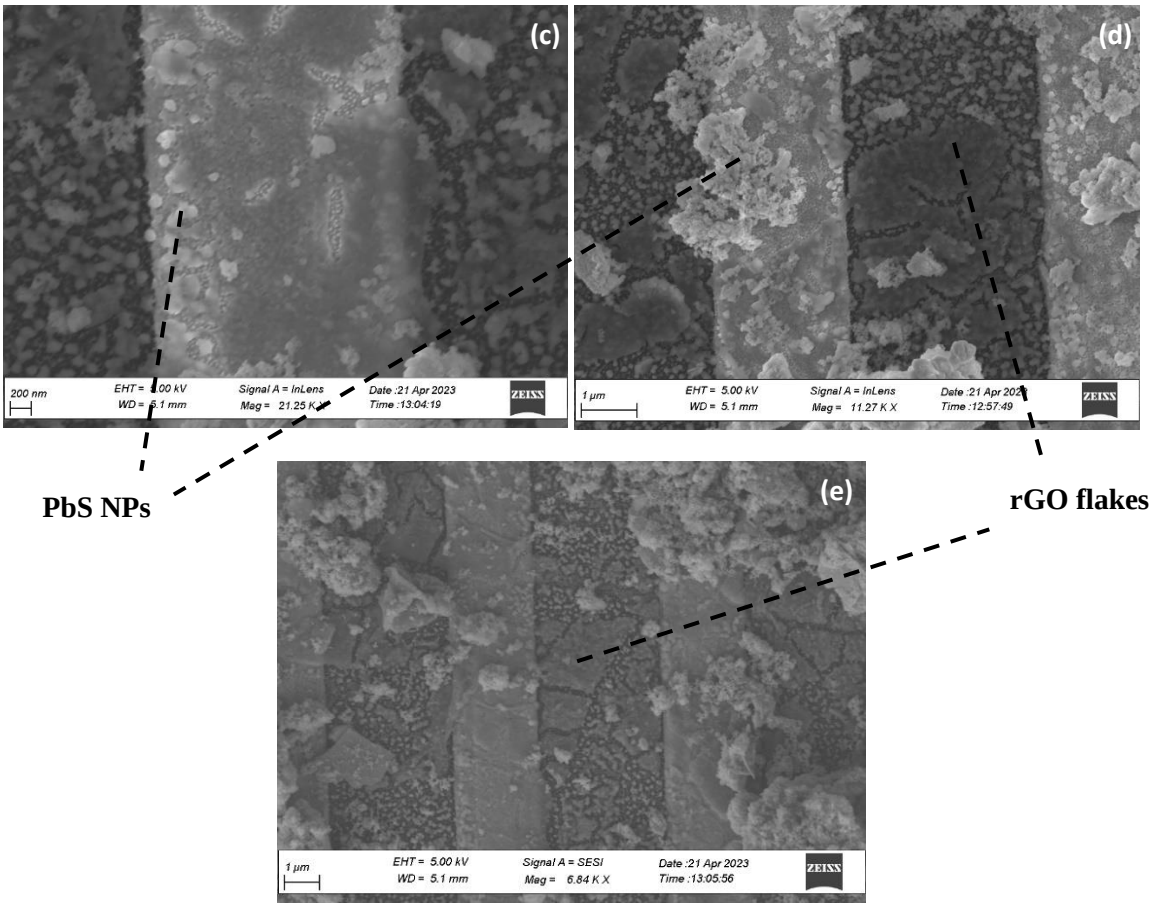

Figure 53. SEM images of rGO 3/PbS 4 a-b) rGO 4/PbS 14 c-e) deposited on IDEs.

3.3 Resistance Measurements

3.3.1 Materials deposited separately

Firstly, to assess the resistance of both materials separately and the effect of the addition of PbS nanoparticles on top of rGO flakes, resistance measurements and IV curves (Figure 54) have been recorded using the four-point prober PM8PS (a picture of the die with probes is shown in Figure 22) and the B1500 semiconductor analyser. The measurements were done at room temperature as PbS/rGO chemiresistor sensor is expected to work at RT.[21] Resistance variations are then discussed to try to understand the sensing mechanism.

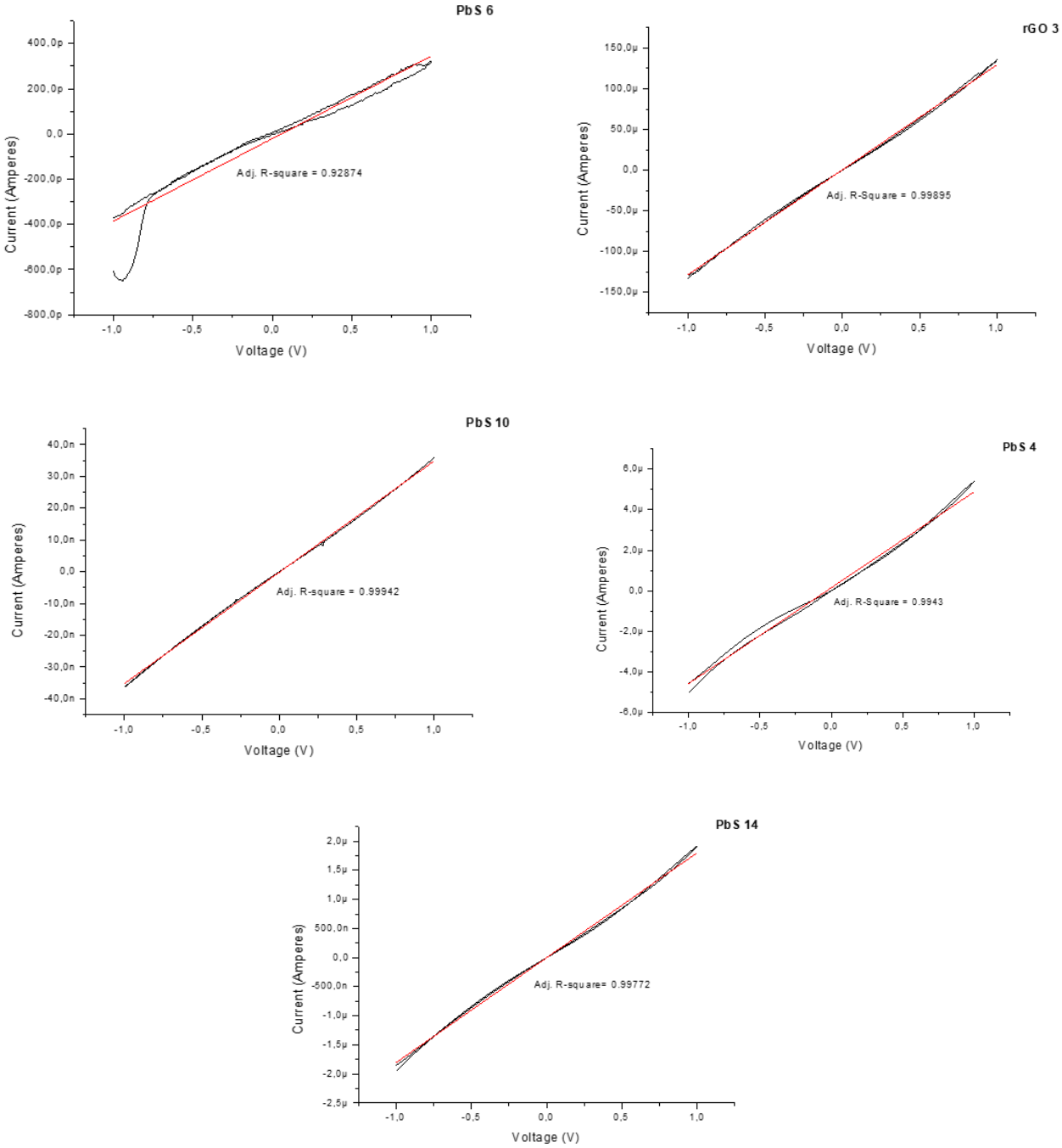

Figure 54. Some Current as a function of applied voltage graphs. Linear fit in red.

I-V curves show mostly linear behaviour of the current as a function of voltage in all cases, and this shows resistive behaviour of the devices, within the applied biasing range. It should be noted that reversing the voltage polarity of power supply influences only a little the devices current, showing a relatively symmetric electrical behaviour, again in all cases. [74] Indeed, hysteresis shown in Fig. 54 is insignificant.

Resistance values listed in Tables 16-18 are resistance values corresponding to the average of resistance values within -0.7V, 0.5V, 0.5V and 0.7V voltages. These points were chosen arbitrarily. However, since I-V curves are nearly linear, results obtained by this manner are considered as reliable. One can observe that PbS 4, followed by PbS 14 show the lowest resistance results, between 25kOhm and 430kOhm, respectively (see Table 16). The better results obtained with PbS 4 may be attributed to a higher amount of material deposited on the electrodes compared to the other PbS samples, leading to a darker appearance as shown in Figure 51-a in Section 3.2.4. Additionally, smaller electrodes consistently exhibit increased resistance, possibly due to less homogeneous material deposition resulting from a smaller surface area and coffee ring effect. Consequently, PbS particles may have reduced dispersion, leading to limitations in charge carrier transportation and therefore, to an increasing resistance.

PbS 4 and PbS 14 showed the smallest resistance values, as mentioned before, and were therefore chosen for the final devices to be tested as gas sensors. Both were deposited a second time on new dies and the resulting values are reported in Table 16 as PbS 4b and PbS 14b. Unfortunately, obtained resistance values are significantly higher compared to those from the 1st dropcasting session. Unsurprisingly, the drop casting method used in the experiment may not have been reproducible. However, despite this inconsistency, the shorter range of resistance values observed, ranging from 1.7 MOhms to 61 MOhms for PbS 4 and PbS 14 respectively, suggests that when the drop casting method could be better mastered, it can result in more consistent coatings. This change does not displace the two samples from the top positions.

Table 16 - Resistance values for PbS samples as extracted from I-V curves

Resistance (kOhm)	**Electrodes**	**PbS 4**	**PbS 4b**	**PbS 6**	**PbS 10**	**PbS 14**	**PbS 14b**
	BigS	25	$0.17*10^4$	$3.16*10^6$	$5.22*10^3$	432	2039
	BigM	233	$0.22*10^4$	$192.02*10^6$	$2.92*10^5$	Short-cut	Short-cut
	Small s	$1.25*10^6$	$1.71*10^4$	$281.91*10^6$	overload	$22.52*10^6$	$2.46*10^4$
	Small m	$8.4*10^3$	$6.11*10^4$	$359.4*10^6$	overload	overload	3943

As shown in Table 17, rGO flakes show, as expected, lower resistance values compared to PbS nanoparticles. The same rGO sample (obtained by GO reduction with NMP at 200°C, as explained in Section 1.6) was deposited on several dies. In general, the resistance values for the samples are in the range of a few hundreds of kOhms, except for the first dropped reduced graphene oxide (rGO) sample, which exhibits resistance in the megaohm range for one of the electrodes. This discrepancy could be attributed to the drop casting method not being well mastered at the beginning of the experiments, like the situation with PbS drop casting.

Table 17 – Resistance values of the rGOs as extracted from I-V curves

Resistance (kOhm)	Electrodes	rGO f	rGO 1	rGO 2	rGO 3	rGO 4
	BigS	$1.2 * 10^4$	361.35	610.09	735.66	3.99
	BigM	38.68	345.94	148.28	8.02	529.95
	Small s	286.28	$190 * 10^6$	$29 * 10^6$	525.66	30.36
	Small m	$2.6 * 10^5$	$307 * 10^6$	Short-cut	298	6.82

3.3.2 Materials deposited together

When lead sulphide (PbS) nanoparticles were deposited on the reduced graphene oxide (rGO) flakes, there was a general increase in the resistance values observed, as shown in Table 18, when compared to rGO alone. However, there were two electrodes that showed the opposite, these are indicated by being highlighted in colour. As a result, the main part (75%) of the electrodes exhibited higher resistance values in the presence of PbS nanoparticles, which was the expected outcome.

Table 18 - Resistance data of rGOs and rGO/PbS mixed samples calculated from I-V curves

Resistance (kOhm)	Electrodes	rGO 3	rGO3 + PbS 4	rGO 4	rGO 4 + PbS 14
	BigS	735.66	5.699	3.99	57.82
	BigM	8.016	$1.55*10^4$	529.95	28.47
	Small s	525.66	$22*10^6$	30.36	$1.28*10^3$
	Small m	298.27	$5.28*10^4$	6.82	$2.23*10^3$

3.3.3 Resistance as a function of temperature

Resistance tests of rGO f , PbS 4 and rGO 1/PbS 4 samples were carried out at 25°C up to 200°C with 25°C steps. (Fig. 55). The general decreasing resistance as a function of temperature might be a characteristic of semiconductor materials [114] and this non-linear behaviour could be explained by several phenomena.

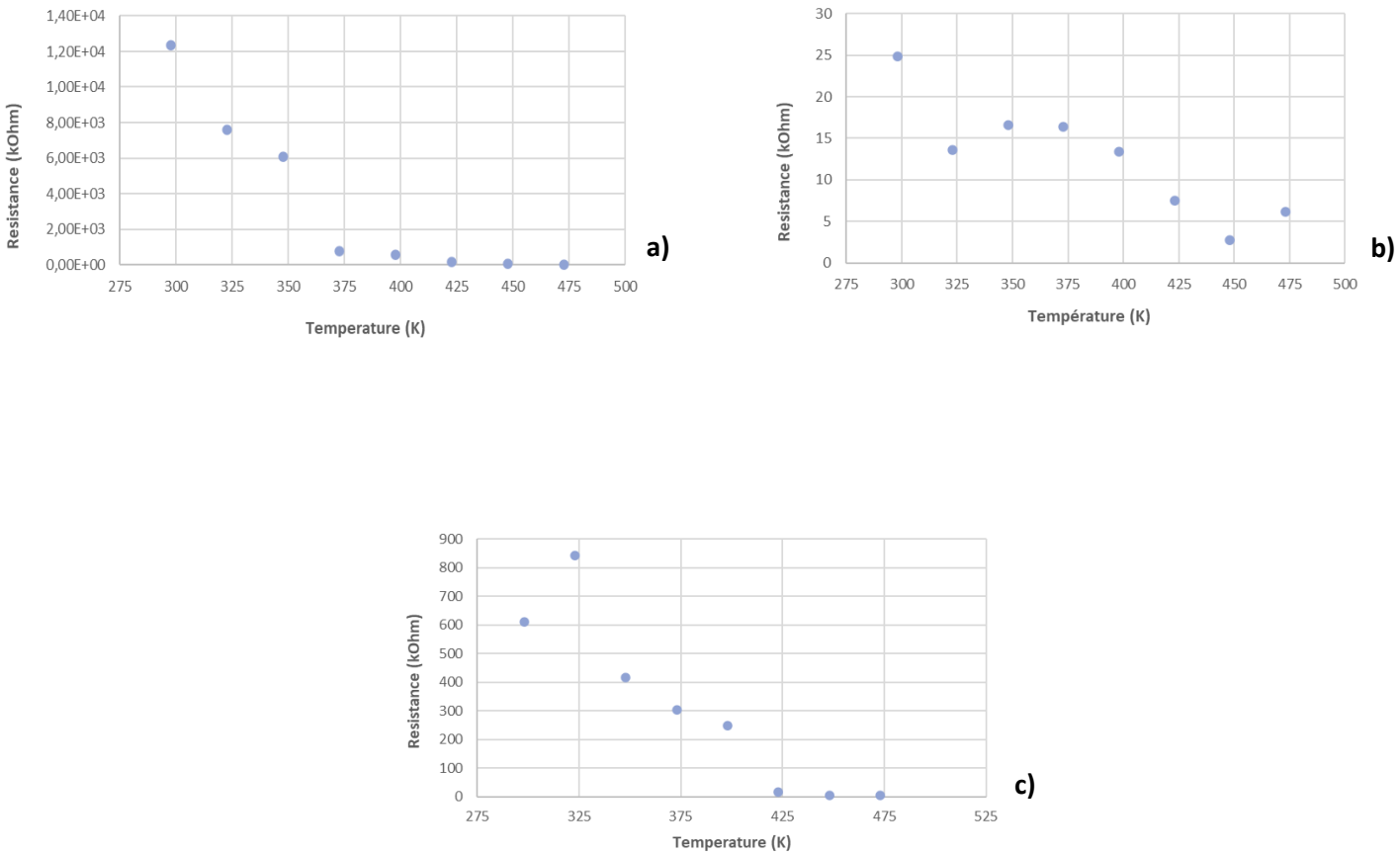

Figure 55. Resistance as a function of temperature for a) rGO f b) PbS 4 c) rGO 1/PbS 4

In the case of rGO, Baleeswaraiah M. et al. [120] explained that the nonlinear behaviour of resistance with temperature was a sign of two consecutive different temperatures regimes. At high temperatures (180K - 400K), it turns out to be a bandgap dominating transport behaviour, where a 70 meV energy bandgap is calculated. This is highlighted by a linear fit with Arrhenius-like temperature dependence of resistance. [121] While the second regime, observed at lower temperatures (50K - 180K), relies on a conduction mechanism consistent with Mott's two-dimensional variable range hopping (2D-VRH). [122] It means that the carrier transport is via electrons hopping between localized states and that the increasing temperature would increase the hopping distance of carriers.

The first regime, occurring at high temperatures, is supported by the linear fit to the Arrhenius temperature dependence $R \sim \exp(E_a / 2\,k\,T)$, [120] where E_a is an activation energy (which can be the band gap), k is the Boltzmann constant, and T is the temperature is shown in Figure 56. As expected from [120], a linear fit (Fig. 57) to the Arrhenius plot (Fig. 56) appears at high temperatures – between 100°C-200°C in our case – and it might be linked to the bandgap dominating transport behaviour. The calculated activation energy (E_a) is 1.77 eV and is considered plausible because it falls within the expected range, which can span from 0 eV for pristine graphene to values exceeding 2.5 eV. [111] Nevertheless, to confirm that the calculated E_a is related to the band gap between CB and VB, it would have been interesting to corroborate E_a behaviour with the degree of reduction of rGO by using XPS analysis-generated O/C ratios. It is worth noting that as the reduced graphene oxide becomes more reduced, the bandgap energy decreases. [111]

The second regime, occurring at lower temperatures, is supported by the best fit to 2D-VHR. This fit helps to determine the characteristic T° of the regime and its density of states at the Fermi level. [120] Unfortunately, the three experimental data points in this work are insufficient to fully confirm this fitting (see Figure 57). A bigger range of temperature should have been achieved. However, at low temperatures (25°C to 100°C), a linear relationship can still be observed in the Arrhenius plot and the calculated activation energy is 254 meV. The decrease in activation energy as temperature decreases indicate carrier transport occurring through electron hopping between localized states, characterized by the second regime. [120] At 100°C, a transition in conduction regime of rGO occurs and is likely due to water removal causing rGO flakes aggregation and a decrease in contact resistance at the electrode/graphene interface.

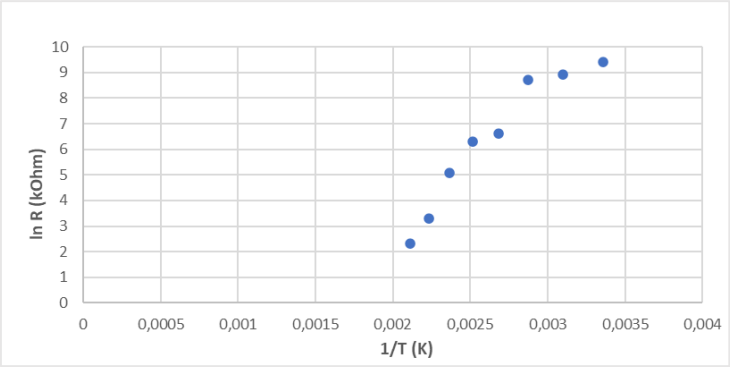

Figure 56. Arrhenius plot of resistance as a function of temperature of rGO f

To obtain a more accurate estimation of the transition temperature, a linear regression analysis was conducted on the two temperature ranges. The fits obtained from this analysis were

extrapolated, ensuring that the two fitting lines intersected. The point of intersection represents the transition temperature, while the slope extracted from the fitting lines provides the activation energy. Fig. 57 exhibited clearly distinguishable curves, enabling the extraction of a reliable crossing point and consistent activation energy.

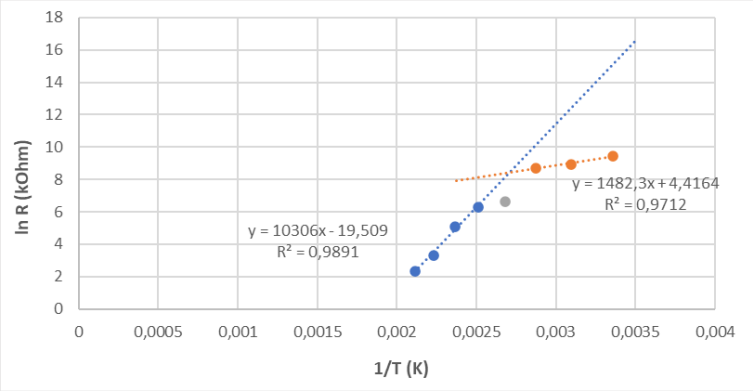

Figure 57. Arrhenius plot of resistance as a function of temperature of rGO f. Blue and orange linear fitting curves are extrapolated until the crossing point.

In the case of PbS alone, Fig. 55-b shows two suspected regimes with a transient occurring at 150°C. Two distinct transport mechanisms are reported in [114] for PbS with conductivity plotted as $\sigma = \sigma_0 \exp(-\frac{E_a}{k_B T})$ where σ_0 is a constant, E_a is the thermal activation energy, k_B is the Boltzmann constant, and T is the temperature. In this work, the conduction mechanism from 25°C to 150°C could be attributed to the variable range hopping (VRH) followed by the nearest neighbour hopping (NNH) conduction mechanism. At higher temperatures (in our case, from 150°C to 200°C), the conduction path might be caused by the hole excitation into the valence band from the acceptor level (conduction band) involving inter-grain conduction in the nanospheres due to the coalescence of the NPs. [123] E_a is a combination of both activation energies associated with both hole excitation and inter-grain conduction. Additionally, there is an increasing acceptor carrier concentration as temperature increases, bringing the Fermi level nearer to the valence band edge. For this reason, the overall activation energy (E_a) will decrease. [114] Unfortunately, the linear fit applied to our PbS curve is insufficiently precise (see figure 58). Therefore, calculation of the bandgap energy is unfeasible. Moreover, as mentioned in Section 3.2.2, DR UV visible analyses were done on PbS samples to calculate the bandgap but unfortunately, all PbS samples seem to have a too strong absorption (see Section 6.5) and these calculations were also therefore impossible. Overall, three successive conduction mechanisms are suspected for PbS as temperature increases: VRH, NNH and then hole excitation into the valence band from the acceptor level.

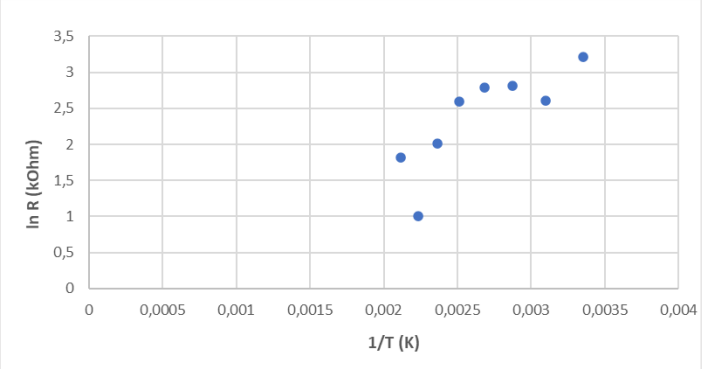

Figure 58. Arrhenius plot of resistance as a function of temperature of PbS 4

For the rGO/PbS mixed sample, resistance behaviour (Fig 55-c) at first seems to show a PbS-QDs dominated transport. Indeed, one can observe a transition occurring upon annealing from 150°C as for the PbS system. This behaviour could be related to a reduction on the interdot spacing involving an inter-grain conduction as mentioned above. However, very low resistance values from 150°C also suggest the bandgap dominating transport of rGO.

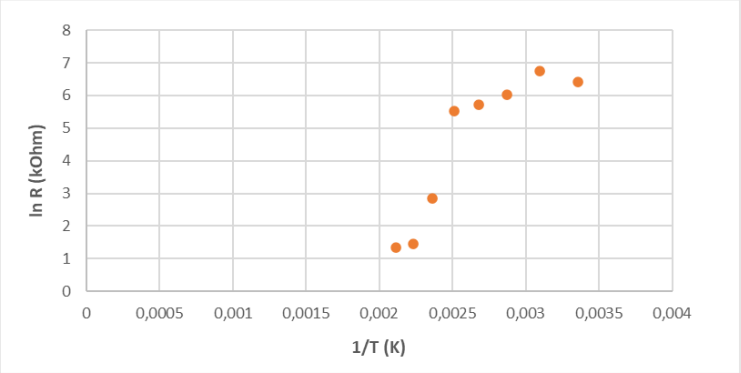

Figure 59. Arrhenius plot of resistance as a function of temperature of rGO 1/PbS 4

The linear regression (see Section 6.6) from the Arrhenius plot of rGO/PbS (Fig. 59) analysis is inadequate, making it impossible to determine the transitional temperature that could be related to two distinct regimes.

In general, it might be quite hard to precisely determine the conduction mechanism since both rGO and PbS nanoparticles are reported to be p-type semiconductors, and both may simultaneously play a role by limiting charge carrier transportation in the mixed rGO/PbS sample rGO/PbS, in addition to coupled effects, such as charge transfer in the heterojunction of PbS and rGO. The basic mechanism is illustrated in Section 1.7.1.

3.4 Preliminary gas sensing measurements

The selected samples were analysed for a first preliminary gas sensing measurement as explained in Section 2.7.14. Unfortunately, none of the devices showed any sensitivity to the calibration gas of air/methane (see Figure 60). An example of a typical response to the methane gas molecule is shown in Figure 61 as reported in [21]

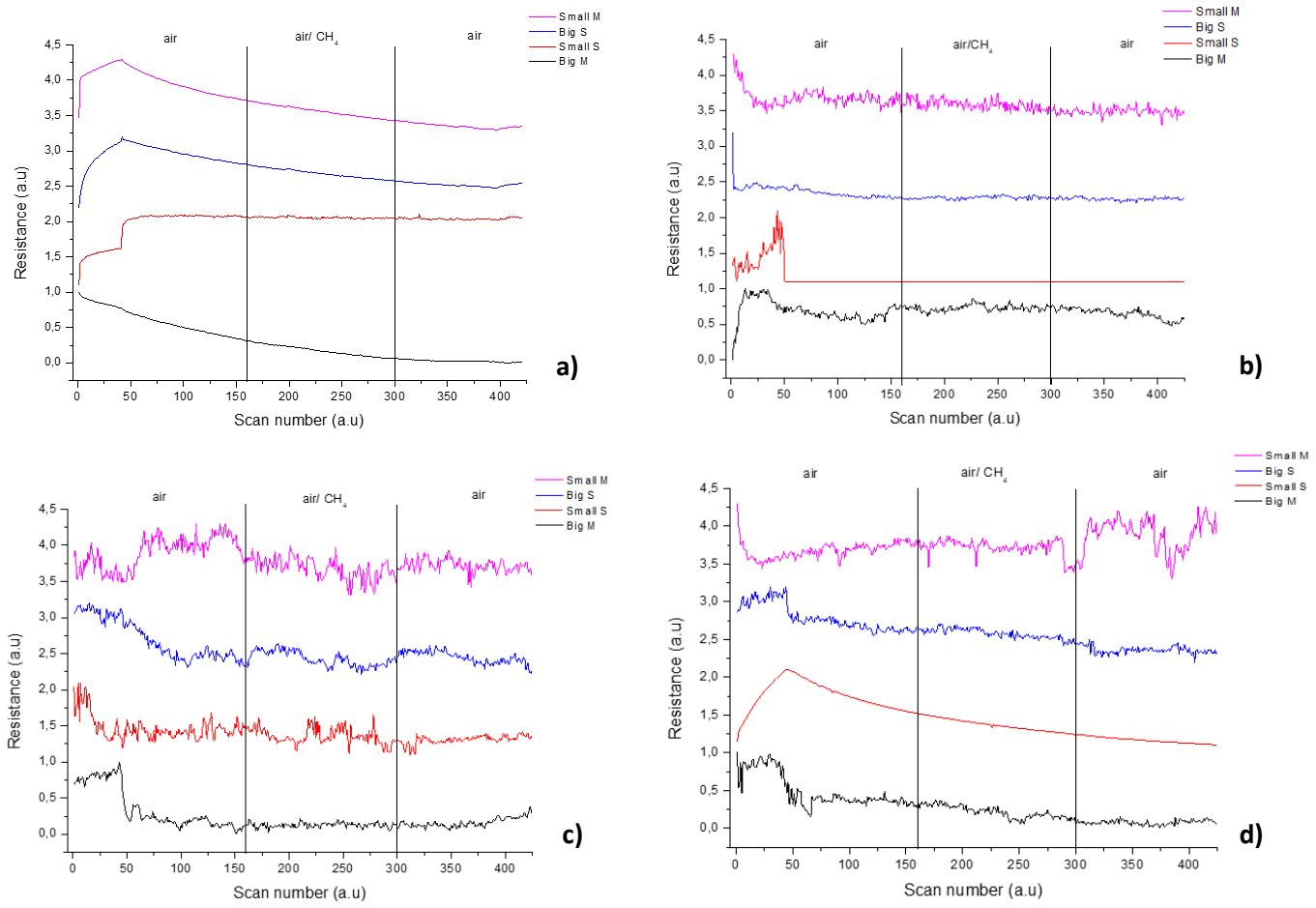

Figure 60. Normalized curves of the resistance response to methane atmosphere under the conditions mentioned in Section 2.7.14 for samples PbS 14b (a) rGO 2 (b) rGO 3/PbS 4 (c) rGO 4/ PbS 14 (d)

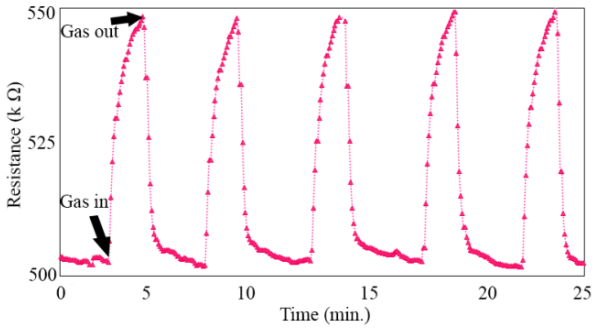

Figure 61. Gas sensing and recovery test of PbS/rGO sensor with 3.5 wt% rGO toward 1% methane [21]

Reduced graphene oxide alone does not show any sensitivity to methane (Fig. 60-b), but this behaviour was expected since rGO is supposed to act as a conducting network with excellent electron-transfer efficiency. [21] On the other hand, PbS nanocrystals were expected to function as reaction centres but do not show any sensitivity to methane. This might be linked to the sort of competition in the charge transport mechanisms occurring in rGO/PbS sensors.

Other hypotheses have been proposed to explain this absence of sensitivity. Hybrid nanomaterials based on rGO are usually prepared by an in-situ method meaning that nanostructures are directly prepared in the presence of graphene solution, or two previously prepared solutions are directly mixed.[48] The present work presented PbS nanoparticles and reduced graphene oxide synthesised separately, and which were never in contact with one another before the deposition on the IDEs. This must have obviously had consequences on the dispersion of rGO and PbS NPs on the surface of the electrodes. Also, one must remind that rGO and PbS were dispersed in different solvents (milli-Q water and ink solution, respectively) and the difference in viscosity might have increased the disparity in the resulted materials dispersion. Furthermore, the literature reports that the NCs synthesized using the exact same reactants and concentration as in this work (refer to Table 2 in Section 1.7) have a size of 40nm, whereas the NCs produced in this work are smaller, measuring around 10nm. It is therefore likely that this notable size difference has been caused by the presence of GO flakes during the NPs formation. in the published results. As sensing occurs on the surface, particle size effects might exert a strong influence on the obtained results.

IV. CONCLUSIONS & PERSPECTIVES

4.1 General conclusion

In conclusion, as outlined in the Introduction, the main goal of this Master thesis has been achieved, namely reduced graphene oxide and lead sulphide nanocrystals have been synthesized separately and deposited on IDEs. To reach this goal, each step has been studied separately and the following conclusions can be reached as detailed below.

First, concerning the reduction of GO, the experimental parameters connected to temperature, Vitamin C concentration, organic and aqueous solvents natures have all impacted the reduction rate of the graphene oxide flakes. Increasing the temperature of the reduction process led to a general improvement in the reduction rates. Vitamin C, as expected, worked well as a green reducing agent as much for 1-methyl 2-pyrrolidone (NMP)-based as for water-based reductions. The resulting rGO displayed a few micrometres to tens of micrometres flakes, as well as good suspensions rate in water and in ink-solution which is useful for further depositions. When considering all the results collectively, it appears that the reduction using the organic NMP at 200°C has given the most reduced graphene oxide sample, as confirmed by FTIR, XPS, TGA and Raman analyses. Despite its convenient high boiling point and its adequacy with rGO, NMP remains a toxic compound. The good news is that the water-based reduction of GO at 90°C resulted in a similar removal of oxygen-containing groups as the rGO NMP reduction at 200°C. This was confirmed through TGA, XPS and FTIR analyses. Additionally, it appeared that the water-based 90°C caused less damage to the carbon base planes as indicated by TGA, although it also led to a lower sp^2/sp^3 carbon ratio compared to rGO NMP 200. Using aqueous solvents, known for their eco-friendliness, could be a good option for eco-friendly sensor devices elaborations in the future.

Second, regarding PbS synthesis, according to XRD patterns, all the resulting nanoparticles prepared by the first protocol, are crystalline but still have some amorphous phase compared to the second protocol. According to calculations using the Scherrer equation, the crystallites have an average size of approximately 10nm. The SEM and TEM images reveal spherical NPs, with the most distinct spheres measuring around 20nm in diameter. In contrast to the first protocol, the second method, considered as a hot injection method, produced larger cubic NPs ranging from 40nm to micrometres in size. The crystallites within these nanoparticles have an average diameter of approximately 35nm, as determined by the Scherrer equation. In general, PbS nanoparticles are polycrystalline and tend to aggregate and precipitate as confirmed by SEM and TEM. Therefore, they need hard sonication to make homogenous dispersions for further

deposition. Also, lead sulphide nanocrystals arising from the 1st protocol with lead nitrate and sodium sulphide as precursors, exhibited suitable S:Pb molar ratio and high purity – with a lead percentage higher than 82% – regardless of the sodium sulphide dripping time and of the presence of the capping agent 2-mercaptoethanol or not. XRF showed S:Pb ratios around 1.2, thus with an excess of sulphur, while ICP revealed a better stoichiometry with ratios around 0.99, thus with a slight excess of lead. The general higher weight percentages of S:Pb observed with XRF indicate some possible surface S enrichment. Both XRF and ICP analyses are relevant, and they provide complementary information.

Finally, the mastering of the deposition method as well as the electrodes surface areas turned out to be very impacting for the resulting morphologies of the deposited materials. Indeed, resistance measurements tended to give higher values for small electrodes, which were more victims of the so-called coffee ring effect, shifting the materials on the sides of the electrodes. Deposited reduced graphene oxide, due to its exceptional crystal lattice, showed a significant higher conductivity, as expected, compared to PbS nanoparticles. Moreover, when these nanoparticles were added on top of rGO, resistance increased for most of the electrodes, as expected.

The most difficult task was to determine the sensing and conduction mechanisms. When the four devices selected were tested under the methane calibration gas, none of the devices were sensitive. However, it was observed that the resistance decreased as a function of temperature and based on this behaviour, two conduction regimes may occur within the materials. As the temperature increases, rGO goes from Mott's two-dimensional variable range hopping regime to a bandgap dominating transport regime. Calculated activation energies of first and second regimes go from 254 meV to 1.77 eV. These values could be related to the bandgap energy, but it still must be corroborated with degrees of reduction of rGO. By contrast, PbS NPs start with a variable range hopping (VRH) followed by the nearest neighbour hopping (NNH) conduction mechanism and end with an inter-grain conduction in the nanospheres due to a coalescence phenomenon. Unfortunately, UV-visible analysis of PbS as well as linear fit of Arrhenius plot of PbS and rGO/PbS were inconclusive. Therefore, it was impossible to determine the corresponding bandgap energies and thus to confirm the intrinsic semi-conductivity of these devices. Interestingly, rGO/PbS seems to show a combination of the conduction mechanisms of both materials. Therefore, both may simultaneously play a role by limiting charge carrier transportation of rGO/PbS, in addition to coupled effects, such as charge

transfer in the heterojunction of PbS and rGO whose mechanism were suggested and detailed in Section 1.7.1.

The gas sensing measurements were unsuccessful for rGO f, PbS 14 as well as both rGO 3/PbS 4 and rGO 4/PbS 14. rGO flakes were not expected to act as sensing material but surprisingly, PbS nanoparticles did not show any reactivity even in the presence of rGO flakes. Three hypotheses are raised to explain this lack of sensitivity: (1) the possible limitation of the charge carrier transportation in rGO/PbS, (2) the preparation of rGO and PbS hybrids that was not achieved *in situ* and (3) the intrinsic low polarizability of methane. In this regard, further investigation about the preparation and the dispersions of both reduced graphene oxide and lead sulphide nanoparticles, separately and together, should be conducted.

4.2 Perspectives

This work could be improved in many different ways; thus, this section will briefly discuss how one can put these propositions for future work in practice.

Gas interaction depends mainly on effective surface area available on the materials. Graphene sheets provide outstanding surface area due to the low number of stacked layers and their dispersion. A higher number of staked layers increases the adsorption energy required for methane detection. [124] Nevertheless, when graphene-dispersion solutions are dried, graphene sheets tend to re-aggregate due to van der Waals and π-π stacking interactions among the sheets. It is reported that the incorporation of nanostructures, such as nanoparticles, prevents this agglomeration to occur and moreover it helps to achieve a good distribution of these nanostructures. [48] Therefore, a deposition "stack by stack" – alternance of rGO and PbS – might be a good compromise to create an efficient incorporation as just explained. This stack-by-stack process could be achieved with an ink-jet printer to get rid of the drawbacks of a manually deposition method as used in this work and to obtain a better reproducibility. Moreover, both materials could be dispersed in an ink-solution and therefore exhibit the same viscosity.

Furthermore, testing the gas with the 35 nm and 40 nm cubic nanoparticles obtained by the second protocol will help to assess the relevance of size, considering that the only reported rGO/PbS sensor [21] so far presented a crystallite size of 40 nm. This investigation would also explore the potential relationship between NP shapes, surface interactions, and methane adsorption. Also, as the sodium sulphide dripping time and the presence of capping agent did not seem to play an important role regarding the shapes, crystallinity, and purity of the NPs

prepared by the first protocol, one can now play on the temperature since this parameter directly impacts the favoured exposed facets of the NCs during their formation. [115]

Eventually, gas sensing measurements could be tested with 90°C water-based rGO as its reduction rate appears to be close to the efficiency of NMP 200°C rGO. The latter needs carbon restoration due to its carbon loss. An interesting approach for repairing sp^2 carbons involves using ethanol as a carbon source [125] which could be considered additionally. Ethanol, when interacting with etch holes and carbon dangling bonds at 200°C, effectively promotes the formation of new hexagonal carbon rings within the reduced graphene oxide.[125] This enhances the degree of graphitization and reduces the risk of defect enlargement caused by the migration of epoxides and hydroxyls. The combination of graphene oxide reduced in NMP with Vitamin C and ethanol would be an interesting option to test, as well as a combination of graphene oxide reduced in water at 90°C, with Vitamin C and ethanol.

V. BIBLIOGRAPHY

[1] T. D. Brock, “Zehnder AJB, Brock TD.. Methane formation and methane oxidation by methanogenic bacteria Yellowstone Thermal Biology View project,” 1979. [Online]. Available: https://www.researchgate.net/publication/22380343

[2] M. Z. Jiao, X. Y. Chen, K. X. Hu, D. Y. Qian, X. H. Zhao, and E. J. Ding, “Recent developments of nanomaterials-based conductive type methane sensors,” *Rare Metals*, vol. 40, no. 6. University of Science and Technology Beijing, pp. 1515–1527, Jun. 01, 2021. doi: 10.1007/s12598-020-01679-9.

[3] R. Ghosh, M. Aslam, and H. Kalita, “Graphene derivatives for chemiresistive gas sensors: A review,” *Materials Today Communications*, vol. 30. Elsevier Ltd, Mar. 01, 2022. doi: 10.1016/j.mtcomm.2022.103182.

[4] J. Kamieniak, E. P. Randviir, and C. E. Banks, “The latest developments in the analytical sensing of methane,” *TrAC - Trends in Analytical Chemistry*, vol. 73. Elsevier B.V., pp. 146–157, Nov. 01, 2015. doi: 10.1016/j.trac.2015.04.030.

[5] D. J. Wuebbles and K. Hayhoe, “Atmospheric methane and global change,” 2001. [Online]. Available: www.elsevier.com/locate/earscirev

[6] SPF Santé publique, “Climat.be,” *Émissions par gaz à effet de serre*, 2023. https://climat.be/en-belgique/climat-et-emissions/emissions-des-gaz-a-effet-de-serre/emissions-par-gaz (accessed May 19, 2023).

[7] R. Kupers and D. Zavala-Araiza, “An Eye on Methane: International Methane Emissions Observatory 2022 Report,” Nairobi, 2022.

[8] A. M. Thompson, K. B. Hogan, and J. S. Hoffman, “METHANE REDUCTIONS: IMPLICATIONS FOR GLOBAL WARMING AND ATMOSPHERIC CHEMICAL CHANGE,” 1992.

[9] V. Ghanshyam.L and R. A.R, “New measurement of the rate coefficient for the reaction of OH with methane.,” *Letters to Nature*, Apr. 1991.

[10] N. S. Lawrence, “Analytical detection methodologies for methane and related hydrocarbons,” in *Talanta*, Elsevier, Apr. 2006, pp. 385–392. doi: 10.1016/j.talanta.2005.10.005.

[11] P. Jacquinot, B. Wehrli, and P. C. Hauser, “Determination of methane and other small hydrocarbons with a platinum-Nafion electrode by stripping voltammetry,” 2001.

[12] T. Hong, J. T. Culp, K. J. Kim, J. Devkota, C. Sun, and P. R. Ohodnicki, “State-of-the-art of methane sensing materials: A review and perspectives,” *TrAC - Trends in Analytical Chemistry*, vol. 125. Elsevier B.V., Apr. 01, 2020. doi: 10.1016/j.trac.2020.115820.

[13] Lens.org, “Patent analysis. Methane sensor.”

[14] “Proceedings,” in *Second International Meeting on Chemical Sensor*, Bordeaux, 1986.

[15] B. Elsevier, J.-J. Ehrhardt, L. Colin, and D. Jamois, “s SORs ACTU/gORS Poisoning of platinum surfaces by hexamethyldisiloxane (HMDS): application to catalytic methane sensors,” 1997.

[16] B. Culshaw, G. Stewart, F. Dong, C. Tandy, and D. Moodie, “Fibre optic techniques for remote spectroscopic methane detection—from concept to system realisation,” *Sens Actuators B Chem*, vol. 51, no. 1–3, pp. 25–37, Aug. 1998, doi: 10.1016/S0925-4005(98)00184-1.

[17] S. Svanberg, “Laser spectroscopy for medical applications,” in *Laser Spectroscopy for Sensing*, Elsevier, 2014, pp. 421–460. doi: 10.1533/9780857098733.3.421.

[18] A. J. Miles and B. A. Wallace, “Circular Dichroism Spectroscopy for Protein Characterization,” in *Biophysical Characterization of Proteins in Developing Biopharmaceuticals*, Elsevier, 2015, pp. 109–137. doi: 10.1016/B978-0-444-59573-7.00006-3.

[19] A. P. Craig, A. S. Franca, and J. Irudayaraj, “Vibrational spectroscopy for food quality and safety screening,” in *High Throughput Screening for Food Safety Assessment*, Elsevier, 2015, pp. 165–194. doi: 10.1016/B978-0-85709-801-6.00007-1.

[20] Y. Jian *et al.*, “Gas Sensors Based on Chemi-Resistive Hybrid Functional Nanomaterials,” *Nano-Micro Letters*, vol. 12, no. 1. Springer, Mar. 01, 2020. doi: 10.1007/s40820-020-0407-5.

[21] H. Roshan, M. H. Sheikhi, M. K. Faramarzi Haghighi, and P. Padidar, “High-Performance Room Temperature Methane Gas Sensor Based on Lead Sulfide/Reduced Graphene Oxide Nanocomposite,” *IEEE Sens J*, vol. 20, no. 5, pp. 2526–2532, Mar. 2020, doi: 10.1109/JSEN.2019.2951511.

[22] S. Choopun, N. Hongsith, and E. Wongrat, “Metal-Oxide Nanowires for Gas Sensors,” in *Nanowires - Recent Advances*, InTech, 2012. doi: 10.5772/54385.

[23] J. He, C. Cheng, and J. Hu, “Electrical degradation of double-Schottky barrier in ZnO varistors,” *AIP Adv*, vol. 6, no. 3, p. 030701, Mar. 2016, doi: 10.1063/1.4944485.

[24] F. Greuter and G. Blatter, “Electrical properties of grain boundaries in polycrystalline compound semiconductors,” *Semicond Sci Technol*, vol. 5, no. 2, pp. 111–137, Feb. 1990, doi: 10.1088/0268-1242/5/2/001.

[25] Y. Sato *et al.*, “Role of Pr Segregation in Acceptor-State Formation at ZnO Grain Boundaries,” *Phys Rev Lett*, vol. 97, no. 10, p. 106802, Sep. 2006, doi: 10.1103/PhysRevLett.97.106802.

[26] Y. Sato, T. Yamamoto, and Y. Ikuhara, “Atomic Structures and Electrical Properties of ZnO Grain Boundaries,” *Journal of the American Ceramic Society*, vol. 90, no. 2, pp. 337–357, Feb. 2007, doi: 10.1111/j.1551-2916.2006.01481.x.

[27] F. Stucki and F. Greuter, “Key role of oxygen at zinc oxide varistor grain boundaries,” *Appl Phys Lett*, vol. 57, no. 5, pp. 446–448, Jul. 1990, doi: 10.1063/1.103661.

[28] P. R. Bueno, E. R. Leite, M. M. Oliveira, M. O. Orlandi, and E. Longo, “Role of oxygen at the grain boundary of metal oxide varistors: A potential barrier formation mechanism,” *Appl Phys Lett*, vol. 79, no. 1, pp. 48–50, Jul. 2001, doi: 10.1063/1.1378051.

[29] K. S. Novoselov *et al.*, “Two-dimensional atomic crystals,” 2005. [Online]. Available: www.pnas.orgcgidoi10.1073pnas.0502848102

[30] H. J. Yoon, D. H. Jun, J. H. Yang, Z. Zhou, S. S. Yang, and M. M. C. Cheng, “Carbon dioxide gas sensor using a graphene sheet,” *Sens Actuators B Chem*, vol. 157, no. 1, pp. 310–313, Sep. 2011, doi: 10.1016/j.snb.2011.03.035.

[31] Y. Liu, X. Dong, and P. Chen, “Biological and chemical sensors based on graphene materials,” *Chem Soc Rev*, vol. 41, no. 6, pp. 2283–2307, Feb. 2012, doi: 10.1039/c1cs15270j.

[32] W. Ye, X. Li, J. Luo, X. Wang, and R. Sun, “Lignin as a green reductant and morphology directing agent in the fabrication of 3D graphene-based composites for high-performance supercapacitors,” *Ind Crops Prod*, vol. 109, pp. 410–419, Dec. 2017, doi: 10.1016/j.indcrop.2017.08.047.

[33] N. M. Julkapli and S. Bagheri, “Graphene supported heterogeneous catalysts: An overview,” *Int J Hydrogen Energy*, vol. 40, no. 2, pp. 948–979, Jan. 2015, doi: 10.1016/j.ijhydene.2014.10.129.

[34] B. G. Zaragoza-Palacios, A. R. Torres-Duarte, and S. J. Castillo, “Synthesis and characterization of nanoparticles and thin films of PbS by a high-performance procedure using CBD,” *Journal of Materials Science: Materials in Electronics*, vol. 32, no. 17, pp. 22205–22213, Sep. 2021, doi: 10.1007/s10854-021-06702-y.

[35] A. K. Geim and K. S. Novoselov, “The rise of graphene,” *Nat Mater*, vol. 6, no. 3, pp. 183–191, Mar. 2007, doi: 10.1038/nmat1849.

[36] F. Yavari and N. Koratkar, “Graphene-Based Chemical Sensors,” *J Phys Chem Lett*, vol. 3, no. 13, pp. 1746–1753, Jul. 2012, doi: 10.1021/jz300358t.

[37] K. S. Novoselov *et al.*, “Electric Field Effect in Atomically Thin Carbon Films,” Kluwer, 2000. [Online]. Available: http://science.sciencemag.org/

[38] M. J. Allen, V. C. Tung, and R. B. Kaner, “Honeycomb carbon: A review of graphene,” *Chem Rev*, vol. 110, no. 1, pp. 132–145, Jan. 2010, doi: 10.1021/cr900070d.

[39] C. Berger *et al.*, “Electronic Confinement and Coherence in Patterned Epitaxial Graphene,” *Science (1979)*, vol. 312, no. 5777, pp. 1191–1196, May 2006, doi: 10.1126/science.1125925.

[40] A. Reina *et al.*, “Large area, few-layer graphene films on arbitrary substrates by chemical vapor deposition,” *Nano Lett*, vol. 9, no. 1, pp. 30–35, Jan. 2009, doi: 10.1021/nl801827v.

[41] X. Li *et al.*, “Large-Area Synthesis of High-Quality and Uniform Graphene Films on Copper Foils,” *Science (1979)*, vol. 324, no. 5932, pp. 1312–1314, Jun. 2009, doi: 10.1126/science.1171245.

[42] R. Vargas-Bernal, “Electrical properties of two-dimensional materials used in gas sensors,” *Sensors (Switzerland)*, vol. 19, no. 6. MDPI AG, Mar. 02, 2019. doi: 10.3390/s19061295.

[43] D. R. Dreyer, S. Park, C. W. Bielawski, and R. S. Ruoff, “The chemistry of graphene oxide,” *Chem. Soc. Rev.*, vol. 39, no. 1, pp. 228–240, 2010, doi: 10.1039/B917103G.

[44] W. S. Hummers and R. E. Offeman, “Preparation of Graphitic Oxide,” Sep. 1957.

[45] T.-Y. ZHANG and D. ZHANG, “Aqueous colloids of graphene oxide nanosheets by exfoliation of graphite oxide without ultrasonication,” *Bulletin of Materials Science*, vol. 34, no. 1, pp. 25–28, Feb. 2011, doi: 10.1007/s12034-011-0048-x.

[46] J. Park, Y. Kim, S. Y. Park, S. J. Sung, H. W. Jang, and C. R. Park, “Band gap engineering of graphene oxide for ultrasensitive NO2 gas sensing,” *Carbon N Y*, vol. 159, pp. 175–184, Apr. 2020, doi: 10.1016/j.carbon.2019.11.063.

[47] J. T. Robinson, F. K. Perkins, E. S. Snow, Z. Wei, and P. E. Sheehan, “Reduced graphene oxide molecular sensors,” *Nano Lett*, vol. 8, no. 10, pp. 3137–3140, Oct. 2008, doi: 10.1021/nl8013007.

[48] F. L. Meng, Z. Guo, and X. J. Huang, “Graphene-based hybrids for chemiresistive gas sensors,” *TrAC - Trends in Analytical Chemistry*, vol. 68. Elsevier B.V., pp. 37–47, May 01, 2015. doi: 10.1016/j.trac.2015.02.008.

[49] B. Yuan *et al.*, “A facile approach to prepare graphene via solvothermal reduction of graphite oxide,” *Mater Res Bull*, vol. 55, pp. 48–52, Jul. 2014, doi: 10.1016/j.materresbull.2014.04.016.

[50] K. Dave, K. H. Park, and M. Dhayal, “Two-step process for programmable removal of oxygen functionalities of graphene oxide: functional, structural and electrical characteristics,” *RSC Adv*, vol. 5, no. 116, pp. 95657–95665, Oct. 2015, doi: 10.1039/c5ra18880f.

[51] Z. Bo *et al.*, “Green preparation of reduced graphene oxide for sensing and energy storage applications,” *Sci Rep*, vol. 4, Apr. 2014, doi: 10.1038/srep04684.

[52] N. Sharma, R. Vyas, V. Sharma, H. Rahman, S. K. Sharma, and K. Sachdev, “A comparative study on gas-sensing behavior of reduced graphene oxide (rGO) synthesized by chemical and environment-friendly green method,” *Applied Nanoscience (Switzerland)*, vol. 10, no. 2, pp. 517–528, Feb. 2020, doi: 10.1007/s13204-019-01138-7.

[53] M. J. Fernández-Merino *et al.*, “Vitamin C is an ideal substitute for hydrazine in the reduction of graphene oxide suspensions,” *Journal of Physical Chemistry C*, vol. 114, no. 14, pp. 6426–6432, Apr. 2010, doi: 10.1021/jp100603h.

[54] A. H. Hamza, Ed., *Vitamin C*. InTech, 2017. doi: 10.5772/66058.

[55] J. Chang and E. R. Waclawik, “Colloidal semiconductor nanocrystals: Controlled synthesis and surface chemistry in organic media,” *RSC Advances*, vol. 4, no. 45. Royal Society of Chemistry, pp. 23505–23527, 2014. doi: 10.1039/c4ra02684e.

[56] A. Urbieta, P. Fernández, and J. Piqueras, “Growth and luminescence properties of micro- and nanoneedles in sintered CdSe,” *Appl Phys Lett*, vol. 85, no. 24, pp. 5968–5970, Dec. 2004, doi: 10.1063/1.1830083.

[57] J.-J. Wu and S.-C. Liu, “Low-Temperature Growth of Well-Aligned ZnO Nanorods by Chemical Vapor Deposition,” *Advanced Materials*, vol. 14, no. 3, pp. 215–218, Feb. 2002, doi: 10.1002/1521-4095(20020205)14:3<215::AID-ADMA215>3.0.CO;2-J.

[58] G. A. OZIN, M. R. STEELE, and A. J. HOLMES, “ChemInform Abstract: Intrazeolite Topotactic MOCVD. 3-Dimensional Structure-Controlled Synthesis of II-VI Semiconductor Nanoclusters.,” *ChemInform*, vol. 25, no. 46, p. no-no, Aug. 2010, doi: 10.1002/chin.199446007.

[59] N. Abid *et al.*, “Synthesis of nanomaterials using various top-down and bottom-up approaches, influencing factors, advantages, and disadvantages: A review,” *Adv Colloid Interface Sci*, vol. 300, p. 102597, Feb. 2022, doi: 10.1016/j.cis.2021.102597.

[60] X. Peng and J. Thessing, “Controlled synthesis of high quality semiconductor nanocrystals,” *Struct Bond*, vol. 118, pp. 79–119, Sep. 2005, doi: 10.1007/b137472.

[61] J. V. Williams, N. A. Kotov, and P. E. Savage, “A Rapid Hot-Injection Method for the Improved Hydrothermal Synthesis of CdSe Nanoparticles,” *Ind Eng Chem Res*, vol. 48, no. 9, pp. 4316–4321, May 2009, doi: 10.1021/ie8007067.

[62] S. Li, Y. Chen, L. Huang, and D. Pan, “Simple continuous-flow synthesis of Cu–In–Zn–S/ZnS and Ag–In–Zn–S/ZnS core/shell quantum dots,” *Nanotechnology*, vol. 24, no. 39, p. 395705, Oct. 2013, doi: 10.1088/0957-4484/24/39/395705.

[63] J. Li, Q. Wu, and J. Wu, “Synthesis of Nanoparticles via Solvothermal and Hydrothermal Methods,” in *Handbook of Nanoparticles*, Cham: Springer International Publishing, 2016, pp. 295–328. doi: 10.1007/978-3-319-15338-4_17.

[64] C. B. Whitehead, S. Özkar, and R. G. Finke, “LaMer’s 1950 model of particle formation: A review and critical analysis of its classical nucleation and fluctuation theory basis, of competing models and mechanisms for phase-changes and particle formation, and then of its application to silver halide, semiconductor, metal, and metal-oxide nanoparticles,” *Materials Advances*, vol. 2, no. 1. Royal Society of Chemistry, pp. 186–235, 2021. doi: 10.1039/d0ma00439a.

[65] S. Mourdikoudis and L. M. Liz-Marzán, “Oleylamine in Nanoparticle Synthesis,” *Chemistry of Materials*, vol. 25, no. 9, pp. 1465–1476, May 2013, doi: 10.1021/cm4000476.

[66] M. A. Hines and G. D. Scholes, “Colloidal PbS Nanocrystals with Size-Tunable Near-Infrared Emission: Observation of Post-Synthesis Self-Narrowing of the Particle Size Distribution,” *Advanced Materials*, vol. 15, no. 21, pp. 1844–1849, Nov. 2003, doi: 10.1002/adma.200305395.

[67] J. M. Pietryga, R. D. Schaller, D. Werder, M. H. Stewart, V. I. Klimov, and J. A. Hollingsworth, “Pushing the band gap envelope: Mid-infrared emitting colloidal PbSe quantum dots,” *J Am Chem Soc*, vol. 126, no. 38, pp. 11752–11753, Sep. 2004, doi: 10.1021/ja047659f.

[68] J. W. Xiaogang Peng and A. P. Alivisatos, “Kinetics of II-VI and III-V Colloidal SemiconductorNanocrystal Growth: ‘Focusing’ of SizeDistributions,” *J. Am. Chem. Soc.*, vol. 120, 5343–5344, Feb. 1998.

[69] I. Moreels, Y. Justo, B. De Geyter, K. Haustraete, J. C. Martins, and Z. Hens, “Size-Tunable, Bright, and Stable PbS Quantum Dots: A Surface Chemistry Study,” *ACS Nano*, vol. 5, no. 3, pp. 2004–2012, Mar. 2011, doi: 10.1021/nn103050w.

[70] W. A. Tisdale, K. J. Williams, B. A. Timp, D. J. Norris, E. S. Aydil, and X.-Y. Zhu, “Hot-Electron Transfer from Semiconductor Nanocrystals,” *Science (1979)*, vol. 328, no. 5985, pp. 1543–1547, Jun. 2010, doi: 10.1126/science.1185509.

[71] D. V. Talapin, J.-S. Lee, M. V. Kovalenko, and E. V. Shevchenko, “Prospects of Colloidal Nanocrystals for Electronic and Optoelectronic Applications,” *Chem Rev*, vol. 110, no. 1, pp. 389–458, Jan. 2010, doi: 10.1021/cr900137k.

[72] M. C. Weidman, M. E. Beck, R. S. Hoffman, F. Prins, and W. A. Tisdale, “Monodisperse, air-stable PbS nanocrystals via precursor stoichiometry control,” *ACS Nano*, vol. 8, no. 6, pp. 6363–6371, Jun. 2014, doi: 10.1021/nn5018654.

[73] H. Liu *et al.*, “Enhancement of hydrogen sulfide gas sensing of PbS colloidal quantum dots by remote doping through ligand exchange,” *Sens Actuators B Chem*, vol. 212, pp. 434–439, Jun. 2015, doi: 10.1016/j.snb.2015.02.047.

[74] A. Mosahebfard, H. Dehdashti Jahromi, and M. H. Sheikhi, “Highly Sensitive, Room Temperature Methane Gas Sensor Based on Lead Sulfide Colloidal Nanocrystals,” *IEEE Sens J*, vol. 16, no. 11, pp. 4174–4179, Jun. 2016, doi: 10.1109/JSEN.2016.2546966.

[75] “Abé, S., Capek, R., De Geyter, B., & Hens, Z. (2012). Tuning the postfocused size of colloidal nanocrystals by the reaction rate. ChemCYS Book of Abstracts. Presented at the Chemistry conference for Young Scientists 2012 (ChemCYS 2012), Blankenberge, Belgium.,”

[76] M. Sharma, S. Kumar, and O. P. Pandey, “Study of energy transfer from capping agents to intrinsic vacancies/defects in passivated ZnS nanoparticles,” *Journal of Nanoparticle Research*, vol. 12, no. 7, pp. 2655–2666, Sep. 2010, doi: 10.1007/s11051-009-9844-2.

[77] E. J. D. Klem, H. Shukla, S. Hinds, D. D. MacNeil, L. Levina, and E. H. Sargent, “Impact of dithiol treatment and air annealing on the conductivity, mobility, and hole density in PbS colloidal quantum dot solids,” *Appl Phys Lett*, vol. 92, no. 21, p. 212105, May 2008, doi: 10.1063/1.2917800.

[78] S. Basu and P. K. Basu, “Nanocrystalline Metal Oxides for Methane Sensors: Role of Noble Metals,” *J Sens*, vol. 2009, pp. 1–20, 2009, doi: 10.1155/2009/861968.

[79] A. Mosahebfard, R. Safaiee, and M. H. Sheikhi, “Density functional theory of influence of methane adsorption on the electronic properties of a PbS cluster,” *Pramana - Journal of Physics*, vol. 93, no. 1, Jul. 2019, doi: 10.1007/s12043-019-1759-6.

[80] G. Korotcenkov and B. K. Cho, “Metal oxide composites in conductometric gas sensors: Achievements and challenges,” *Sens Actuators B Chem*, vol. 244, pp. 182–210, Jun. 2017, doi: 10.1016/j.snb.2016.12.117.

[81] Y. Li, A.-S. Xiao, B. Zou, H.-X. Zhang, K.-L. Yan, and Y. Lin, “Advances of metal–organic frameworks for gas sensing,” *Polyhedron*, vol. 154, pp. 83–97, Nov. 2018, doi: 10.1016/j.poly.2018.07.028.

[82] S. J. Choi and I. D. Kim, “Recent Developments in 2D Nanomaterials for Chemiresistive-Type Gas Sensors,” *Electronic Materials Letters*, vol. 14, no. 3. The Korean Institute of Metals and Materials, pp. 221–260, May 01, 2018. doi: 10.1007/s13391-018-0044-z.

[83] J. S. Jang, S. J. Choi, S. J. Kim, M. Hakim, and I. D. Kim, “Rational Design of Highly Porous SnO2 Nanotubes Functionalized with Biomimetic Nanocatalysts for Direct Observation of Simulated Diabetes,” *Adv Funct Mater*, vol. 26, no. 26, pp. 4740–4748, Jul. 2016, doi: 10.1002/adfm.201600797.

[84] Y. Guo *et al.*, “Hierarchical graphene-polyaniline nanocomposite films for high-performance flexible electronic gas sensors,” *Nanoscale*, vol. 8, no. 23, pp. 12073–12080, Jun. 2016, doi: 10.1039/c6nr02540d.

[85] F. Shao *et al.*, “Heterostructured p-CuO (nanoparticle)/n-SnO2 (nanowire) devices for selective H2S detection,” *Sens Actuators B Chem*, vol. 181, pp. 130–135, 2013, doi: 10.1016/j.snb.2013.01.067.

[86] Y. Jiang, N. Tang, C. Zhou, Z. Han, H. Qu, and X. Duan, “A chemiresistive sensor array from conductive polymer nanowires fabricated by nanoscale soft lithography,” *Nanoscale*, vol. 10, no. 44, pp. 20578–20586, Nov. 2018, doi: 10.1039/c8nr04198a.

[87] J. Fu, C. Zhao, J. Zhang, Y. Peng, and E. Xie, “Enhanced gas sensing performance of electrospun Pt-functionalized NiO nanotubes with chemical and electronic sensitization,” *ACS Appl Mater Interfaces*, vol. 5, no. 15, pp. 7410–7416, Aug. 2013, doi: 10.1021/am4017347.

[88] L. Xiao, S. Xu, G. Yu, and S. Liu, “Efficient hierarchical mixed Pd/SnO2 porous architecture deposited microheater for low power ethanol gas sensor,” *Sens Actuators B Chem*, vol. 255, pp. 2002–2010, Feb. 2018, doi: 10.1016/j.snb.2017.08.216.

[89] M. K. Nakhleh *et al.*, “Sensor arrays based on nanoparticles for early detection of kidney injury by breath samples,” *Nanomedicine*, vol. 10, no. 8, pp. 1767–1776, Nov. 2014, doi: 10.1016/j.nano.2014.06.007.

[90] D. R. Miller, S. A. Akbar, and P. A. Morris, “Nanoscale metal oxide-based heterojunctions for gas sensing: A review,” *Sensors and Actuators, B: Chemical*, vol. 204. Elsevier, pp. 250–272, Dec. 01, 2014. doi: 10.1016/j.snb.2014.07.074.

[91] P. A. Russo *et al.*, “Room-temperature hydrogen sensing with heteronanostructures based on reduced graphene oxide and tin oxide,” *Angewandte Chemie - International Edition*, vol. 51, no. 44, pp. 11053–11057, Oct. 2012, doi: 10.1002/anie.201204373.

[92] S. Liu, B. Yu, H. Zhang, T. Fei, and T. Zhang, “Enhancing NO2 gas sensing performances at room temperature based on reduced graphene oxide-ZnO nanoparticles hybrids,” *Sens Actuators B Chem*, vol. 202, pp. 272–278, Oct. 2014, doi: 10.1016/j.snb.2014.05.086.

[93] K. R. Nemade and S. A. Waghuley, “LPG sensing application of graphene/Bi2O3 quantum dots composites,” *Solid State Sci*, vol. 22, pp. 27–32, Aug. 2013, doi: 10.1016/j.solidstatesciences.2013.05.008.

[94] H. Kan *et al.*, “PbS Nanowires-on-Paper Sensors for Room-Temperature Gas Detection,” *IEEE Sens J*, vol. 19, no. 3, pp. 846–851, Feb. 2019, doi: 10.1109/JSEN.2018.2879895.

[95] Z. Wu *et al.*, “Room Temperature Methane Sensor Based on Graphene Nanosheets/Polyaniline Nanocomposite Thin Film,” *IEEE Sens J*, vol. 13, no. 2, pp. 777–782, Feb. 2013, doi: 10.1109/JSEN.2012.2227597.

[96] D. A. Gidlow, “Lead toxicity,” *Occup Med (Chic Ill)*, vol. 54, no. 2, pp. 76–81, Mar. 2004, doi: 10.1093/occmed/kqh019.

[97] K. LEE, “Toxicity of N-methyl-2-pyrrolidone (NMP): Teratogenic, subchronic, and two-year inhalation studies,” *Fundamental and Applied Toxicology*, vol. 9, no. 2, pp. 222–235, Aug. 1987, doi: 10.1016/0272-0590(87)90045-5.

[98] D. Koziej, N. Bârsan, U. Weimar, J. Szuber, K. Shimanoe, and N. Yamazoe, “Water–oxygen interplay on tin dioxide surface: Implication on gas sensing,” *Chem Phys Lett*, vol. 410, no. 4–6, pp. 321–323, Jul. 2005, doi: 10.1016/j.cplett.2005.05.107.

[99] N. Lu, S. Fan, Y. Zhao, B. Yang, Z. Hua, and Y. Wu, “A selective methane gas sensor with printed catalytic films as active filters,” *Sens Actuators B Chem*, vol. 347, p. 130603, Nov. 2021, doi: 10.1016/j.snb.2021.130603.

[100] Valentina Berlin, “Graphene oxide reduction and decoration with lead sulphide nanoparticles for gas sensing application,” Politecnico Milano 1863, 2022.

[101] ZEISS, “Product Information Version 1.0 - ZEISS Axio Imager Vario Examine Large Specimens – Automated and Compatible with Clean Rooms.”

[102] C. Weidenthaler, “Pitfalls in the characterization of nanoporous and nanosized materials,” *Nanoscale*, vol. 3, no. 3. pp. 792–810, Mar. 2011. doi: 10.1039/c0nr00561d.

[103] A. Vomiero *et al.*, “In2O3 nanowires for gas sensors: morphology and sensing characterisation,” *Thin Solid Films*, vol. 515, no. 23, pp. 8356–8359, Sep. 2007, doi: 10.1016/j.tsf.2007.03.034.

[104] J. Park, Y. Kim, S. Y. Park, S. J. Sung, H. W. Jang, and C. R. Park, “Band gap engineering of graphene oxide for ultrasensitive NO2 gas sensing,” *Carbon N Y*, vol. 159, pp. 175–184, Apr. 2020, doi: 10.1016/j.carbon.2019.11.063.

[105] J. Zhang, H. Yang, G. Shen, P. Cheng, J. Zhang, and S. Guo, “Reduction of graphene oxide via <scp>l</scp> -ascorbic acid,” *Chem. Commun.*, vol. 46, no. 7, pp. 1112–1114, 2010, doi: 10.1039/B917705A.

[106] S. Stankovich *et al.*, “Synthesis of graphene-based nanosheets via chemical reduction of exfoliated graphite oxide,” *Carbon N Y*, vol. 45, no. 7, pp. 1558–1565, Jun. 2007, doi: 10.1016/j.carbon.2007.02.034.

[107] S. Some *et al.*, “High-quality reduced graphene oxide by a dual-function chemical reduction and healing process,” *Sci Rep*, vol. 3, May 2013, doi: 10.1038/srep01929.

[108] W. D. Yang and Y. J. Lin, “Preparation of rGO/Bi2O3 composites by hydrothermal synthesis for supercapacitor electrode,” *Journal of Electrical Engineering*, vol. 70, no. 7, pp. 101–106, Dec. 2019, doi: 10.2478/jee-2019-0049.

[109] R. I. R. Blyth *et al.*, “XPS studies of graphite electrode materials for lithium ion batteries,” Graz, Jul. 2000. doi: https://doi.org/10.1016/S0169-4332(00)00525-0.

[110] S. Pei and H.-M. Cheng, “The reduction of graphene oxide,” *Carbon N Y*, vol. 50, no. 9, pp. 3210–3228, Aug. 2012, doi: 10.1016/j.carbon.2011.11.010.

[111] Y. Jin, Y. Zheng, S. G. Podkolzin, and W. Lee, “Band gap of reduced graphene oxide tuned by controlling functional groups,” *J Mater Chem C Mater*, vol. 8, no. 14, pp. 4885–4894, 2020, doi: 10.1039/C9TC07063J.

[112] Graphenea, “Graphenea GO Powder Datasheet 202109.” 2021. Accessed: Jun. 01, 2023. [Online]. Available: https://www.graphenea.com/collections/graphene-oxide/products/graphene-oxide-powder

[113] B. Deng *et al.*, “High yield synthesis of matchstick-like PbS nanocrystals using mesoporous organosilica as template,” *Nanoscale*, vol. 3, no. 3, pp. 1014–1021, Mar. 2011, doi: 10.1039/c0nr00741b.

[114] R. Bai, S. Chaudhary, and D. K. Pandya, “Temperature dependent charge transport mechanisms in highly crystalline p-PbS cubic nanocrystals grown by chemical bath deposition,” *Mater Sci Semicond Process*, vol. 75, pp. 301–310, Mar. 2018, doi: 10.1016/j.mssp.2017.12.003.

[115] Z. Zhuang, Q. Peng, and Y. Li, “Controlled synthesis of semiconductor nanostructures in the liquid phase,” *Chem Soc Rev*, vol. 40, no. 11, pp. 5492–5513, Oct. 2011, doi: 10.1039/c1cs15095b.

[116] C. Zha *et al.*, “Facet engineering of monodisperse PbS nanocrystals with shape- and facet-dependent photoresponse activity,” *RSC Adv*, vol. 6, no. 109, pp. 107151–107157, 2016, doi: 10.1039/C6RA24119K.

[117] M. R. Loghman-Estarki and M. Rafiei, “Synthesis and characterization of mercaptoacetic acid/lead sulfide inorganic/organic nanocomposite,” *Journal of Materials Science: Materials in Electronics*, vol. 27, no. 12, pp. 12852–12859, Dec. 2016, doi: 10.1007/s10854-016-5420-6.

[118] A. K. Mishra and S. Saha, “Growth and Characterization of PbS Nanoparticles Using THF,” Medinipur, Dec. 2018. [Online]. Available: www.vidyasagar.ac.in/publication/journal

[119] H. Beygi, S. A. Sajjadi, A. Babakhani, J. F. Young, and F. C. J. M. van Veggel, “Surface chemistry of as-synthesized and air-oxidized PbS quantum dots,” *Appl Surf Sci*, vol. 457, pp. 1–10, Nov. 2018, doi: 10.1016/j.apsusc.2018.06.152.

[120] B. Muchharla, T. N. Narayanan, K. Balakrishnan, P. M. Ajayan, and S. Talapatra, “Temperature dependent electrical transport of disordered reduced graphene oxide,” *2d Mater*, vol. 1, no. 1, Jun. 2014, doi: 10.1088/2053-1583/1/1/011008.

[121] M. Trushin, “Thermally activated conductivity in gapped bilayer graphene,” *EPL (Europhysics Letters)*, vol. 98, no. 4, p. 47007, May 2012, doi: 10.1209/0295-5075/98/47007.

[122] N. F. Mott, E. A. Davis, and K. Weiser, “*Electronic Processes in Non-Crystalline Materials*,” *Phys Today*, vol. 25, no. 12, pp. 55–55, Dec. 1972, doi: 10.1063/1.3071145.

[123] R. C. Keitel, M. C. Weidman, and W. A. Tisdale, “Near-Infrared Photoluminescence and Thermal Stability of PbS Nanocrystals at Elevated Temperatures,” *The Journal of Physical Chemistry C*, vol. 120, no. 36, pp. 20341–20349, Sep. 2016, doi: 10.1021/acs.jpcc.6b06053.

[124] N. Yang *et al.*, “The Effects of Graphene Stacking on the Performance of Methane Sensor: A First-Principles Study on the Adsorption, Band Gap and Doping of Graphene,” *Sensors*, vol. 18, no. 2, p. 422, Feb. 2018, doi: 10.3390/s18020422.

[125] C. Gong, M. Acik, R. M. Abolfath, Y. Chabal, and K. Cho, “Graphitization of Graphene Oxide with Ethanol during Thermal Reduction,” *The Journal of Physical Chemistry C*, vol. 116, no. 18, pp. 9969–9979, May 2012, doi: 10.1021/jp212584t.

[126] M. A. Karimi, M. Ranjbar, and A. Salmanipour, “Novel solvothermal synthesis and characterization of Ag2S/PbSO4 nanocomposites,” *Journal of Saudi Chemical Society*, vol. 21, no. 2, pp. 193–197, Feb. 2017, doi: 10.1016/j.jscs.2015.04.006.

[127] İ. A. Kariper, “What is the Effect of Critical Surface Tension of PbSO3 Thin Film?,” *Metallurgical and Materials Transactions A*, vol. 45, no. 10, pp. 4398–4404, Sep. 2014, doi: 10.1007/s11661-014-2387-x.

[128] Wikipedia, “Graphene,” 2023. https://en.wikipedia.org/wiki/Graphene (accessed May 27, 2023).

[129] Dmitry Kireev, “COMBINING GRAPHENE AND ORGANIC FERROELECTRIC FOR POSSIBLE MEMORY DEVICES Thesis for the Degree of Erasmus Mundus Master of Nanoscience and Nanotechnology Chalmers University of Technology & KULeuven,” KULeuven, Leuven, Belgium, 2013.

VI. APPENDIX

6.1 Raman Spectra

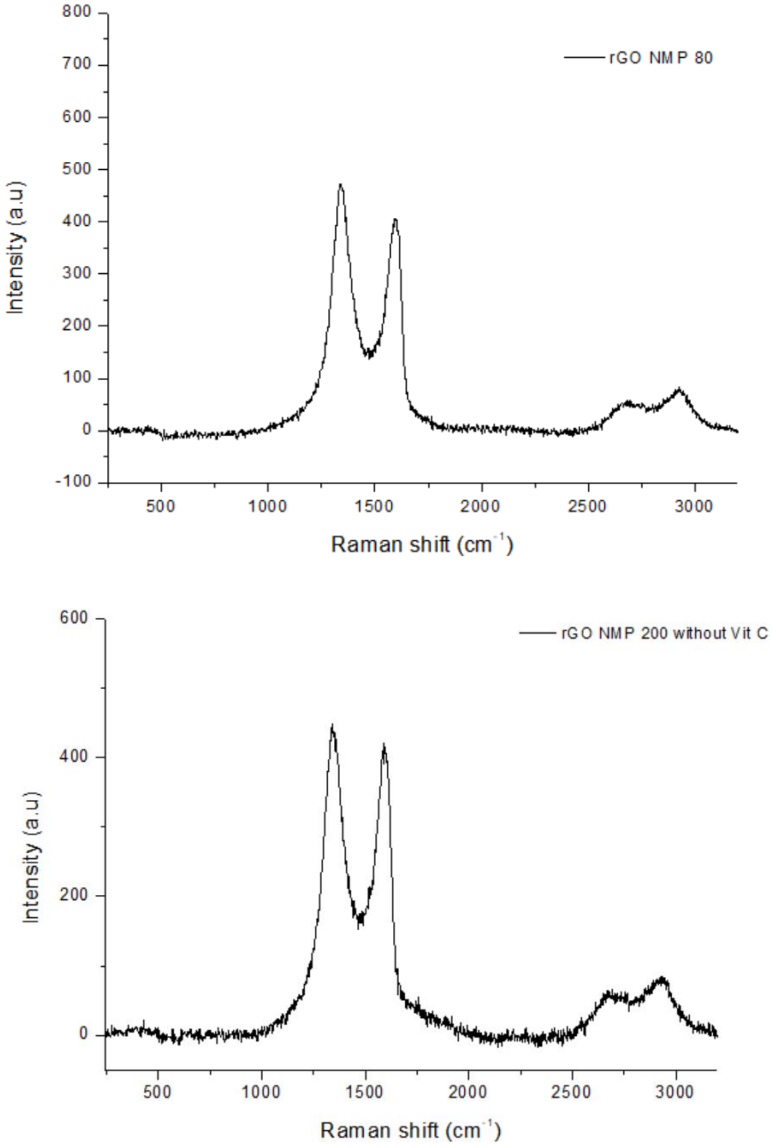

Figure 62. Raman spectra of rGOs

6.2 XPS Spectra

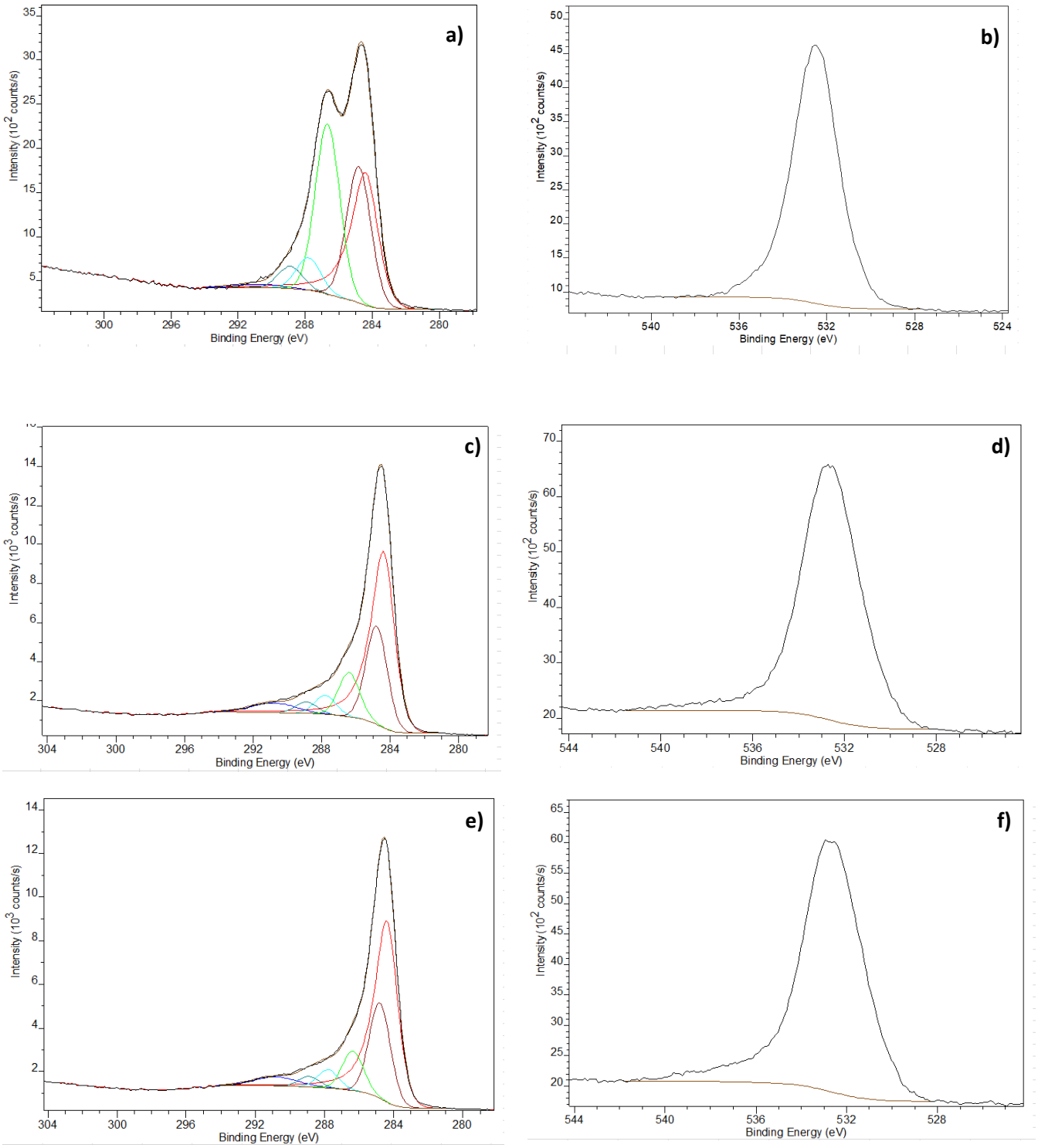

Figure 63. XPS spectra of rGO NMP 80 a-b) rGO 90 full Vit. C c-d) rGO 90 half Vit. C. All spectra display C 1s (left) and O 1s (right)

6.3 XRD diffractograms of PbS samples from the 1st protocol

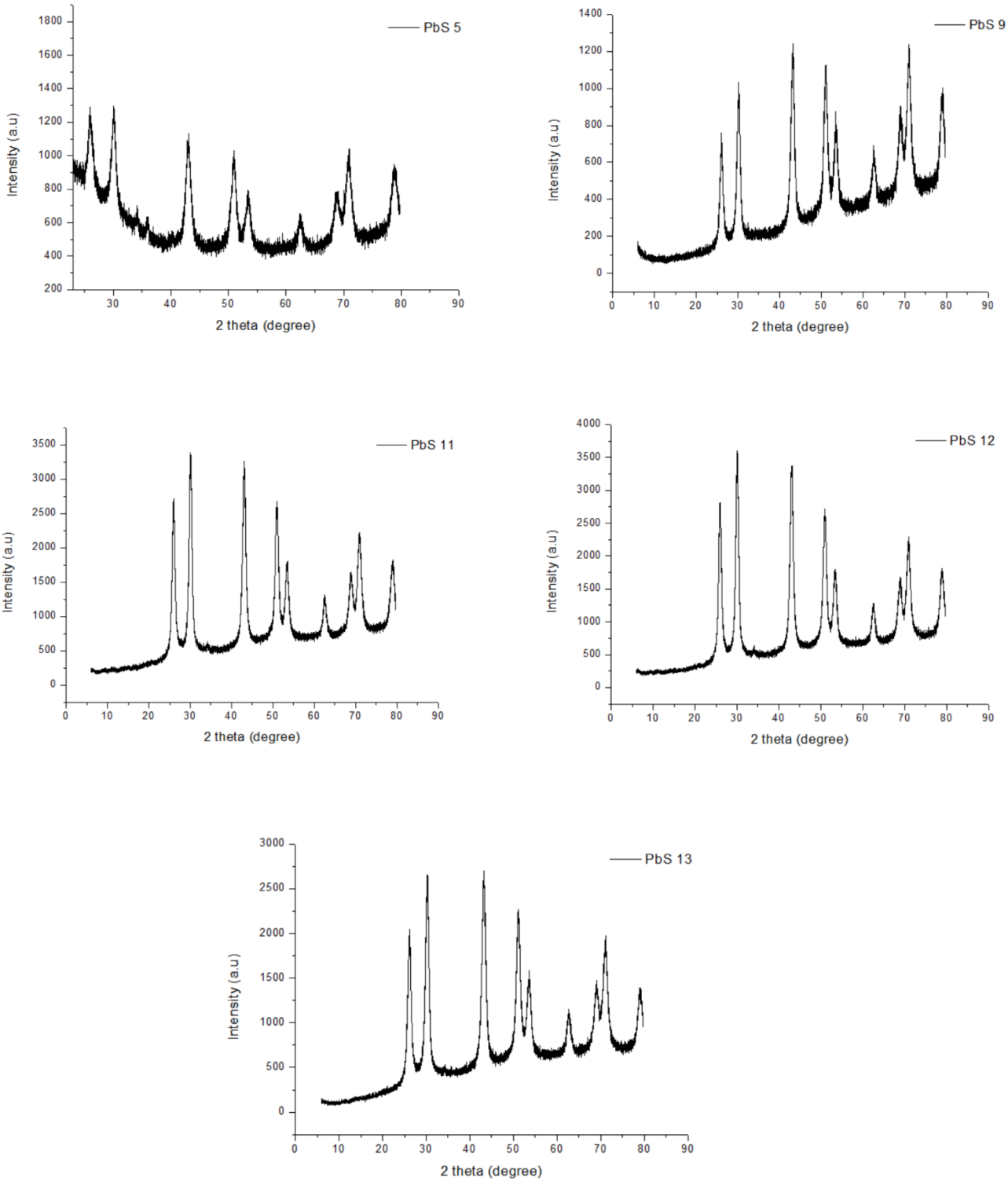

Figure 64. XRD patterns of different PbS samples

6.4 XRD Spectra of TGA residue of PbS sample

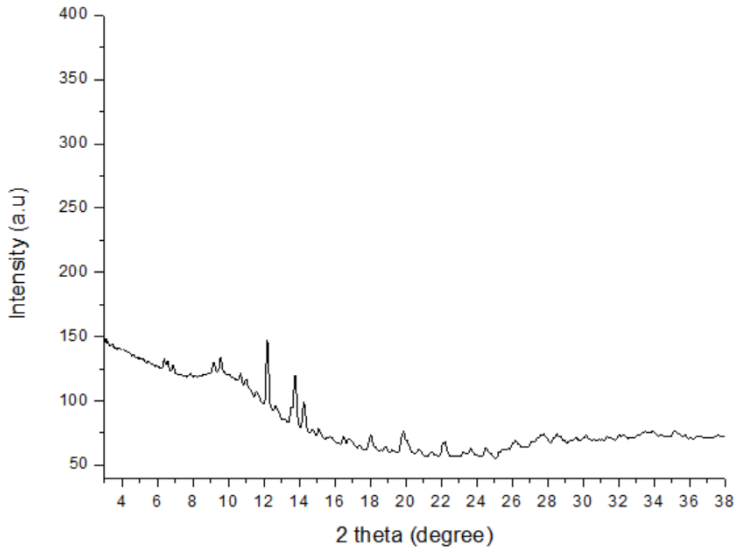

Figure 65 XRD pattern of suspected oxidized PbS 4 after TGA

$PbSO_4$ has multiple peaks located at 21°, 23°, 28°, 29°, 44°, 49°, 51°, 58°, 64° and 71°. [126] The peaks of $PbSO_3$ are located at 22.61°, 26.46°, 54.24° and 67.18°. [127] Fig. 65 shows distinguishable peaks at 12°, 13°, 14° 18°, 19°, 22°, the others are not interpretable.

6.5 DR – UV-visible Absorbance Spectra of the four selected PbS samples

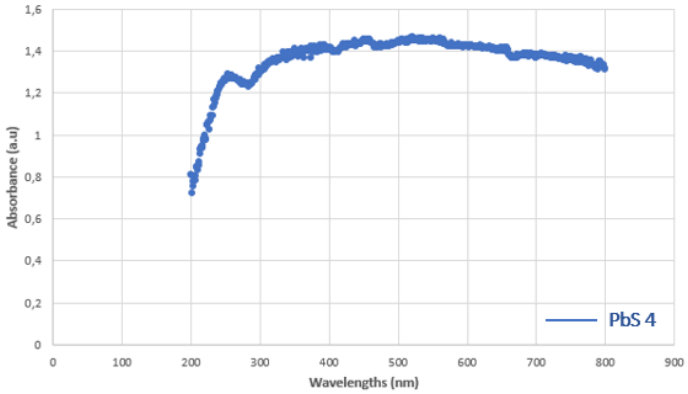

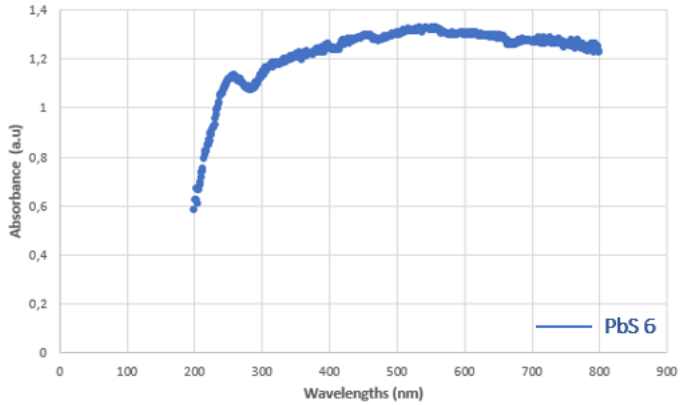

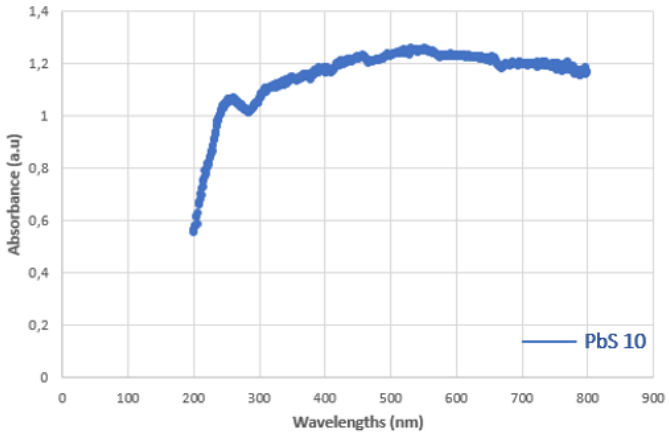

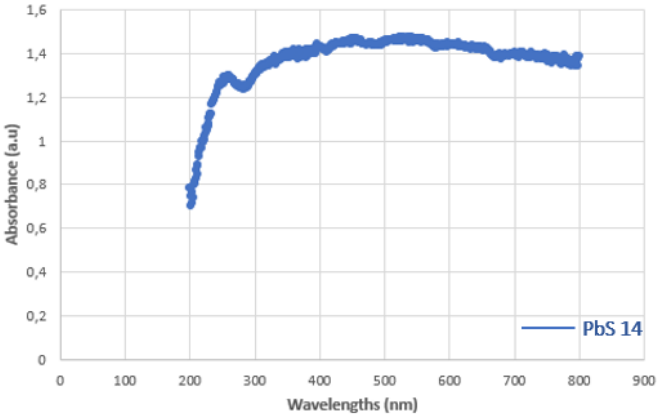

Figure 66. DR UV-vis absorbance spectra of PbS samples. Absorbance saturates around 200 nm

6.6 Arrhenius plot of the mixed rGO/PbS sample

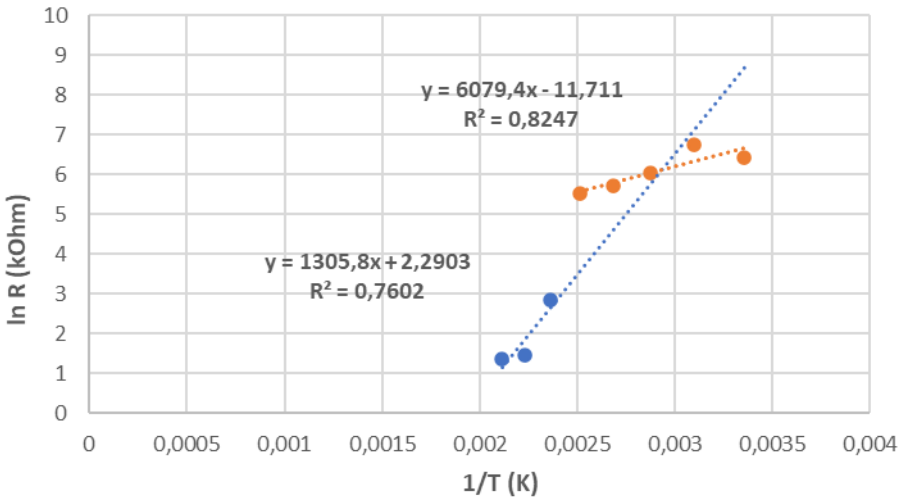

Figure 67. Arrhenius plot of resistance as a function of temperature for rGO 1 /PbS 4 sample

UNIVERSITÉ CATHOLIQUE DE LOUVAIN
Faculté des sciences
Place des sciences, 2 bte L6.06.01, 1348 Louvain-la-Neuve, Belgique | **www.uclouvain.be/sc**